LIFE CYCLE MONITORING OF REVERSIBLE ADHESIVE BONDED JOINTS USING GUIDED WAVES

By

Rajendra Prasath Palanisamy

A DISSERTATION

Submitted to
Michigan State University
in partial fulfillment of the requirements
for the degree of

Civil Engineering – Doctor of Philosophy

2022

ABSTRACT

LIFE CYCLE MONITORING OF REVERSIBLE ADHESIVE BONDED JOINTS USING GUIDED WAVES

By

Rajendra Prasath Palanisamy

Recent advancements in automotive, aerospace, civil and wind-energy industries have resulted in an ever-increasing demand for lightweight, cost-effective, rapidly manufactured and recyclable/reusable of structural components. Adopting composite materials is a popular solution to achieve light-weighting, however it requires complex joining methods compared to traditional mechanical fasteners. Electromagnetic targeted heating of nano-Fe_3O_4 reinforced thermoplastic adhesives (Reversible-Adhesive) is an emerging technique for rapid assembly, dis-assembly, and re-assembly of bonded composite parts. Alternate magnetic field applied to the dispersed ferromagnetic nanoparticles (FMNP) within a thermoplastic adhesive results in these particles acting as nano-heaters and rapidly heating the surrounding material resulting in melting and flow of the adhesive, which upon cooling forms a structural bond. This process can be repeated and hence termed reversible adhesive.

Reversible-adhesive bonded composite structures (RBCS) offer a greater advantage over thermosets or mechanical joints such as rapid processing, easy repair, quick disassembly, and possible re-usability of components. However, it is essential to accurately measure the temperature of the adhesive during processing and repair, since overheating may cause chemical degradation and underheating may introduce improper bonds. Adhesively bonded composite structures provide a more uniform stress distribution in the bond-line than riveted joints resulting in higher fatigue life. However, modeling the physics behind crack initiation and propagation inside bonded regions is challenging especially under fatigue loading. As a result, real-time in-service bond monitoring is required to ensure structural safety. In addition to monitoring the damage state, prediction of damage area and remaining useful life of the component is imperative. Thus, this research work

focusses on developing a life cycle monitoring solution for RBCS using the guided wave (GW) technique.

Ultrasonic guided waves were made to propagate across the bond-line of the joint by exciting and sensing them using miniature piezoelectric wafers. Analysis of dispersion relations and dynamic wave propagation were performed using finite element modeling (FEM). Fundamental longitudinal mode L_0 at 35 kHz was found optimal for bond process monitoring. Mapping between the FE-simulated transmission coefficient of L_0 and actual temperature of the thermoplastic adhesive was established using the DMA test data. Real-time guided wave measurements were used as feedback in the discrete control of the induction heater so as to provide optimal bonding and prevent adhesive degradation. The developed ultrasonic technique was successfully validated by fiber-optic temperature sensing. Results indicate that the bondlines processed with GW control offer better ultimate strength compared to uncontrolled processing.

Guided wave modal and frequency sensitivity analysis for fatigue damage was performed. Based on the analysis, symmetric mode at 85 kHz was found optimal for fatigue damage detection. Further, a damage propagation model based on Paris law was developed to estimate remaining useful life in terms of the GW signal features. Finally, the remaining useful life of the lap-joint was predicted and validated experimentally. One of the major advantages of reversible adhesive is its ability to repair/heal the damage. The controlled processing technique developed earlier was used for controlled healing of fatigue damaged joints. Experimental investigation proves the healed-bond line have returned to its original strength. A holistic approach of a complete lifecycle monitoring of bonded joints was aimed at increasing the confidence in the use of bonded joints relative to mechanical fasteners, and can be easily extended to other structural applications.

ACKNOWLEDGMENTS

First, I would like to acknowledge my advisors Dr. Mahmoodul Haq and Dr. Yiming Deng for their technical and moral support throughout my doctoral career. I am grateful to Dr. Haq for introducing me to reversible adhesive and non-destructive testing methods, which laid the foundation for my thesis.

I must also acknowledge the members of my thesis committee: Dr. Lalita Udpa, from the department of electrical and computer science engineering, and Dr. Weiyi Lu of the department of civil and environmental engineering. In supplement to my primary advisor, these three helped to guide my research program through their valuable suggestion and feedback.

My deepest gratitude goes to all my family members who supported me through the ups and downs of graduate student life. I could not have done it without you, my mother Gowri, my father Palanisamy, my sister Surya Prabha and my wife Priya. I offer my special thanks to all my colleagues; Mr. Ben Swanson, Mr. Syed Fahad Hassan, Mr. Saratchandra Kundurthi, Dr. Suhail Hyder Vattathurvalappil, Dr. Portia Banerjee and Dr. Erik Stitt for their motivation and sincere help during the graduate program.

This research has been primarily supported through a research grant from the American Chemistry Council (ACC), Plastics division. I would also like to acknowledge Mr. Michael Day, Project manager at ACC. Next, I would like to thank ASNT (American Society of Nondestructive testing) for the fellowship award. Further, I thank for the financial support in the form of fellowship awards and assistantships from department of civil and environmental engineering and the graduate school of engineering.

TABLE OF CONTENTS

LIST OF TABLES

LIST OF FIGURES

CHAPTER 1

INTRODUCTION

Traditionally, non-destructive evaluations (NDE) involves setting up monitoring devices in a controlled environment and hard wired to identify suspecting localized damage. Most NDE is performed during its service life for repair and maintenance. With advancing technology, the development of monitoring systems within the life-cycle context of a structure or component is necessary. Emerging sensor technology opens the opportunity for continuous monitoring of components from its manufacturing process to in-service and failure. By combining the component information with the sensor network, the overall state of the structure shall be monitored throughout its lifetime. This process is called life cycle health monitoring [46]. This work is focused on the life cycle monitoring of the reversible-adhesive bonded composite structures (RBCS). Figure 1.1 shows the schematic of different life stages of RBCS and associated monitoring activity considered in this work.

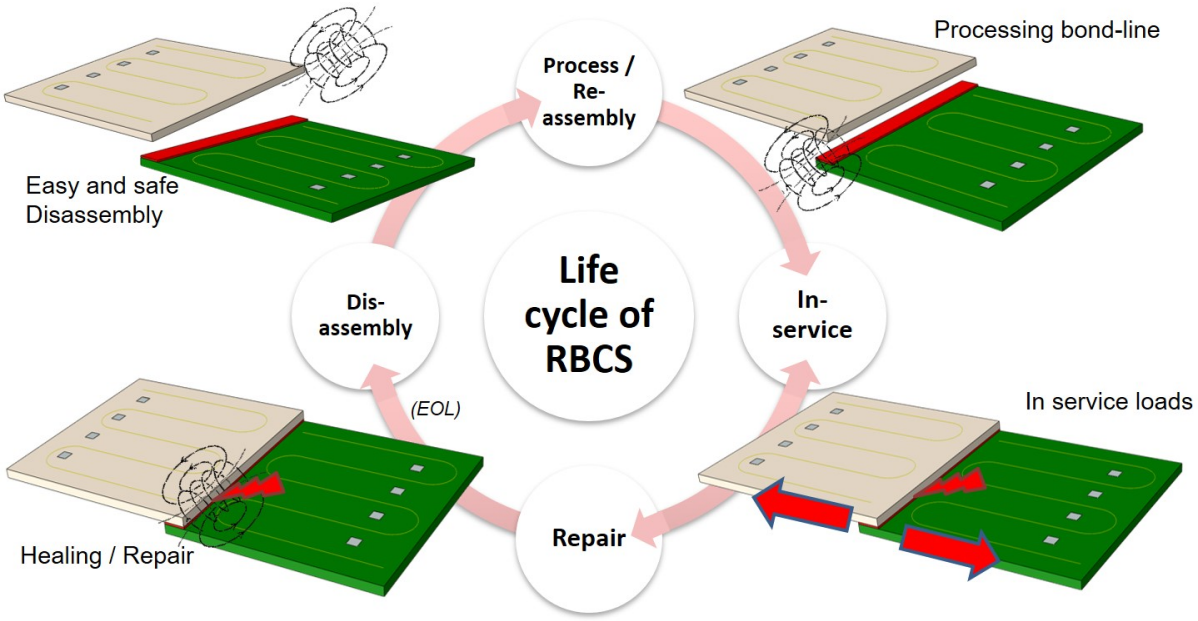

Figure 1.1: Overall Process of Life Cycle Health monitoring

Before introducing the monitoring techniques, it is important to know the reason for choosing

reversible adhesive bonds. Unlike mechanical joints, adhesive bonds are lightweight, free of holes which eliminates high-stress concentration. Adhesives shall be broadly classified into two types thermosets and thermoplastics. Thermoplastic adhesives modified with conductive nanoparticles and exposed to alternate magnetic field results in intensive heat dissipation and melting from within the adhesive. This phenomenon provides thermoplastics a greater advantage over thermosets such as rapid processing, easy repair, quick disassembly, and possible reusability of components [69]. However, it is essential to accurately measure the temperature of the adhesive, since overheating may cause chemical degradation and underheating may introduce kissing bonds. Thus one cannot take full advantage of thermoplastics unless a parallel monitoring system is implemented. Thus, proposed techniques monitor the bond-line during processing and repair. During the in-service period, the system continuously monitors the bond-line and substrates for any defects. Also, the system simultaneously predicts the Remaining Useful Life (RUL) of the components. Studies show dis-assembly of reversible-adhesive components are much easier compared to chemical or mechanical dismantling process [44, 74]. In most cases, once the components are disassembled the bond-line areas are resurfaced and a fresh adhesive is used during re-assembly. Thus, a bond-line monitoring technique during disassembly is considered less important and not included in this study.

By implementing life cycle monitoring the overall reliability of the structure shall be improved such as (1) Quality control: Every RBCS manufactured in the assembly line is monitored for processing defects. (2) Timely warning on components health during the in-service period avoids any catastrophic failure. (3) Monitored repairs increase the confidence in using repaired components. (5) Continuous in-service monitoring helps in the prognosis of various failures.

1.1 Objective

Automotive industries in the last decade are demanding for light-weight, cost-effective, and multi-material joining solutions [44]. Adhesively bonded joints having all such properties, quickly gain popularity over traditional mechanical joints. Adhesive bonds also provide better vibration damping

and uniform stress distribution properties.

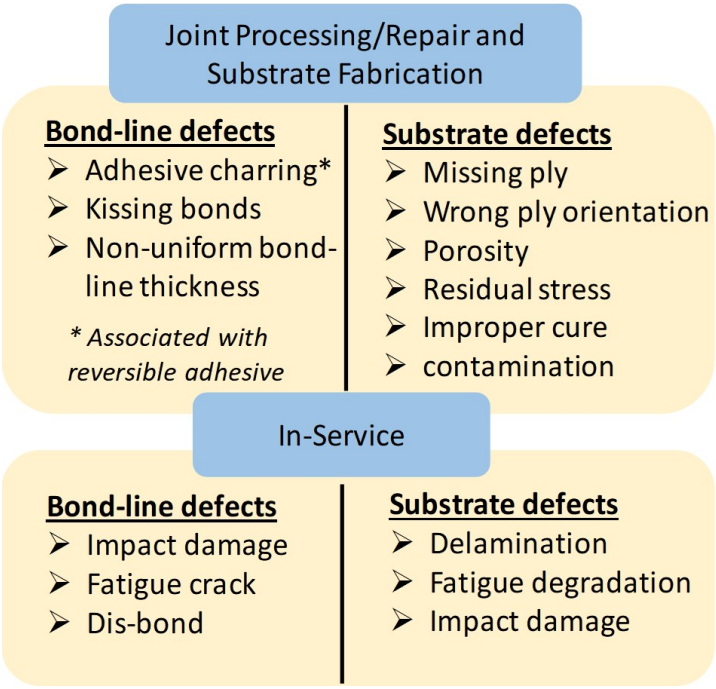

Figure 1.2: Some common defects found in adhesively bonded joints during fabrication and in-service.

With the introduction of reversible adhesive, targeted heating and easy dismantle further elevate the popularity of RBCS. However, In comparison to metallic riveted joints, one of the major challenges in bonded joints and laminated composites is various processing and in-service defects (see Figure 1.2). Defects at all life stages shall be classified into bond-line and substrate defects. Life cycle monitoring is the best solution to improve the reliability of adhesive bonded components. Thus, the overall objective of this work is to develop a life cycle monitoring framework with prognosis for RBCS.

The monitoring approach at each stage involves strategic sensor deployment, data acquisition, and signal processing. In process monitoring, Analysis of dispersion relations and dynamic wave propagation were performed using finite element modeling (FEM). Fundamental longitudinal mode L0 at 35 kHz was found optimal for bond process monitoring. Real-time guided wave measurements were used as feedback in the discrete control of the induction heater to provide optimal bonding and prevent adhesive charring. A very similar approach shall be followed for repair monitoring.

Sensor deployment, excitation frequency, and mode selection all remain the same between process and repair monitoring. The only difference in repair monitoring is, the adhesive is expected to have some in-service damages. Unlike processing or repair, in-service monitoring cannot be generalized, it purely depends on the type of in-service loads. This work focuses primarily on fatigue loads. Guided wave modal and frequency sensitivity analysis for fatigue damage is performed. Based on the analysis, Symmetric mode at 85 kHz was found optimal for fatigue damage detection. Further, a damage propagation model based on Paris law is developed to estimate remaining useful life in terms of the GW signal features. Finally, the remaining useful life of the lap-joint is predicted and validated experimentally.

1.2 Background

This section illustrate the necessary background and current state of the art under each focus areas. Since this research work centers around the application of reversible adhesive, A detailed background study on reversible adhesive is discussed first. Later, application of Guided waves for bond motioning and existing fatigue prognosis techniques are discussed in detail.

1.2.1 Reversible Adhesive

Acrylonitrile butadiene styrene (ABS) terpolymer reinforced with Fe_3O_4 nanoparticles was used as adhesive to bond the substrates of the lap-joint. ABS is widely used in automotive, sports, electronics and other consumer markets owing to its good balance between cost, mechanical properties and ease of processing [56]. ABS pellets (CYCOLAC^{TM} Resin MG 94) obtained from Sabic® corporation were dry mixed with 16 wt.% of Fe_3O_4 nanoparticles (obtained from Sigma-Aldrich®) before they were fed into the twin-screw driven extruder to produce the adhesive films. 16 wt.% of Fe_3O_4 nanoparticles were chosen as they provided the optimum balance between mechanical and thermal properties [69].

Dynamic mechanical analysis (DMA) was performed using DMA Q800 analyzer from TA Instruments in order to determine the temperature dependent elastic modulus E of the ABS polymer.

All measurements were performed at a heating rate of $5^oC/min$ in the temperature range between 20^oC and 160^oC. A sinusoidal displacement of 20 μm with a frequency of 1 Hz was applied to the sample holder throughout the experiment. The elastic modulus E was calculated from the storage modulus $G^{'}$ and loss modulus $G^{''}$ using equation 1.1:

$$\sigma = \epsilon E = \epsilon \left(\sqrt{G'^2 + G''^2} \right), \tag{1.1}$$

where σ is stress, and ϵ is strain. Note that in (1.1), $G^{'}$ represents the elastic stored energy when the material is deformed, and $G^{''}$ represents the energy dissipation during the material deformation.

The temperature dependent elastic modulus obtained from DMA for ABS is shown in figure 1.3.

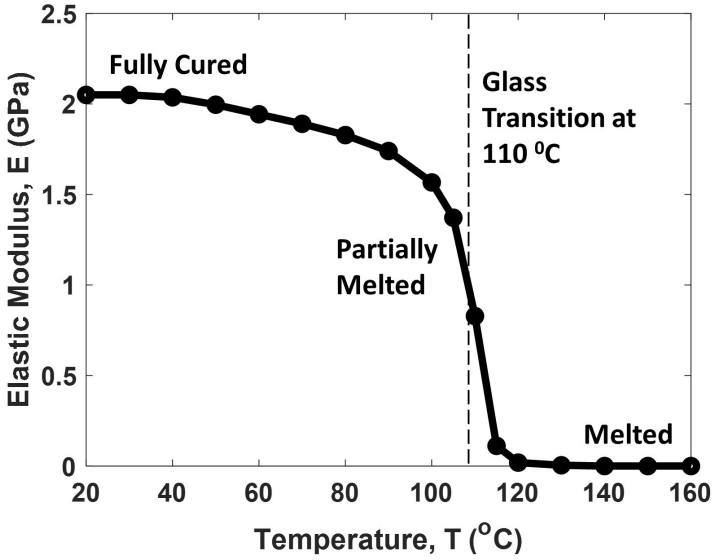

Figure 1.3: Dependence of ABS elastic modulus E on temperature.

The dynamic viscosity ν, which represents the internal resistance of a fluid to flow is also obtained from the DMA, and is shown in figure 1.4.

In the process of EM bonding, the FMNPs embedded in the thermoplastic adhesive generate heat using two possible mechanisms, such as hysteresis heating and Joule (resistive) heating. In case of hysteresis heating, the cause of heat generation is a hysteresis loss in individual FMNPs (see Figure 1.5(d)) due to the reversal of magnetization [10]. In case of Joule heating, the heat is produced

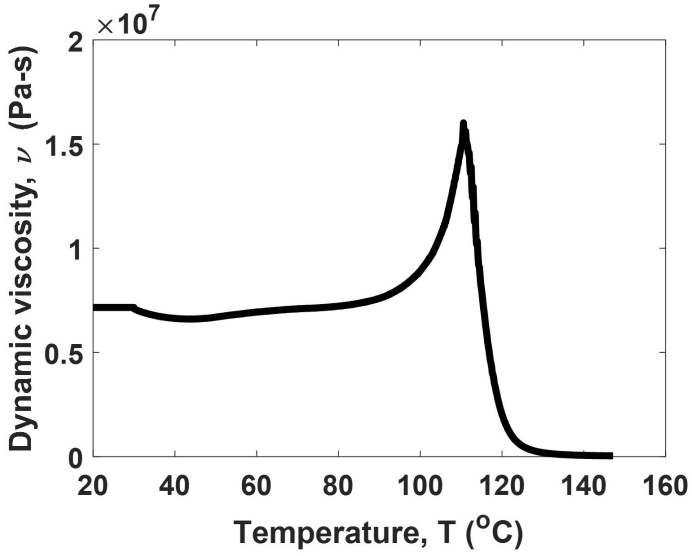

Figure 1.4: Dependence of ABS dynamic viscosity ν on temperature.

owing to induced eddy currents passing through local agglomerations of FMNPs (see Figure 1.5(a)). figure 1.5(b,c) [15] with SEM images showing nanoparticles responsible for hysteresis and Joule's heating. The clustering of nano-particles is observed in the images acquired with the

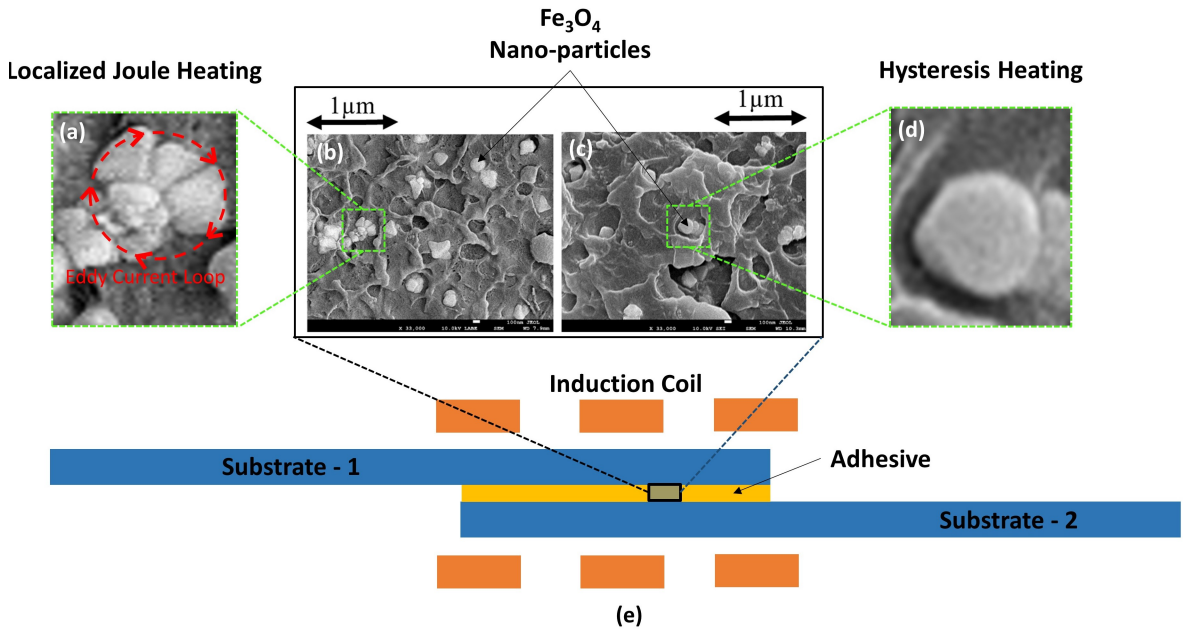

Figure 1.5: Schematic of structural bonding using EM induction heating technique (e) with SEM images (b,c) illustrating nanoparticles configuration responsible for joule (a) and hysteresis heating (d).

help of scanning electron microscopy (SEM). Induced eddy currents form loops as demonstrated in Figure 1.5(a). The power of generated Joule heat will increase with larger nano-particle clusters. However, the authors consider hysteresis loss a dominant source of heat generation in the adhesive, since FMNPs are generally well dispersed and clusters are less common. Properties of Fe_3O_4 nano-particles are given in Table 1.1, and the schematic of the adhesive bond-line of the lap-joint is shown in Figure 1.5(e).

Properties	**Value**	**Unit**
Size	50-100	nm
Density	5180	$\frac{kg}{m^3}$
Thermal Conductivity	90	$\frac{W}{mC}$
Specific heat	148.63	$\frac{J}{KgC}$
Elastic modulus	161	Gpa

Table 1.1: Material properties of Fe_3O_4 nano-particles.

1.2.2 Induction Bonding and Monitoring

The electromagnetic (EM) targeted heating of thermoplastic adhesives may offer multiple advantages over heating in a conventional oven such as rapid processing, high repeatability [71], low energy consumption and smaller space requirements. In this case, the adhesive is modified with ferromagnetic nanoparticles (FMNP) that interact with the applied electromagnetic field at radio or microwave frequencies [44, 18, 74]. The temperature of suspended nanoparticles rises owing to hysteretic losses, Neel relaxation and Brown relaxation losses, and friction losses making the surrounding adhesive melt from the inside [10, 9, 12, 11]. If the adherends of the joint are made of electrically insulating materials, they will be affected mainly by the heat transfer from the FMNP-reinforced adhesive [69, 68, 70].

However, several technical challenges need to be addressed in order to increase the technology readiness level (TRL) of the EM-activated reversible bonding. The temperature of the FMNP-modified adhesive need to be monitored in real-time, and the energy of the excitation EM field need to be actively controlled for optimal bonding and disassembly of a reversible structural joint.

The adhesive may suffer chemical degradation if heated above the optimal processing temperature. In contrast, the bond-line may develop kissing bonds if the adhesive is underheated. The amount of generated heat within the adhesive may differ depending on the weight fraction of the FMNPs, their type, average size, and surface functionalization that determine the specific power loss (SPL). Another issue to consider is the thermal profile of the adhesive during the EM heating process as it may be less uniform in comparison with heating in the convection oven. The local temperature distribution in the adhesive depends on such factors as the quality of FMNP dispersion, the uniformity of the applied EM field, and the overall geometry of the joint that determines the thermal boundary conditions [22]. For instance, possible agglomeration of FMNPs may lead to formation of eddy currents and Joule heating [10] in particulate clusters, and the shape of the coil or microwave applicator will determine the distribution of the excitation field.

To the best of authors knowledge, the studies on monitoring the aggregate state and temperature distribution within the FMNP-reinforced adhesives in manufacturing of structural joints have been limited. Ciardiello et al [19] used a setup with infrared (IR) cameras to measure the temperatures of the substrates and the exposed edges of the adhesive bond-line during the EM heating of the lap-shear joint. Vattathurvalappil et al [69] deployed the distributed fiber-optic sensor within the bond-line to measure the temperature of the adhesive using the optical frequency domain reflectometry (OFDR). The sensor consisted of a free single mode optical fiber covered by an insulating tube in order to decouple measured temperature from strain in the adhesive. The proposed technique was successful in capturing the temperature distribution along the axis of the embedded sensor. However, the diameter of the sensor was large enough to create a weak interface inside the bond-line and thereby act as a flaw that reduced the load carrying capacity of the joint.

In this research work, we present an ultrasonic guided wave technique for real-time monitoring of adhesive temperature and elastic modulus for controlled EM heating of FMNP-reinforced adhesive in manufacturing of reversible composite joints. The validation experiments are performed on a single lap-shear joint with glass fiber reinforced polymer (GFRP) adherends and nano-Fe_3O_4 reinforced acrylonitrile butadiene styrene (ABS) polymer adhesive. Guided waves (GW) are chosen

as the sensing modality, because: 1) they are sensitive to material properties of a wave guide in which they propagate (adhesive bond-line region); 2) being mechanical stress waves they do not interfere with electromagnetic radiation during the EM heating; and 3) they can travel relatively long distances with little attenuation so that the excitation and sensing transducers can be deployed conveniently away from the heating zone.

Application of GWs for in-situ damage detection in adhesively bonded joints was successfully demonstrated in several studies [30, 75, 77, 38]. GWs showed promise in identifying disbonds, cracks, and in-service fatigue damage [63, 64, 16, 24, 25, 7, 8]. The influence of bond interface properties on wave propagation was also thoroughly investigated [40, 63, 64]. Vogt et al.[76] showed the possibility of using ultrasonic GWs for monitoring the curing process of epoxy resins. Similarly, the experimental work by Hudson et al [32] featured a GW technique for real-time cure monitoring of carbon fiber reinforced polymer (CFRP) composites. The concepts described in the aforementioned studies were successfully implemented in a GW sensing technique proposed by the authors.

The GW technique presented here allows for the indirect measurement of the average temperature and Young's modulus of the FMNP-reinforced adhesive. Selected GW modes are excited in one adherend, propagate across the adhesive bond-line and are sensed at the opposite adherend of the lap-joint. Important properties such as amplitude, time-of-flight (TOF) and/or energy transmission coefficient are extracted from the acquired GW signals. Properties of transmitted guided waves are mapped into the adhesive temperature and modulus using validated finite element models (FEM) and the results of the dynamic mechanical analysis (DMA). The average temperature estimated with the help of the GW technique is also used as a feedback for the discrete control of the EM heater. The heater is programmed to turn off automatically as soon as the adhesive temperature reaches an optimal value so as to prevent charring. Additionally, the results of guided wave sensing are experimentally validated using the OFDR technique reported by the Vattathurvalappil et al [69].

1.2.3 Fatigue Diagnosis and Prognosis

Unlike mechanical fasteners or rivets in metallic components, composite structures prefer adhesively bonded joints which not only maintains low weight but also distribute the force over larger areas thereby avoiding stress concentrations. This extends the overall life cycle of a composite structure. However, fatigue degradation often leads to formation of cracks or disbonds in the adhesive layer which reduces the load carrying capacity of the joint. An un-monitored adhesive joint may be detrimental to a composite structure if not replaced or repaired on time. Hence, efficient non-destructive evaluation (NDE) technology is required to detect disbonds in adhesive joints and ensure reliability of the complex structures.

In recent studies, guided waves(GW) have been demonstrated as a potential NDE technique for monitoring disbonds in lap-joints of fiber-reinfored polymers [57, 61]. The propagation of guided waves in adhesively bonded lap joints and the influence of bond conditions in wave parameters have been thoroughly studied in the past [34, 40, 63, 64]. Recently, researchers used guided wave sensing to detect dis-bonds, cracks, post-cure and perform in-service monitoring [16, 24, 25]. Further, behavior of guided wave in lap-joint fatigue loading is studied by Karpenko et al., [37]. Most of the studies in lap joints are conducted to monitor the changes in guided wave features with damage propagation. There are minimal efforts in incorporating guided wave for prediction and estimation of remaining useful life in lap-joints.

The primary challenge of prediction of remaining life in lap joints is that the physics behind damage propagation in adhesively bonded structures is extremely complex and highly dependent on the geometry, ply layup, dimensions and material property. In order to accurately compute fatigue life of a lap joint, each time a new bonded joint has to be monitored, its corresponding FEM model needs to be developed. Some modeling approaches have been performed to understand the stress distribution and damage mechanism [2, 52]. Besides, all loading forces need to be accurately modeled. If one or more physical phenomenon or parameters are overlooked, the prediction results may be highly discrepant from the true state of the structure. Hence, it is imperative to utilize periodic NDE or Structural Health Monitoring (SHM) data to track and predict fatigue damage in

composite lap-joints in addition to physics based knowledge. Similar studies have been proposed before where residual stiffness of composite coupons were computed based on Paris-Paris law coupled with data from GW and optical NDE systems [8].

1.2.4 Healing of Thermoplastics

Repair or removal of damaged bond-line is expensive and it can even cause damage to adjoining structures. Using thermoplastic adhesive with dispersed ferrous nano-particles can enable localized healing and easy dismantling for re-usability of components. One of the commonly used bond-line healing technique is micro-encapsulation approach. Here the healing agent and catalyst are dispersed in epoxy matrix, Once a damage occurs the suspended capsules around the damage area release the healing agent which react with dispersed catalyst to polymerize and activate the healing process [79, 35]. Li et al [42], proposed a two step self-healing technique. In this method, first the initial cracks are closed using a steel frame and later placed in oven to introduce heat that activate healing of thermoplastic particles. Aubert et al [4], introduced cross-linked polymers that are capable of healing cracks by formation of thermal activated covalent bond. This reaction is also known as Diels-Adler reaction.

For bonding non-metallic substrates, Thermoplastics embedded with conductive nano-particles are great choice. Verna and ciardiello [74, 18], illustrated the assembling and dismantling of joints using Electro-Magnetic (EM) heating technique. EM offers various advantages over above mentioned healing techniques. EM healing allows targeted healing, reduced energy usage, rapid processing. Vattathurvalappil et al [72], demonstrated the ability of EM healing on impact damaged bondline. Alternate magnetic field applied to dispersed ferromagnetic nanoparticles (FMNP) introduces hysteresis losses in the FMNPs, which results in intensive heat dissipation and melting from within the adhesive. However, it is essential to accurately measure the temperature of the adhesive, since overheating may cause chemical degradation while repair. In this research work an ultrasonic guided wave technique for online monitoring of the adhesive state while repair and feedback control of the electromagnetic bonding process.

1.2.5 Material Characterization

Application of GW in material characterization and damage detection has been successfully demonstrated in several studies [77, 30, 75, 38] Recent studies used GW to detect disbonds, cracks, perform quality control, and in-service fatigue monitoring [64, 16, 24, 25, 6, 7] A Multiple Transmitter Multiple Receiver (MTMR) configuration is generally used for material characterization. In most of the above-mentioned studies, piezo-ceramic sensors are permanently bonded to the surface of the substrate during inspection. In this study we have developed a smart skin where the emended sensors can be reused. An inverse Rayleigh lamb wave technique is used to estimate the material properties in different direction. This technique is validated on a aluminum sample in identifying the material modulus in each direction. To enable rapid material classification, machine learning models are used to process the data collected from smart skin.

1.3 Thesis Organization

There are seven chapters in this thesis. The first chapter 1 introduces the Motivation, objective and illustrate the background work related to this research focus. Chapter 2 discusses the usage of Finite Element Method to understand the behavior of guided wave propagation under different bond-line state while curing. This chapter uses COMSOL for eigen-frequency analysis to determine dispersion relation and ABAQUS for Time-dependent, guided wave propagation. Chapter 3 focuses on developing an Guided Wave based method for online monitoring and controlling of induction bonding. Chapter 4 deals with developing fatigue damage model for adhesively bonded lap-joint and data driven prognosis technique for remaining useful life (RUL) estimation. Chapter 5 reports the advantage of controlled healing after fatigue damage in adhesively bonded lap-joint Chapter 6 introduces a conformable Smart skin with embedded piezoelectric sensors for material characterization. Finally, Chapter 7 summarizes the overall contribution to the field of structural Health Monitoring (SHM) and provides concluding remarks and future recommendations.

CHAPTER 2

FINITE ELEMENT MODELING OF GUIDED WAVES IN LAP JOINT

2.1 Introduction

This chapter first presents the Lap-joint geometry and material properties that are required for modeling. Next, two finite element models developed to understand dispersion properties and propagation of ultrasonic guided waves in the adhesively bonded lap-joint. The first model was an eigenfrequency study that helped determine possible GW modes in the adherends and the bond-line region of the joint. Results of the study were used to identify an optimal excitation frequency and select the mode shape that would be most sensitive to changes in the modulus of the adhesive. The second FE model was a time-dependent study of wave propagation from one adherend to another adherend thorough the bond-line. Guided wave signals were simulated at different adhesive temperatures in order to link the features in the signals such as energy, peak amplitude or time-of-flight to adhesive state. Temperature-dependent viscoelastic properties of the adhesive were taken from the DMA, and uniform temperature distribution in the adhesive was assumed for simplicity.

2.2 Lap-joint Geometry and Material Properties

Single lap-shear joint was manufactured in accordance with the ASTM standard D-5868 [21]. The adherends were made of Garolite G-10 glass-fiber reinforced epoxy. Garolite G-10 was selected due to its low in-plane anisotropy, low thermal expansion coefficient, and high dimensional stability at the ABS processing temperatures. In addition, Garolite was an electric insulator that didn't interact with the applied magnetic field to any appreciable degree. Adherends of the lap-joint had the dimensions of $177.8 \times 25\ mm$ with a thickness of $3.175\ mm$. Bond-line area was $25 \times 25\ mm^2$, and the thickness of the nano Fe_3O_4 reinforced ABS adhesive film was $1\ mm$. Figure 2.1 shows the overall dimensions of the lap-joint along with sensor locations.

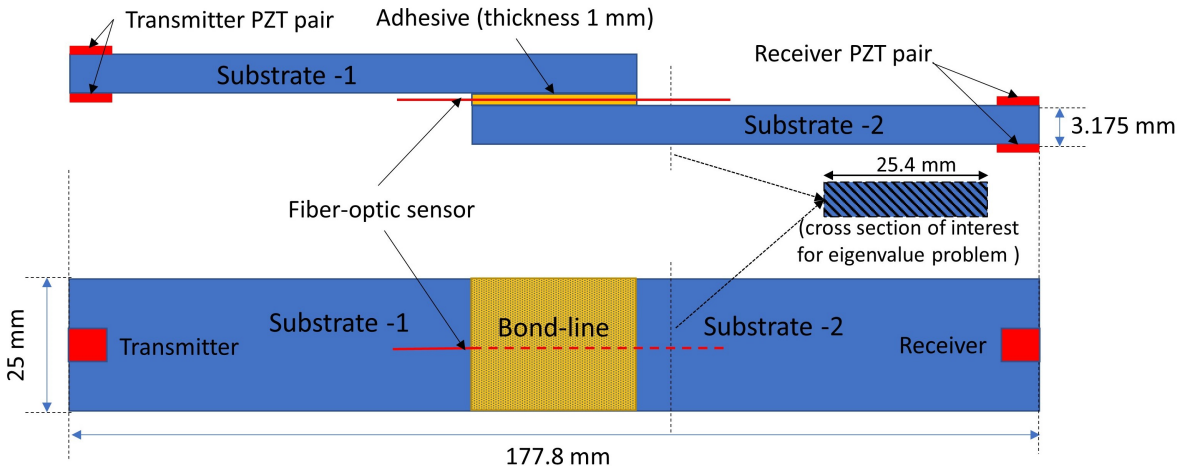

Figure 2.1: Lap-joint dimensions.

Table 2.1 lists the respective material properties of the ABS adhesive and Garolite G-10 adherends. Modulus E and dynamic viscosity ν of the ABS were labeled as known functions of temperature T. However, material properties of Garolite were assumed to be constant in the temperature range between 20^oC and 160^oC.

Material	Property	Value/Function	Unit
Adherend (Garolite)	Young's modulus (E)	20	GPa
	Poission's ratio (ν)	0.3	-
	Density (ρ)	1799	$\frac{kg}{m^3}$
Adhesive (ABS)	Young's modulus (E)	$E(T)$	GPa
	Poission's ratio (ν)	0.35	-
	Density (ρ)	1050	$\frac{kg}{m^3}$
	Dynamic viscosity (η)	$\eta(T)$	$Pa \times s$

Table 2.1: Material properties of Garolite G-10 and ABS adhesive.

Pairs of rectangular lead zirconate titanate (PZT) wafers ($7\ mm \times 8\ mm$) with a thickness of $0.2\ mm$ were bonded to respective edges of the adherends as shown in figure 2.1. PZT wafers were made of PZT-5A Navy Type-2 material from STEMiNC, and had the same resonant frequency of $275\ kHz$. Electrical, mechanical and piezoelectric porperties of PZT wafers can be found in the reference [66]. PZT wafers bonded to one adherend were used as actuators of ultrasonic guided waves, and wafers bonded to the opposite adherend were used as receivers of guided waves as

shown in figure 2.1.

2.3 Eigenfrequency Analysis to Determine Dispersion Relations

Guided waves are elastic waves that can propagate in plate-like structures, bars, rods, pipes, rails and other waveguides of various cross-sections and periodicity. Compared to ultrasonic bulk waves, guided waves are characterized by complex displacement fields or modes. Only certain modes can be supported by the host structure, however there can be multiple at the same excitation frequency. Guided waves are also dispersive, meaning that the phase and group velocities of each mode are functions of excitation frequency. Hence, determining dispersion relations is key in current application, since the goal is to identify modes with large displacements in the adhesive bond-line of the lap-joint.

Dispersion relations for plates can be computed analytically (e.g. using Rayleigh-Lamb equation for isotropic plates [60, 49], Transfer Matrix method or Global Matrix method for classical laminates[53]) based on the assumption that plates have infinite length and width. More sophisticated techniques such as Semi-Analytical Finite Element (SAFE) method [60] were developed for computation of dispersion relations of waveguides with arbitrary cross-sections. In this work, we adopted Floquet-Bloch (F-B) technique ([28]) to identify dispersion curves of the adherends and bond-line region of the lap-joint. The F-B technique doesn't require development of complex numerical scripts and can be easily implemented using commercial FEM software.

The concept of the F-B is to represent a continuous rectangular waveguide with a unit cell and apply periodic displacement boundary conditions on the faces perpendicular to the direction of wave propagation (see fig.2.2). Equation of motion for rectangular waveguide accepts plane wave solutions of the form

$$\mathbf{u}(x, y, z, t) = \mathbf{U}(y, z)e^{i(k_x x - \omega t)}, \tag{2.1}$$

where $\mathbf{u}(x, y, z, t)$ is displacement field, $\mathbf{U}(y, z)$ is mode shape, k_x is wavenumber component in $\hat{x}$ direction, ω is angular frequency and $i = \sqrt{-1}$. Note that $\mathbf{U}(y, z)$ doesn't depend on $\hat{x}$, therefore if we compute the displacement at a distance L from the origin, it will differ from the original

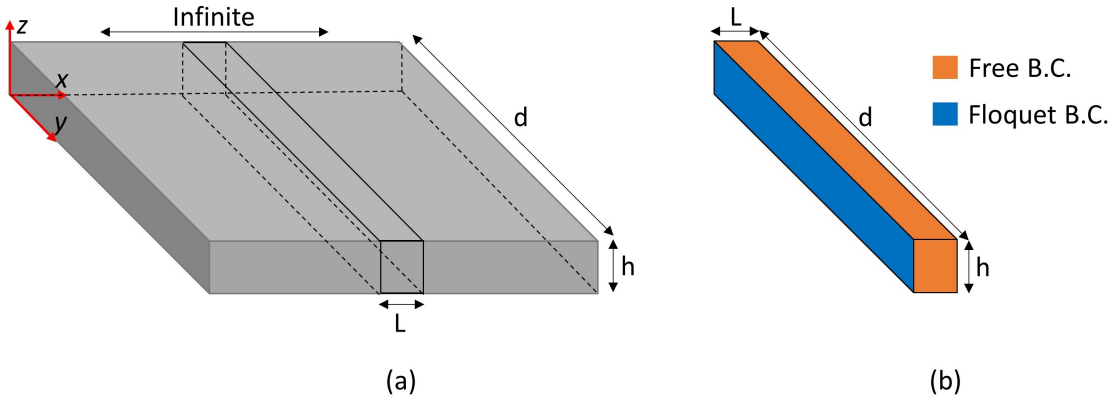

Figure 2.2: Floquet-Bloch theory for computation of dispersion relations of a rectangular waveguide: (a) unit cell; (b) boundary conditions.

displacement only by a phase term:

$$\mathbf{u}(x+L,y,z,t) = \mathbf{u}(x,y,z,t)e^{ik_xL}. \tag{2.2}$$

Since the waveguide is a periodic structure, we can consider its unit cell of length L and apply the Floquet-Bloch theorem:

$$\mathbf{u}_{k_x^{FB}}(x,y,z,t) = \mathbf{U}_p(y,z)e^{i\left(k_x^{FB}x-\omega t\right)}, \tag{2.3}$$

$$\mathbf{u}_{k_x^{FB}}(x+L,y,z,t) = \mathbf{u}_{k_x^{FB}}(x,y,z,t)e^{ik_xL}, \tag{2.4}$$

where $\mathbf{u}_{k_x^{FB}}(x,y,z,t)$ is displacement in the unit cell, $\mathbf{U}_p(y,z)$ is mode shape in the unit cell (also a periodic function in $\hat{x}$), and k_{FB} is the Floquet wavenumber. Floquet wavenumber is related to the original wavenumber as

$$k_x = \frac{2\pi n}{L} + k_x^{FB}, \tag{2.5}$$

where n is an integer and L is the length of the unit cell. Owing to periodicity in Eq.2.4, dispersion relations of the rectangular waveguide and its representative unit cell will be equal only for certain values of k_x^{FB}:

$$\omega(k_x) = \omega(k_x^{FB}) \quad \forall k_x^{FB} \in \left(0, \frac{\pi}{L}\right) \tag{2.6}$$

The high-frequency limit of computation can be adjusted by changing the size of the unit cell L.

The F-B method for finding dispersion relations was implemented in Comsol Multiphysics 5.4. Structural mechanics module was used to conduct an eigenfrequency study. Material properties for FE simulation were the same as in section 2.2. It was assumed that the thermoplastic adhesive was fully cured. Two separate unit cells were created to represent the adherend and bond-line region of the lap-joint as shown in figure 2.3. The unit cells were meshed using tetrahedral elements, and

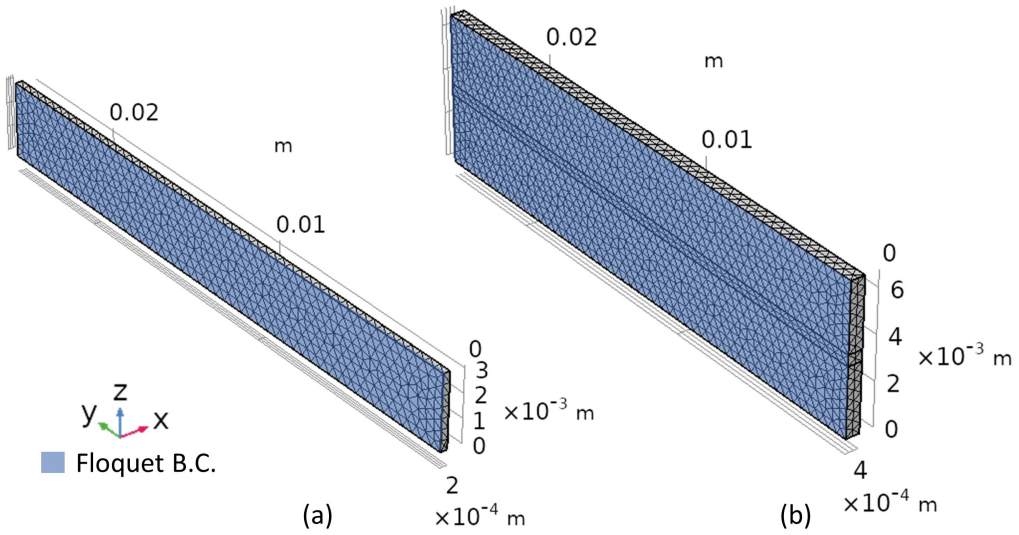

Figure 2.3: Unit cells for computation of dispersion relations using Floquet-Bloch approach: (a) adherend; (c) bond-line region.

periodic displacement boundary conditions were applied to highlighted faces as defined in Comsol Multiphysics 5.4:

$$\mathbf{u}_{dst} = \mathbf{u}_{src} e^{-ik_x^{FB}(\mathbf{r}_{dst} - \mathbf{r}_{src})} \tag{2.7}$$

where, k_x^{FB} is the Floquet wavenumber; $\mathbf{u}_{src}$ and $\mathbf{u}_{dst}$ are displacements at source and destination, respectively; and $\mathbf{r}$ is the spatial coordinate vector. Note that in our case $L = |\mathbf{r}_{dst} - \mathbf{r}_{src}|$.

The Floquet wavenumber k_x^{FB} was parametrically swept while solving for angular frequency $\omega = 2\pi f$ and mode shapes. Corresponding results for the Garolite adherend are shown in figure2.4. There are four fundamental modes in low frequency region under $f = 40\ kHz$, out of which one is longitudinal ($L0$), one is torsional ($T0$) and two are flexural (F_z0 and F_y0).

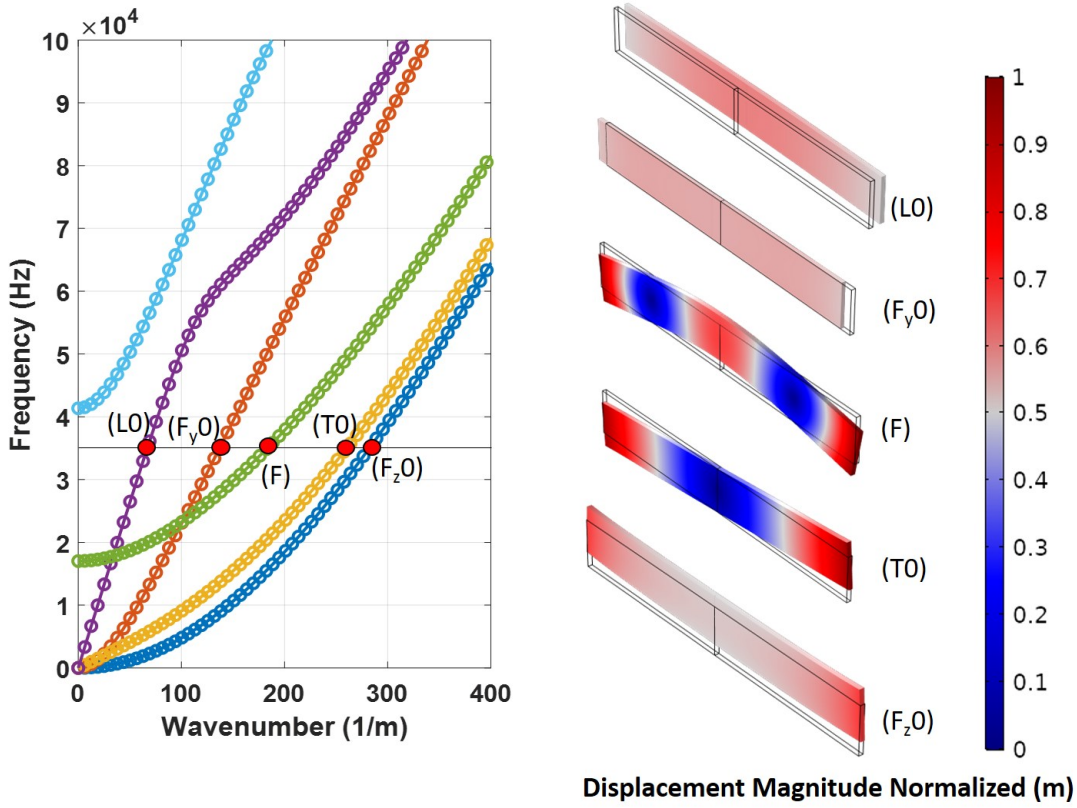

Figure 2.4: Eigenfrequency analysis of the Garolite adherend: (a) wavenumber versus excitation frequency; (b) mode shapes.

Phase c_{ph} and group c_{gr} velocities were computed using the equations 2.8 and 2.9, respectively:

$$c_{ph} = \frac{\omega}{k_x}, \tag{2.8}$$

$$c_{gr} = \frac{{c_{ph}}^2}{c_{ph} - fa\frac{\partial c_{ph}}{\partial (fa)}}, \tag{2.9}$$

where $a = \frac{h}{2}$ is the half thickness of the unit cell. The results are demonstrated in figure 2.5.

The fundamental longitudinal mode $L0$ was selected for excitation in the lap-joint. As shown in Figure 2.5, the $L0$ mode is largely non-dispersive under 40 kHz, which helps preserve the shape of the excitation signal and simplify signal processing. In addition, the $L0$ mode is the easiest to identify among the other modes and reflections in the received signal as it has the highest group velocity. The authors verified that in the low frequency region with only fundamental modes, $L0$ was best excited by square surface-bonded PZT wafers at 35 kHz. The corresponding mode shape

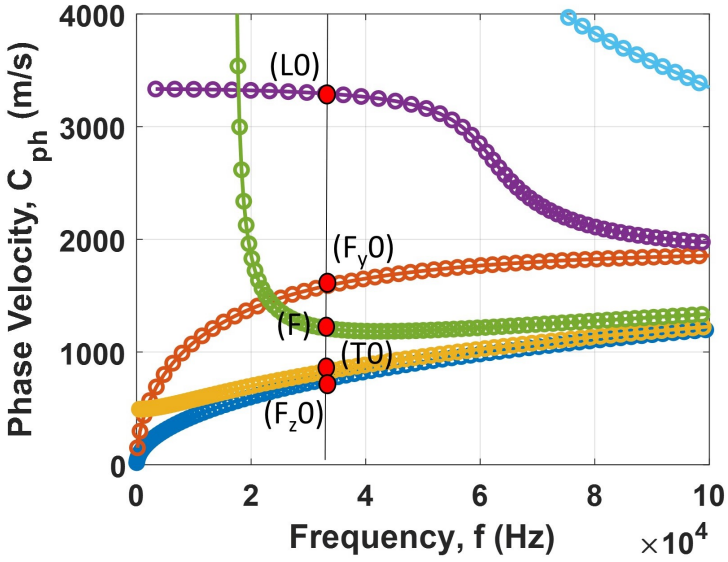

(a)

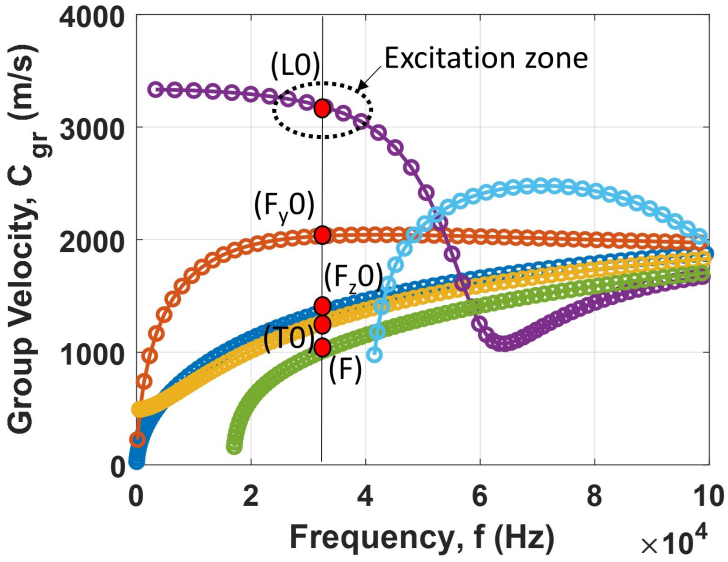

(b)

Figure 2.5: Dispersion curves of Garolite adherend: (a) phase velocity; (b) group velocity.

is shown in Figure 2.6. Figure 2.6 demonstrates that the $L0$ at 35 kHz is characterized by dominant in-plane displacement u_x in the transect of the adhesive bond-line. Strong displacement in the bond-line ensures high sensitivity of transmitted guided waves to adhesive stiffness change.

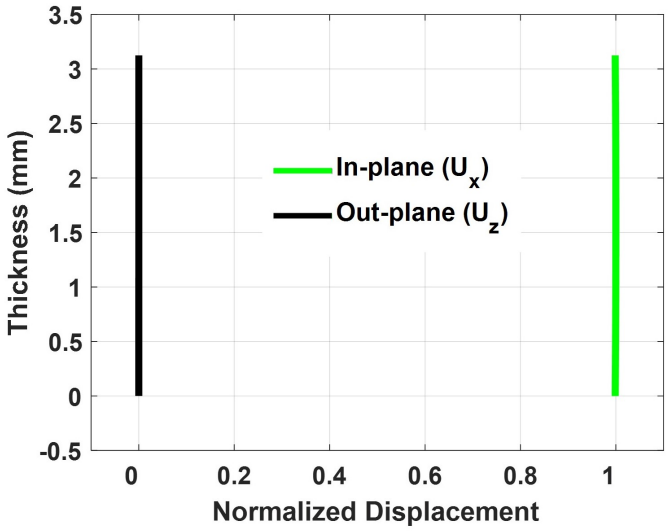

(a)

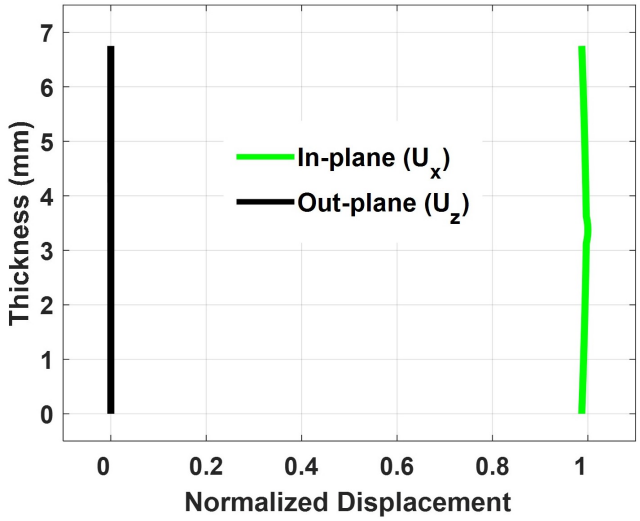

(b)

Figure 2.6: Displacement profile u_x, and u_z for garolite adherend (a) and lap joint (b) in L mode at 35 kHz

2.4 Time-depended Model of Guided Wave Propagation

ABAQUS CAE with Implicit Dynamic Analysis (IDA) was used to simulate the piezoelectric wafers and guided wave propagation across the lap-joint. The geometry of the lap-joint is presented in figure 2.1.

2.4.1 Maxwell Viscoelastic Model of the Adhesive

Adhesive was modeled as a viscoelastic material in order to account for the damping of ultrasonic waves. The generalized 4^{th} order Maxwell viscoelastic model was incorporated into the FE analysis. Equivalent mechanical representation of the viscoelastic model is demonstrated in figure 2.7.

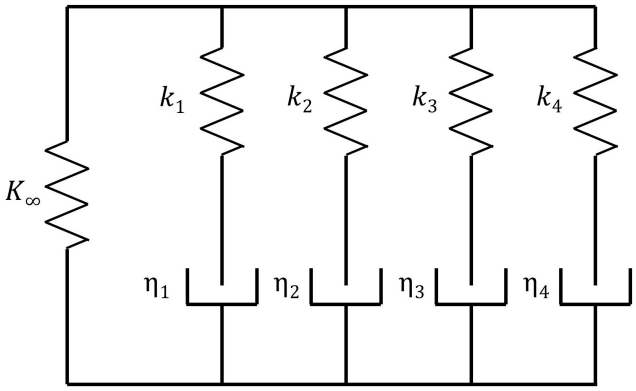

Figure 2.7: Equivalent mechanical representation of Maxwell viscoelastic model.

The bulk and shear relaxation moduli can be expanded in the Prony series [17] as shown in equation 2.10 and 2.11:

$$K(t) = K_\infty + \sum_{i=1}^{4} k_i K_0 e^{\frac{-t}{\tau_i}} \tag{2.10}$$

$$G(t) = G_\infty + \sum_{i=1}^{4} g_i G_0 e^{\frac{-t}{\tau_i}} \tag{2.11}$$

$$G_0 = G_\infty + \sum_{i=1}^{4} g_i \tag{2.12}$$

$$K_0 = K_\infty + \sum_{i=1}^{4} k_i, \tag{2.13}$$

where g_i, k_i and τ_i are Prony parameters [65]. Note that $g_i = \frac{G_i}{G_0}$ is the shear relaxation modulus ratio; $k_i = \frac{K_i}{K_0}$ is the bulk relaxation modulus ratio; and $\tau_i = \frac{\eta_i}{E_i}$ is the relaxation time.

2.4.2 Guided Wave Excitation and Sensing using Surface-bonded PZT Wafers

The voltage signal applied to actuating PZT wafers was the Morlet wavelet with the central frequency f_0 = 35 kHz and V_{pp} = 20 V as shown in figure 2.8. Figure 2.9 illustrates how the top and bottom PZT wafers were driven in phase in order to generate purely $L0$ mode (see figure 2.5).

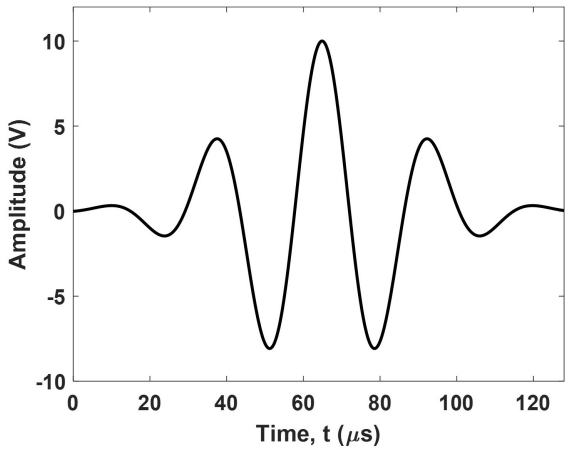

Figure 2.8: Excitation signal (electric potential) applied to actuating PZT wafers.

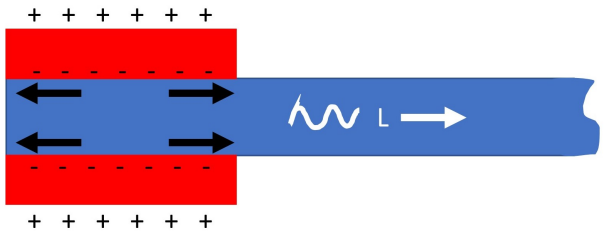

Figure 2.9: Collocated PZT wafer excitation for generation of the $L0$ mode.

2.4.3 FE Model Configuration

Substrate, adhesive, and piezoelecric domain are all defined as part, meshed (Structured), and assembled to form a single lap joint as shown in figure 2.10. The adherends were meshed using first order C3D8 (3D-brick) elements with maximal size of $1 \times 1 \times 0.78$ mm, and the adhesive bond-line was meshed using C3D8R elements with maximal size of of $1 \times 1 \times 0.33$ mm so that the bond-line had at least 3 elements in the thickness direction. PZT wafers were assumed ideally

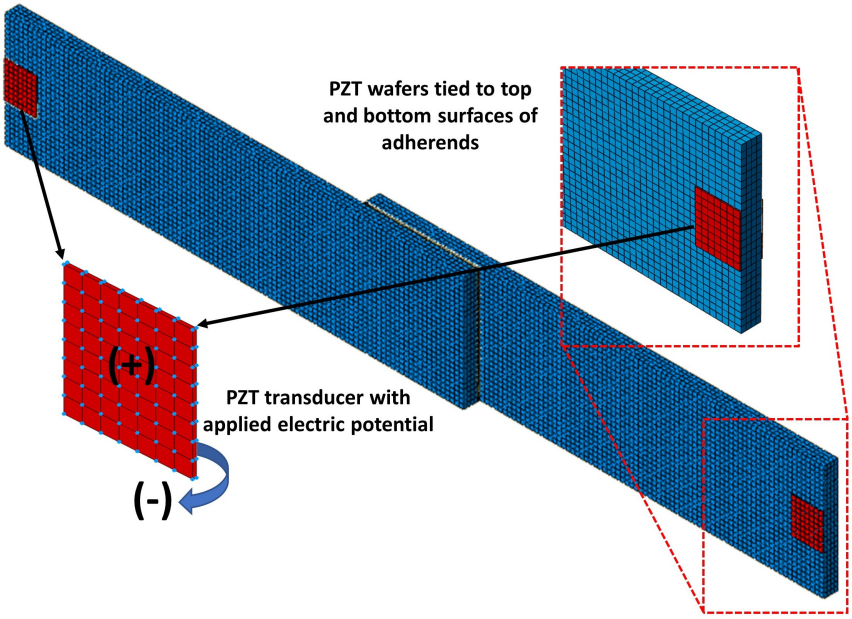

Figure 2.10: Meshed lap-joint geometry in ABAQUS CAE.

bonded to the adherends, and were represented using C3D8E piezoelectric elements with maximal size of $1 \times 1 \times 0.2\ mm$. For the excitation frequency of 35 kHz, selected mesh size provided nearly 92 nodes per wavelength of the $L0$ mode.

The implicit solver was configured to run simulations with fixed 0.1 μs time increments. The von Misses stress and displacements were saved for every time increment in order to create snapshots of the ultrasonic wave field. The parametric study was performed by sweeping through material properties of the ABS thermoplastic adhesive obtained experimentally using the DMA.

2.4.4 FE Simulation Results

The wave propagation in the lap-joint is simulated for the time period of 200 μs. Within this time span, the excited longitudinal mode $L0$ propagates from PZT transmitters across the adhesive bond-line and reaches the PZT receiver pair. Voltages generated by the PZT receivers are summed to reduce the effect of flexural modes on the resulting signal. Guided waves undergo mode conversions while entering and while leaving the adhesive bond-line region. This phenomenon combined with varying thicknesses and different dispersion relations in the substrates and the adhesive bond-line

may render signal analysis complicated. Hence, in this study, the measured GW signal is cropped to include mostly the fastest $L0$ mode, then its energy is monitored in order to evaluate the bond condition [59].

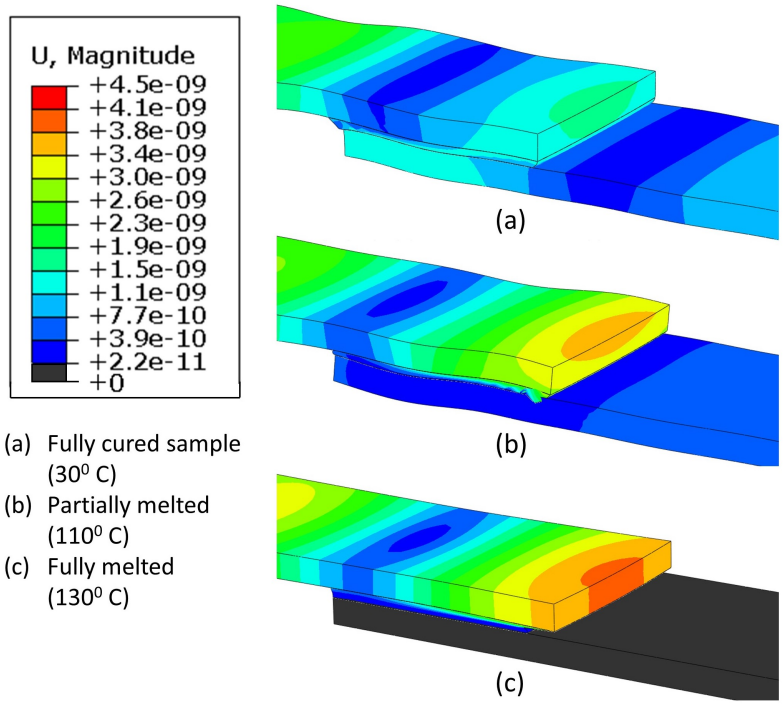

Figure 2.11: Displacement fields in the lap-joint at 90 μs corresponding to different adhesive states: (a) fully cured; (b) partially melted; and (c) fully melted.

Guided wave propagation corresponding to different adhesive states is simulated by changing the elastic modulus E of the adhesive and its dynamic viscosity ν as per experimental DMA results from Figure 1.3 and Figure 1.4. The ABS adhesive at 30 °C, 110 °C and 130 °C will be in a fully cured, partially melted and fully melted state, respectively. Thus, the simulation results at these three temperatures are discussed in detail for better understanding of guided wave transmission through the adhesive bond-line. Figure 2.11 shows snapshots of the corresponding displacement fields in the lap-joint at 90 μs. The energy transfer of guided waves from the top Substrate 1 to the bottom Substrate 2 reduces slightly in the case of partially melted adhesive compared to the case of the fully cured adhesive. However, when the adhesive is fully melted, the energy transfer is nearly zero. In the process of transitioning from the fully cured to the fully melted state, the magnitude

of displacements increases in the top Substrate 1. This indicates that guided waves are trapped in the Substrate 1. They reflect from the top edge in the bond-line region and propagate backwards to the transmitter PZT pair. Similar observations are reflected in Figure 2.12 that demonstrates the voltages generated by the PZT receiver pair.

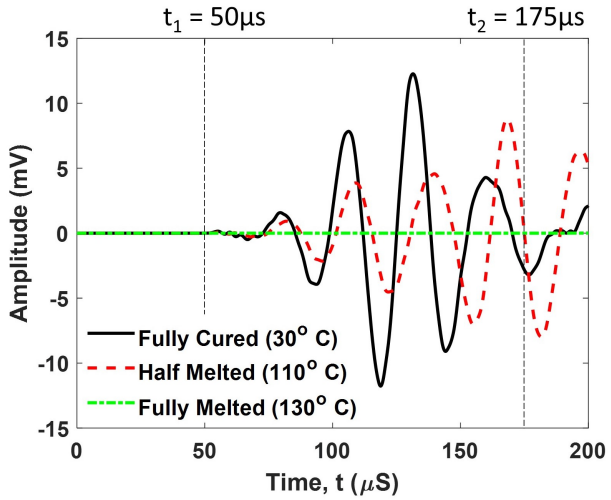

Figure 2.12: Voltage acquired by the receiver transducer pair

Figure 2.13 presents the guided wave transmission coefficient α as a function of the adhesive temperature. In this case, the simulated guided wave signals were cropped between $t_1 = 50\ \mu s$ and $t_2 = 175\ \mu s$ (see Figure 2.12), and α was computed as per the Eq. 4.5 for the frequencies between $f_1 = 10\ kHz$ and $f_2 = 60\ kHz$. The relationship in Figure 2.13 was later used during experiments for the real-time estimation of the adhesive state and temperature from the acquired guided wave signals. Figure 2.14 demonstrates the non-linear dependence of the simulated guided wave transmission coefficient α with respect to the adhesive modulus.

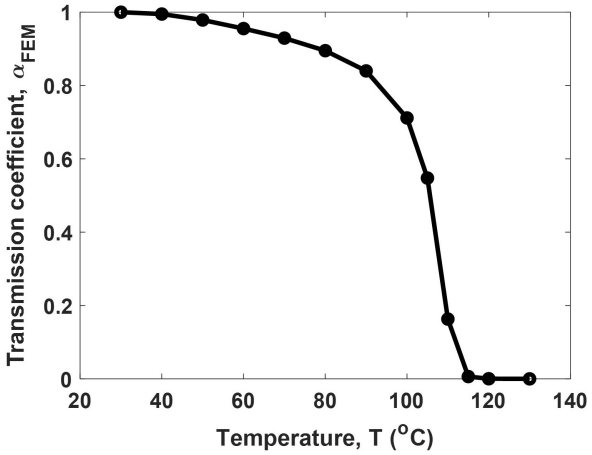

Figure 2.13: Guided wave transmission coefficient, α as a function of the adhesive temperature.

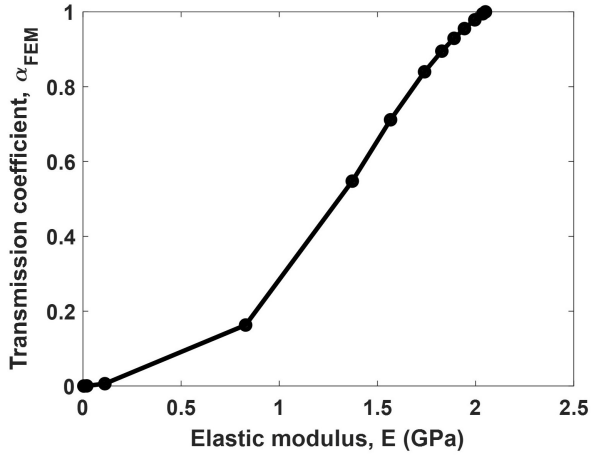

Figure 2.14: Guided wave transmission coefficient, α as a function of the adhesive modulus.

CHAPTER 3

PROCESS MONITORING AND CONTROLLED FABRICATION OF REVERSIBLE ADHESIVE BONDED LAP JOINTS

3.1 Introduction

This chapter presents an ultrasonic guided wave technique for online monitoring of the adhesive state and feedback control of the electromagnetic bonding process. Experiments were carried out on a single lap-shear joint with nano-Fe_3O_4 reinforced thermoplastic adhesive and non-conductive glass fiber reinforced polymer (GFRP) adherends. Ultrasonic guided waves were made to propagate across the bond-line of the joint by exciting and sensing them using miniature piezoelectric wafers. Analysis of dispersion relations and dynamic wave propagation were performed using finite element modeling (FEM). Fundamental longitudinal mode L_0 at 35 kHz was found optimal for bond process monitoring. Mapping between the FE-simulated transmission coefficient of L_0 and actual temperature of the thermoplastic adhesive was established using the DMA test data. Real-time guided wave measurements were used as a feedback in the discrete control of the induction heater so as to provide optimal bonding and prevent adhesive charring. The developed ultrasonic technique was successfully validated by fiber-optic temperature sensing. Single mode optical fiber was embedded inside the adhesive bond-line, and dynamic distributed temperature measurements were acquired using commercial optical frequency domain reflectometer (OFDR). Experiments demonstrated good agreement between guided wave measurements and OFDR system. Overall, the results indicate the potential of guided wave technique for in-situ monitoring and controlled bonding of reversible lap-joints using electromagnetic heating. Further, Lap-joint samples prepared with guided wave controlled system offer better ultimate strength compared to lap-joints processed without guided wave control.

3.2 Experimental Setup for Rapid EM Bonding with Temperature Feedback

The experimental setup consist of separate systems for 1) EM targeted heating of the adhesive, 2) guided wave monitoring of the adhesive state, and 3) OFDR distributed temperature sensing using the embedded optical fiber as shown in figure 3.1. All systems are controlled using a PC and software developed in MatLab. EM system heats up the nano Fe_3O_4 reinforced ABS adhesive

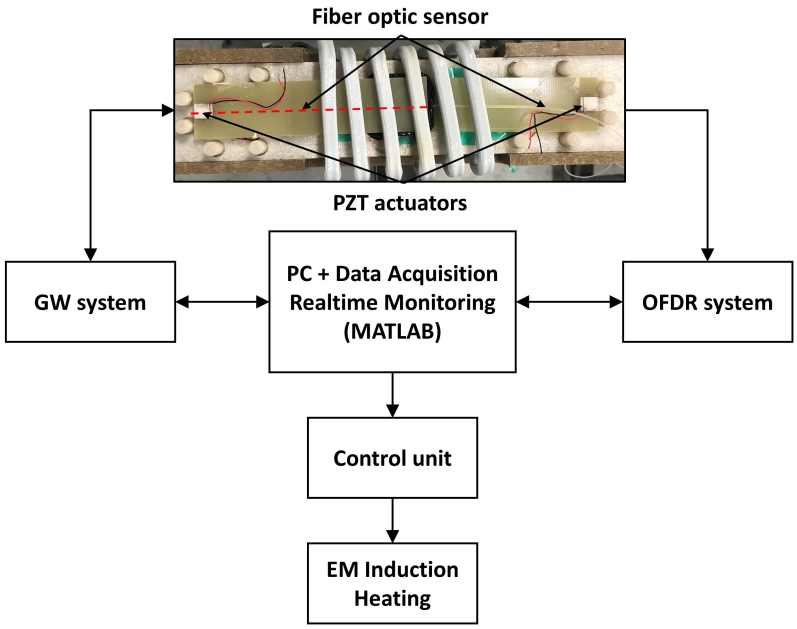

Figure 3.1: Schematic experimental Setup with direction of data and control flow

based on the principles discussed in Chapter 1. The temperature and aggregate state of the adhesive is monitored by registering ultrasonic guided waves transmitted through the bond-line. Application of the electromagnetic field is controlled in a discrete manner. The heater is turned off when guided wave measurements are being acquired, and it turns on for $0.5\ s$ afterwards. The process continues until the optimal melt temperature of the adhesive is reached. A fiber optic temperature sensor is deployed within the adhesive layer in order to validate the acquired guided wave measurements. Ultrasonic guided waves fill the whole cross-section of the bond-line, hence provide the information about the average temperature of the adhesive. In contrast, the OFDR system furnishes localized temperature measurements distributed along the whole length of the embedded optical fiber.

3.2.1 EM Induction Heating System

Electromagnetic heating of nano Fe_3O_4 reinforced ABS adhesive was performed using IHG06A1 induction heater from Across International shown in figure 3.2 (a). Commercial induction heater could operate in the frequency range of 100-500 kHz. It had a maximum active current of 30 A and maximum output power of 6.6 kW. The EM heater was remotely controlled via optically isolated USB relay switch from SMAKN® that was connected to a PC. Remote control allowed for the implementation of the pulse-width modulation (PWM), in which the heater could be turned on and off for short time intervals of 0.5-1 s.

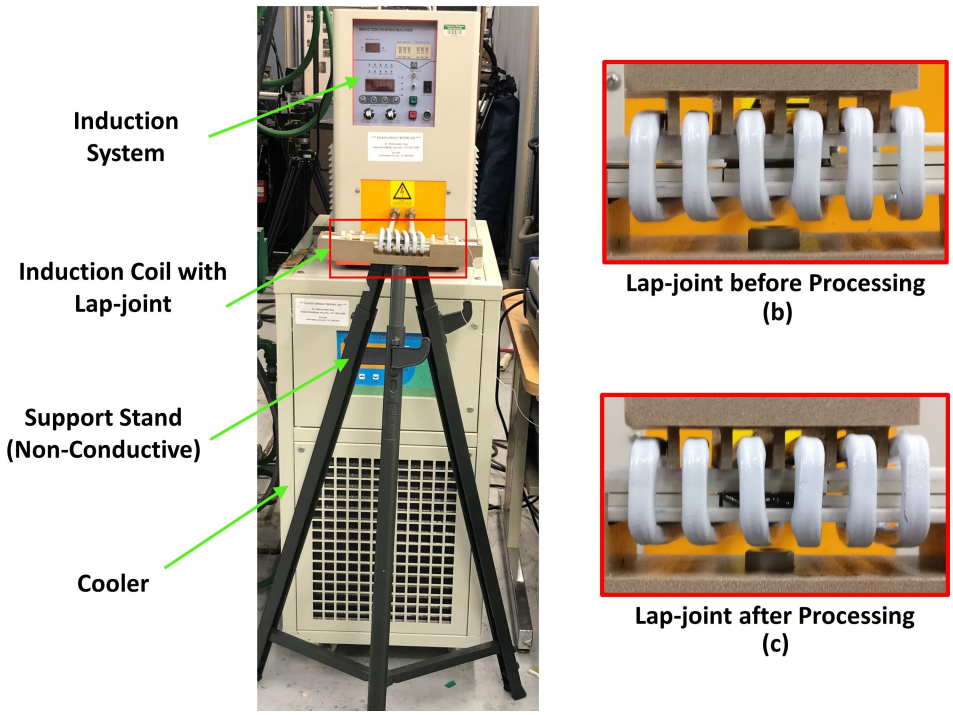

Figure 3.2: (a) Induction processing system with non-conductive supportive stand and fixture. (b) Lap-joint before processing withing the non-conductive ceramic fixture. (c) Lap-joint after processing withing the non-conductive ceramic fixture.

Induction heater was equipped with IHHC 2×1 water cooled rectangular coil (50.8 $mm \times 25.4$ mm). The coil was made of 6 turns of a hollow copper profile with a square cross-section of 6.35 $mm \times 6.35$ mm. Induction heater automatically adjusted the excitation frequency to 200 kHz for optimal impedance matching with the coil. A non-conductive ceramic fixture for holding the

lap-joint was inserted into a coil as shown in 3.2. Guide pins were used to maintain bond-line thickness and align the substrates to prevent them from moving during EM bonding.

3.2.2 GW Measurement System

The block diagram of the guided wave system is shown in figure 3.3. It consisted of 1) PZT wafers deployed on the lap-joint, 2) arbitrary waveform generator 33220A from Keysight Technologies, 3) acoustic emission pre-amplifier, and 4) data acquisition (DAQ) device USB-6255 from National Instruments. PZT wafers were bonded to the Garolite adherends using instant Loctite epoxy. PZT transmitters were electrically connected to the output of the waveform generator. Excitation was done using a Morlet wavelet function with adjustable center frequency, bandwidth and amplitude. Guided waves transmitted through the adhesive bond-line were sensed using PZT receivers, which were connected to the multi-channel acoustic pre-amplifier. Signals from the pre-amplifier were acquired by the DAQ with a sample rate of 1.25 MS/s and no averaging. Data was then transferred to a PC with MatLab for real-time processing. Guided wave measurement system was only activated discretely for approximately 50 ms time intervals when the EM heating was off so as to avoid electromagnetic interference and noise.

In order to simplify the analysis of multi-modal guided wave signals, it was desirable to actuate only one guided wave mode in the adherend of a lap-joint. This was accomplished by frequency tuning and collocated actuation/sensing. Frequency tuning was established by Giurgiutiu et al [27]. The technique helps identify the frequencies that enhance the excitation of certain GW modes while suppressing the excitation of other modes. Frequency tuning is accomplished by analyzing the strain response of a PZT coupled with a host structure. In contrast, collocated actuation/sensing technique requires two PZT wafers symmetrically bonded to different sides of the adherend. When wafers are driven in-phase (the electric field of the same polarity is applied across the similar faces), they apply extension forces to the structure, thus generating only symmetric modes (see fig.2.9). Conversely, if the pair is driven out-of-phase, the host structure is subjected to bending moment, and only antisymmetric modes are actuated.

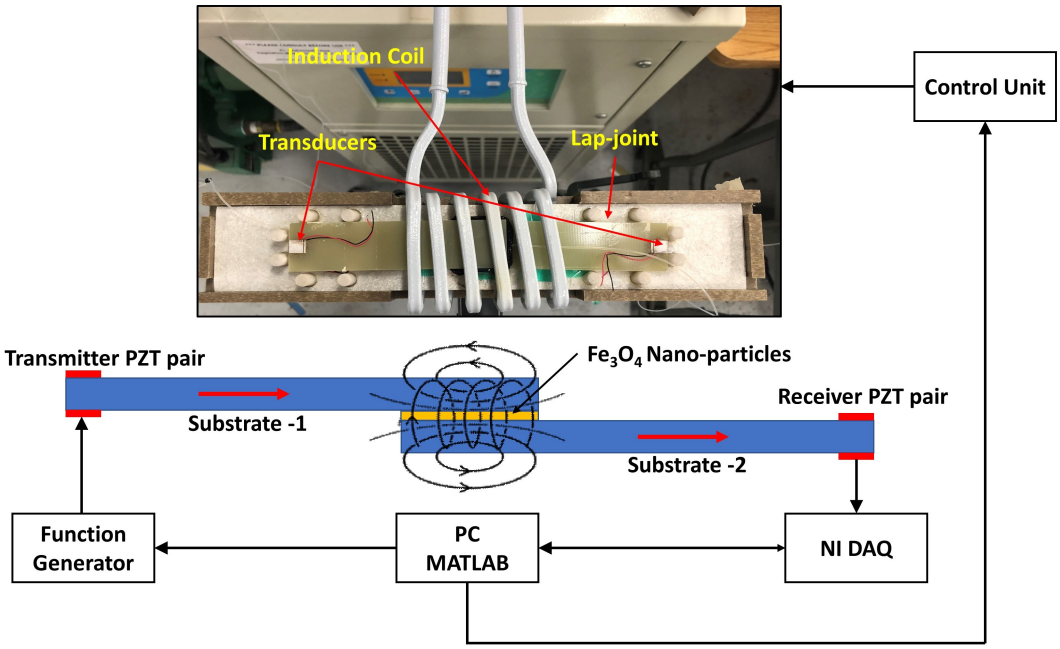

Figure 3.3: Guided Wave system

Guided wave signals acquired at different adhesive temperatures were processed in MatLab in order to estimate their energy spectral density (ESD), E_S:

$$E_S = \int_{f_1}^{f_2} |\hat{s}(f)|^2 df, \tag{3.1}$$

where $\hat{s}(f) = \int_{-\infty}^{\infty} e^{-i(2\pi f)t} s(t) dt$ is the Fourier transform of the acquired and cropped signal $s(t)$, and f_1 and f_2 are the lower and upper frequencies selected for the analysis, respectively. Then the guided wave transmission coefficient α was evaluated for each signal as:

$$\alpha^{(n)} = \frac{E_S^{(n)}}{E_S^{(0)}}, \tag{3.2}$$

where $E_S^{(n)}$ is the ESD of the n-th guided wave signal acquired at adhesive temperature $T^{(n)}$, and $E_S^{(0)}$ is the ESD of the baseline signal acquired with fully cured adhesive at room temperature $T^{(0)}$. Note that $T^{(n)} > T^{(0)}$ during EM heating, but $\alpha^{(n)} < \alpha^{(0)}$ as adhesive heats up and transitions from solid to viscoelastic state. The condition for stopping the EM heating process was

$$\alpha_{STOP}^{(n)} = 0.05\alpha^{(0)}. \tag{3.3}$$

In this case, the developed software would send an OFF command to the relay controlling the heater. The 5% threshold accounted for electric noise in guided wave measurements and small acoustic energy transferred via ceramic fixture bypassing the adhesive bond-line of the lap-joint.

3.2.3 OFDR Measurement System

In order to measure the temperature of the adhesive, a fiber-optic sensor from Luna Innovations was embedded into the center of the adhesive bond-line as demonstrated in figure 2.1. The sensor was a free single mode fiber (SMF) inserted into an insulating polymer tube with outer diameter of 1 mm. Distributed temperature measurements in the bond-line were acquired using Luna ODiSI-B optical frequency domain reflectometer (OFDR). Luna ODiSI-B OFDR system operated based upon Raleigh back-scattering in SMF. Temperature profiles along the fiber length were acquired at 10 Hz and with a spatial resolution of 1.5 mm. The OFDR system was calibrated with respect to the ambient temperature prior to EM bonding.

3.3 Experimental Results and Discussion

Reversible bonding was performed on the lap-joint with Garolite adherends and nano-Fe_3O_4 reinforced thermoplastic ABS adhesive (see Figure 1.5). The fully cured lap-joint was placed inside the inductive coil with electrically insulating fixture, and the thermoplastic adhesive was remotely heated using the electromagnetic system with PWM described in Section 3.2.1. In order to monitor the melting and curing processes, the ultrasonic measurements were acquired by sensing guided waves propagating through the adhesive bond-line as explained in Section 3.2.2. Concurrent measurements of temperature distribution within the adhesive bond-line were acquired using the embedded fiber-optic sensor and the OFDR technique. OFDR distributed temperature sensing using LUNA ODiSI-B instrument served as a validation for the proposed guided wave technique. Guided wave signals were acquired in real-time and the transmission coefficient of the $L0$ mode, α was converted into the elastic modulus of the adhesive, E using FE results from Section 2.4.4 in order to provide the estimate of the adhesive state. Ultrasonic measurements were used as a

feedback to prevent adhesive degradation by stopping the EM heating, when E was close to zero (see Eq. 3.2.1).

Additional experiment was performed for a reference. In the reference experiment, the EM heater was activated manually, the PWM was disabled, and there was no feedback in the form of guided wave sensing. Only the OFDR temperature measurements were acquired in order to estimate the time it takes for the adhesive to develop damage due to over-heating.

3.3.1 Fiber-optic Sensing

The optical fiber sensor was embedded in the adhesive bond-line of the lap-joint as shown in Figure 2.1 and Figure 3.1. LUNA ODiSI-B system provided distributed temperature measurements along the whole fiber length with the spatial resolution of 1 mm. It should be noted that the measurements of temperature distribution inside the adhesive bond-line were by no means comprehensive, since only a single section of the optical fiber was utilized, and no other segments of the fiber were routed in the perpendicular direction. However, the acquired OFDR data was sufficient for validation of guided wave sensing.

Multiple temperature profiles in the embedded section of the optical fiber were acquired over the course of EM heating and cooling of the adhesive. Each distributed measurement was later averaged over the length of the embedded section of the fiber in order to provide an integrated temperature estimate of the adhesive bond-line. The obtained OFDR results are demonstrated in figure 3.4.

In the reference case of EM heating with no feedback control and no PWM (red curve in Figure 3.4a), the average adhesive temperature reaches a critical value of 140°C within about 15 s. This indicates that the melting process is rapid and may be difficult to control manually. Overheating of the adhesive above 140°C would lead to its thermal degradation and reduced load carrying capacity of the lap-joint. On the other hand, if guided wave sensing is enabled and the EM heating is controlled using PWM, the melting process is stopped when the average temperature in the adhesive is just over 130°C (see black curve in Figure 3.4a). Note that the adhesive cooled down

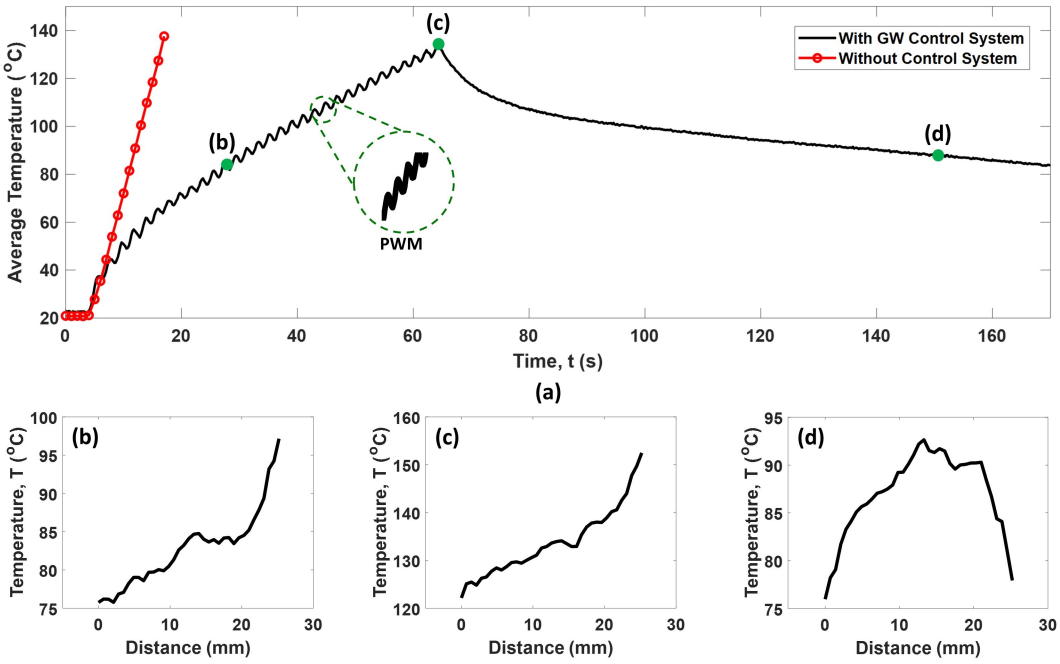

Figure 3.4: Distributed temperature measurements in the adhesive bond-line using LUNA ODiSI-B OFDR system and embedded SMF optical fiber: (a) average temperature along the embedded section of the optical fiber as a function of time; (b) temperature distribution at t = 30 s; (c) temperature distribution at t = 65 s; and (d) temperature distribution at t = 150 s.

and cured completely at around 450 s, and only the first 170 s of the process are shown in Figure 3.4a. Periodic variations of temperature during the EM targeted heating of the adhesive at 5-65 s are caused by the PWM.

Figure 3.4b, Figure 3.4c and Figure 3.4d demonstrate temperature profiles in the adhesive at different stages of the EM bonding. Temperature distributions in Figure 3.4b and Figure 3.4c correspond to the heating stage. The authors suggest that the non-uniformity of these profiles is likely caused by: 1) the non-uniform distribution of Fe_3O_4 nanoparticles during manufacturing, or 2) local agglomerations of nanoparticles inside the adhesive as they are displaced by the applied electromagnetic field. Temperature profile in Figure 3.4d corresponds to the cooling stage. This profile is largely determined by convection heat loss, since the adhesive is approximately 15°C hotter in the center of the bond-line compared to the edges.

3.3.2 Guided Wave Sensing

The $L0$ mode at 35 kHz was excited in the Substrate 1, and resulting guided waves were sensed in the Substrate 2 using the surface-bonded PZT wafers as described in Section 3.2.2. Guided wave propagated across the adhesive bond-line of the lap-joint at all stages of the EM heating process. Figure 3.5 shows the signals acquired by the receiving PZT pair. The amplitudes of transmitted guided waves reduced as adhesive melted.

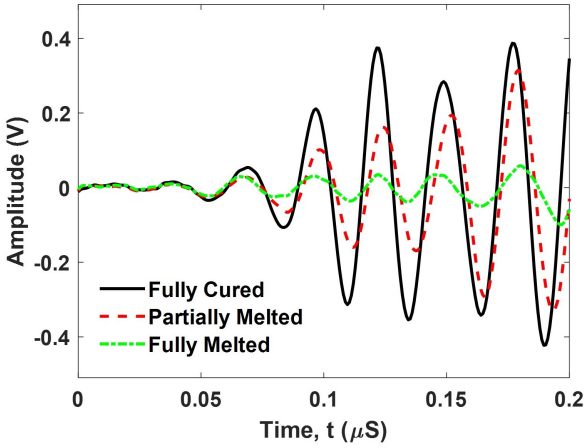

Figure 3.5: Experimental received signal at different adhesive state

Overall, obtained results agreed well with FE models from Section 2.4.4 (see Figure 2.12) in terms of capturing the dependence of the transmission coefficient on the adhesive state. However, shapes of the experimental and simulated guided waves signals were slightly different owing to 1) the assumption of ideal bonding of PZT wafers in the models; 2) mismatch between the assumed and actual material properties of adhesive and adherends; 3) the assumption of uniform temperature distribution in the adhesive; and 4) minor variations of lap-joint geometry and placement of PZT wafers compared to the original CAD drawings.

Figure 3.6 shows the transmission coefficient, α computed for measured signals using Eq. 2 and Eq. 3. The nano-Fe_3O_4 reinforced adhesive was fully melted after 70 s of EM heating with PWM as α reduced to nearly zero. After the heater was disabled, the adhesive started to cool down and returned back to the solid state.

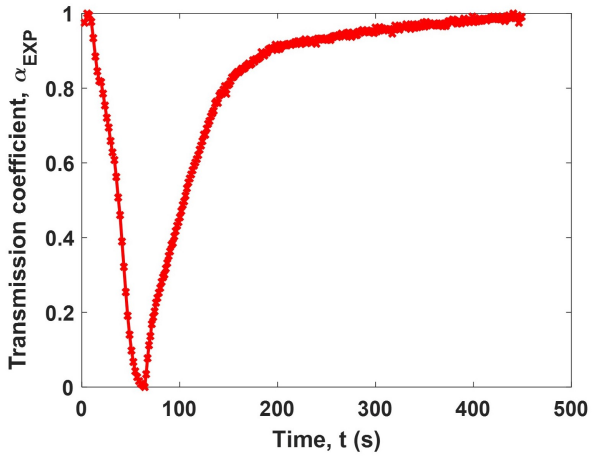

Figure 3.6: Experimental guided waves transmission coefficient (α_{EXP}) during adhesive processing

3.3.3 Comparison of Guided Wave and OFDR Sensing

The average temperature in the embedded section of the optical fiber (see Figure 3.4) was converted to the elastic modulus, E using the DMA data for the ABS adhesive. Since, the DMA provided the elastic modulus only for a few temperature values (see Figure 1.3), a linear interpolation was performed on DMA curve in order to map all OFDR temperature averages. Black curve in Figure 3.7 shows the elastic modulus, E estimated using the OFDR system. Similarly, the elastic modulus, E was computed from guided wave transmission coefficient α_{EXP} (see Figure 3.6) using DMA (see Figure 1.3) and FE simulations from Section 2.4.4. The corresponding result is presented in Figure 3.7 as a red curve.

The elastic modulus estimated with the help of both sensing modalities reduced from it's original value to nearly zero when the adhesive was completely melted, and slowly raised while the adhesive was cooling and curing. This behavior confirmed solid-to-viscoelastic and viscoelastic-to-solid transitions observed visually during the experiments. Hence, guided wave and OFDR techniques successfully captured critical aspects of adhesive processing and helped prevent adhesive degradation. Both techniques can be effectively used for real-time monitoring of EM bonding of FMNP-reinforced thermoplastics. Minor differences between the two curves in Figure 3.7 are explained by the assumptions made in the FE modeling of guided wave propagation as mentioned

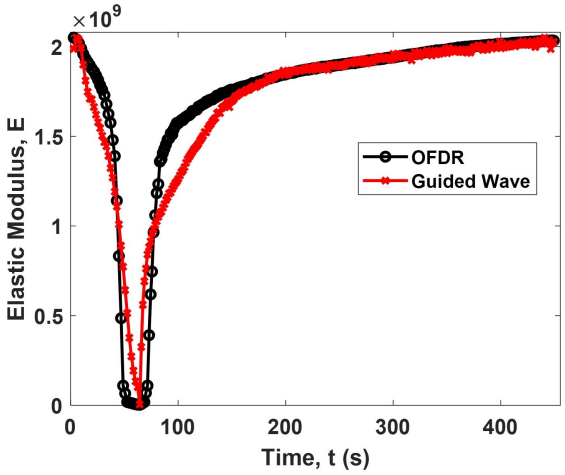

Figure 3.7: Elastic modulus of nano-Fe_3O_4 reinforced ABS adhesive estimated using guided wave sensing (black curve) and OFDR sensing (red curve).

in Section 2.1, as well as by the fact that the temperature inside the adhesive was measured only along one segment of the embedded optical fiber.

3.4 Mechanical Testing and Validation

In this section, we are mechanically testing the EM bonded samples prepared with and without guided wave control. To perform a shear strength comparison a new bond line needs to be prepared. In this chapter, we assessed the ability of guided wave technique to monitor the phase change of the adhesive during induction bonding. It is important to note that while preparing a new bond line, initially there is no transfer of stress wave across the bond line as the adhesive is not melted yet and are not chemically bonded to the substrate. Thus, a small amount to uncontrolled intermittent heating is applied as shown in figure 3.8. It can be seen that there is a $20s$ of intermittent heating to achieve initial melting of adhesive strips. The initial heat is only for a short period of time thus it does not create any adhesive degradation. The process monitoring system developed in section 3.2.2 is modified to wait for $100s$ and monitor the energy transmission coefficient T_c across the bond-line. If the T_c value did not reach 90% of reference T_c value, then the heating cycle is repeated. the reference T_c is measured using an oven bonded joint. Figure 3.8 shows the lap-joint took three heating cycles to achieve 90% of reference T_c value. Most samples achieve 90% of reference T_c

value within three heating cycle.

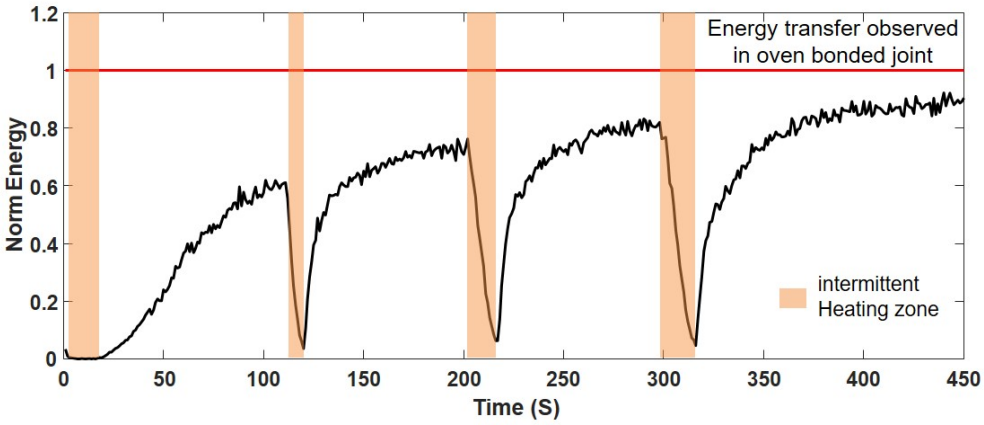

Figure 3.8: Preparation of new bond line using controlled induction heating technique

From figure 3.8 it can be seen that the duration of heating for each heating cycle increases as T_c value increases, this indicates that after each heating cycle there are more area of chemical bonding then the previous cycle.

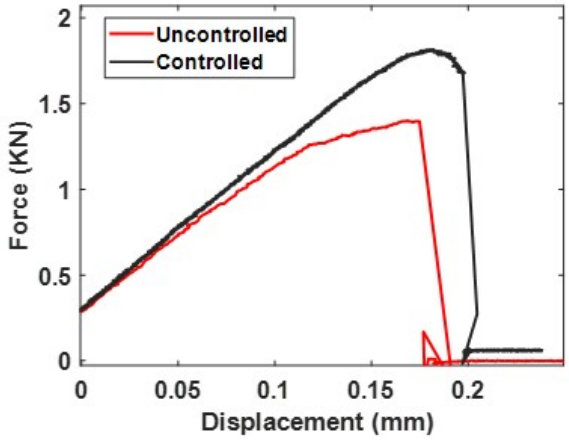

Figure 3.9: Representative load vs displacement comparison of lap-joints process with and without GW control

Samples prepared with and without GW controlled processing are tested in Mechanical Testing System for ultimate shear strength. Monotonic lap-shear tests are conducted in the MTS machine at the rate of $0.1mm/min$ as shown in figure 3.9. It can seen that the lap-joint processed by GW control shows much higher ultimate strength and also higher displacement to failure. This clearly

indicate the effectiveness of controlled heating. Figure 3.10 shows Mean and variance of ultimate strength comparison between lap-joints process with and without GW control. The low variance observed in the controlled processing indicates the reliability and uniform heating of samples.

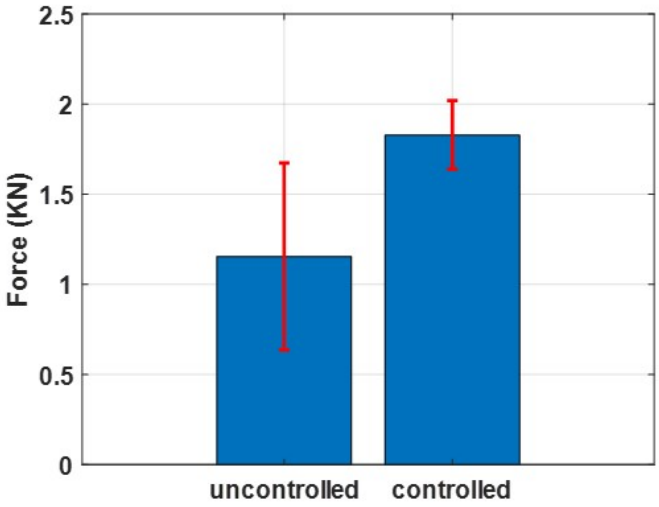

Figure 3.10: Mean and variance of ultimate strength comparison between lap-joints processed with and without GW control

3.5 Summary and Conclusion

Ultrasonic guided wave sensing and optical frequency domain reflectometry were successfully implemented for real-time monitoring of melting and curing processes in a Garolite lap-shear joint with nano-Fe_3O_4 reinforced ABS adhesive. The thermoplastic adhesive was remotely heated at 200 kHz with the help of a 6.6 kW commercial induction heater and a water-cooled solenoid. The embedded FMNPs interacted with the applied electromagnetic field by generating heat due to hysteresis losses and eddy currents between locally agglomerated nano-particles. The electromagnetic system was controlled using pulse-width modulation and was programmed to terminate the heating process based on guide wave measurements so that the adhesive wouldn't suffer thermal degradation.

Guided waves were excited and sensed using surface-bonded PZT wafers on both adherends. Dispersion relations corresponding to the adherends and the bond-line region were obtained in

Comsol Multiphysics 5.4 based on the Floquet-Bloch theory. The state of adhesive was actively monitored by passing the fundamental $L0$ mode at 35 kHz across the bond-line from one adherend to another. The $L0$ mode was selected due to its high sensitivity to material properties of the adhesive and its high group velocity that helped simplify signal processing. Ultrasonic wave propagation was simulated in Abaqus CAE 6.14 in order to map the transmission coefficient of the $L0$ mode to the Young's modulus of the adhesive. In FE modeling, the nano-Fe_3O_4 reinforced ABS plastic was simulated as a viscoelastic material, and it's properties were obtained experimentally using the dynamic mechanical analysis. A non-linear relationship between the Young's modulus of the adhesive and the FE transmission coefficient of the $L0$ mode was later applied to experimental guided wave signals.

In addition to guided wave measurements, distributed measurements of temperature within the adhesive bond-line were successfully acquired using the strategically embedded optical fiber. A Rayleigh back-scattering OFDR system ODiSI-B from Luna Innovations provided temperature profiles of the adhesive at a rate of 10 Hz and with a spatial resolution of 1.5 mm. Measured temperature distributions were averaged along the length of the embedded section of the optical fiber. Then, similarly to the guided wave technique, temperature averages were converted to the Young's modulus of the adhesive based on the DMA data.

The advantages of EM bonding with guided wave and fiber-optic feedback were successfully demonstrated in the experiments with a manufactured lap-joint specimen. Implementing guided wave and fiber-optic sensing provided real-time monitoring of the adhesive state by displaying the effective Young's modulus of the adhesive. Both techniques accurately captured a transition from a solid to a viscoelastic state at which the modulus dropped down to nearly zero values. At that stage, the EM heating was automatically disabled at a prescribed temperature of 130°C to avoid thermal damage. In addition, guided wave and fiber-optic systems correctly sensed the curing of the adhesive after the EM field was removed. As the lap-joint was let cool down to the room temperature and eventually turned solid, measured Young's modulus of the adhesive went up to its original value observed before EM heating. Obtained experimental results demonstrated the

stability of the proposed EM bonding process. Mechanical validation test results indicate that the bondlines processed with GW control offer better ultimate strength compared to uncontrolled processing.

CHAPTER 4

DIAGNOSIS AND PROGNOSIS OF FATIGUE DAMAGE IN LAP JOINT

4.1 Introduction

Composites have been widely utilized in aviation, automotive and marine industries due to their excellent properties of light weight and high tensile stiffness. Unlike mechanical fasteners or rivets in metallic components, composite structures prefer adhesively bonded joints which not only maintains low weight but also distribute the force over larger areas thereby avoiding stress concentrations. This extends the overall life cycle of a composite structure. However, fatigue degradation often leads to formation of cracks or disbonds in the adhesive layer which reduces the load carrying capacity of the joint. An unmonitored adhesive joint may be detrimental to a composite structure if not replaced or repaired on time. Hence, efficient non-destructive evaluation (NDE) technology is required to detect disbonds in adhesive joints and ensure reliability of the complex structures.

In recent studies, guided waves(GW) have been demonstrated as a potential NDE technique for monitoring disbonds in lap-joints of fiber-reinfored polymers [57, 61]. The propagation of guided waves in adhesively bonded lap joints and the influence of bond conditions in wave parameters have been thoroughly studied in the past [34, 40, 63, 64]. Recently, researchers used guided wave sensing to detect dis-bonds, cracks, post-cure and perform in-service monitoring [16, 24, 25]. Further, behavior of guided wave in lap-joint fatigue loading is studied by Karpenko et al., [37]. Most of the studies in lap joints are conducted to monitor the changes in guided wave features with damage propagation. There are minimal efforts in incorporating guided wave for prediction and estimation of remaining useful life in lap-joints.

The primary challenge of prediction of remaining life in lap joints is that the physics behind damage propagation in adhesively bonded structures is extremely complex and highly dependent on the geometry, ply layup, dimensions and material property. In order to accurately compute

fatigue life of a lap joint, each time a new bonded joint has to be monitored, its corresponding FEM model needs to be developed. Some modeling approaches have been performed to understand the stress distribution and damage mechanism [2, 52]. Besides, all loading forces need to be accurately modeled. If one or more physical phenomenon or parameters are overlooked, the prediction results may be highly discrepant from the true state of the structure. Hence, it is imperative to utilize periodic NDE or Structural Health Monitoring (SHM) data to track and predict fatigue damage in composite lap-joints in addition to physics based knowledge. Similar studies have been proposed before where residual stiffness of composite coupons were computed based on Paris-Paris law coupled with data from GW and optical NDE systems [8].

Current health status of a system or structure can be defined by a health-index (HI) which changes with time (or load cycles) as structural health detoriates. Damage propagation path or HI-time curve can be estimated using either model-based or data-driven approaches or a hybrid of both. Model-based methods predict the equipment health condition using component physical models, such as finite element (FE) models, or damage propagation models such as Paris-Ergodan law based on damage mechanics [54]. Kacprzynski et al. [36] presented a prognosis tool using 3D gear FE modeling to study damage inititation and propagation in helicopter gears. Li and Lee [41] proposed a gear prognosis approach based on FE modeling to estimate Fourier coefficients of the meshing stiffness expansion. The strip-yield model included in the NASGRO software developed in [62] is widely used to simulate crack growth under variable amplitude loading. Such methods extract model parameters depending on structural properties and generally do not use condition monitoring data for prediction of damage evolution. Although CBM data is used in hybrid prognostic methods, lack of knowledge of physics-based models especially in newer composites often hinders accurate prediction of damage status. Unlike metals, composites are heterogenous in nature whereby a slight change in their material or geometry can result into an entirely different and complex damage mechanism which may not adhere to known physical models. As a result in most cases, prognosis based on periodic inspection data is the only available choice for prediction of damage in composite structures.

Data-driven prognostic methods models the relationship between damage status and condition-monitoring or NDE data by training the prognostic system on historical inspection data. Gebraeel et al. [26] used Artificial Neural Network (ANN) for monitoring rolling bearing elements and predicting fatigue crack propagation from vibration-based degradation signals. Hu et al. proposed ensemble data-driven prognostic approach which combines multiple member algorithms with a weighted-sum formulation for predicting RUL of electronic cooling fan units [31]. Accuracy of these methods strongly rely upon the training data characteristics and they may fail to produce accurate prediction if insufficient or under-representative data are used.

In general, data-driven methods estimates the 'best' fitted HI-time curve based on all the inspection data collected upto current time, as shown in Fig 1. This may often lead to overfitting on the training data especially since NDE measurements are often noisy. In such cases, prediction of future damage states is significantly different from the ground truth. In order to tackle this challenge, Bayesian inference [3] in a sequential Monte Carlo process can be implemented wherein the data fitting parameters are updated sequentially at every instant a new inspection data is reported instead of using them all at once. Such a dynamic framework enables incorporation of measurement noise and uncertainties in composite properties which can avoid overfitting leading to lower prediction error.

In this research work, dynamic framework for data-driven prognosis of fatigue damage growth in adhesively bonded lap-joint is presented. guided wave(GW)[78] sensing and optical technique are used for NDE of damage introduced in a lap-joint sample by cyclic fatigue loading. The guided wave signals are generated through surface-mounted piezo electric transducers (PZT) which enable on-line monitoring of bond-line while they are in use. Displacement and force information from Mechanical Testing System (MTS) have high accuracy of damage estimation. Hence, damage area computed from MTS are considered as the ground truth. Prediction results of static and dynamic methods combined with GW data are compared with the ground truth to assess their prognostic capability

4.2 Damage Mechanism and Damage Growth Model

In this paper, single lap joints (SLJ) are chosen to demonstrate the ability of single sensor based shear fatigue prognosis. Damage mechanism of SLJ under tension-tension fatigue loading is well studied in the past [1]. Based on these studies fatigue loading in SLJ might be complex, however the damage mechanism is straight forward. The crack initiation and propagation is the main source of fatigue failure. The crack growth indirectly represents the reduction in area of stress transfer. In other words, the crack growth can be converted to damage area by knowing the dimension of SLJ as shown in figure 4.1

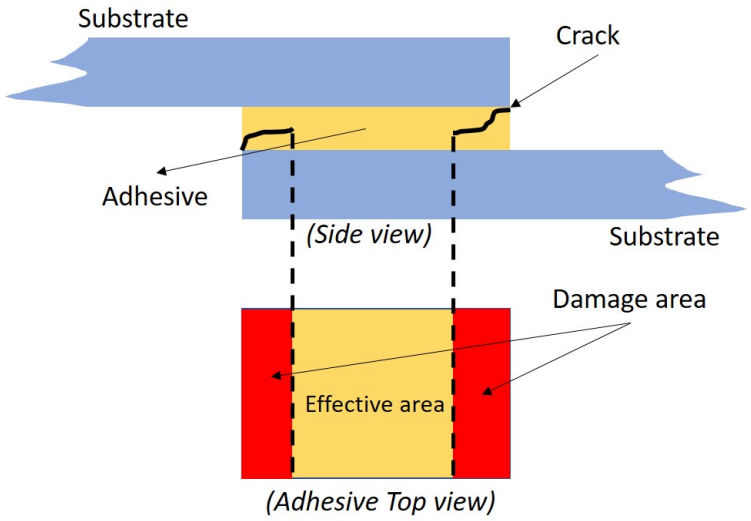

Figure 4.1: Damage and effective adhesive area with fatigue crack

Damage area shall be estimated directly using force and displacement information from mechanical testing device (MTS). E, according to equation 4.1 where, A_{Damage} is the Damage area (m^2), $A_{pristine}$ is the original undamaged joint area (m^2), F is the force applied to the lap joint (N), δl is the change in displacement for the applied force F and G is the shear modulus (N/m^2). Damage area being the crucial factor to decide on remaining useful fatigue life, GW sensors are deployed to monitor the damage area as it propagates. Damage area obtained from MTS testing system remains as ground truth for prognosis.

$$A_{Damage} = A_{pristine} - \frac{Fl}{\delta l G} \tag{4.1}$$

4.3 Modal Analysis

Crack initiation and propagation are not identical from one sample to other. They are highly random and depends on various factors such as micro cracks in adhesive, surface preparation etc., Due to the complex interaction of guided wave with different crack nature dispersion analysis performed in chapter 2 is not a viable solution for selecting a particular frequency and mode-shape that is sensitive to fatigue damage. Thus, we require a investigate the wave propagation using simulation or experiments. In this section, the interaction of guided waves with different crack length is explored numerically and experimentally. The best excitation mode and frequency for fatigue damage monitoring is selected.

4.3.1 Numerical Modal analysis

The aim of these simulations are to understand the interaction of different GW modes at different fatigue damage state. Three parameter are selected for this purpose 1) Excitation mode: fundamental symmetric ($S0$) and Asymmetric ($A0$) mode. 2) Crack length: The lap joint is assumed to have symmetrical crack formation at stress concentration areas as shown in Figure 4.1 with crack lengths such as 2, 4, 6 and 8 mm. 3) Excitation frequency: Seven different frequencies such as 25, 35, 45, 55, 75, 85 and 95 kHz are considered. In total, 70 simulations (including pristine lap-joint) are conducted to analyze the GW modal sensitivity towards fatigue damage. It would be computationally expensive to conducting 70 3D full model simulation, thus a simplified 2D model of lap-joint described in section 2.2 is considered.

Substrate is defined as part, meshed (Structured), and assembled to form a single lap joint as shown in Figure 4.2. Adhesive is replaced as cohesive zone which connects both the adherends in joint location. Cohesive zone properties are obtained through tensile lap-shear FEM calibration. The cohesive zone contact length is adjusted to simulate different crack length. For excitation

of GW, piezo-ceramic transducers are replaced with displacement boundary conditions. Nodal displacement history are recorded at the receiver transducer pair.

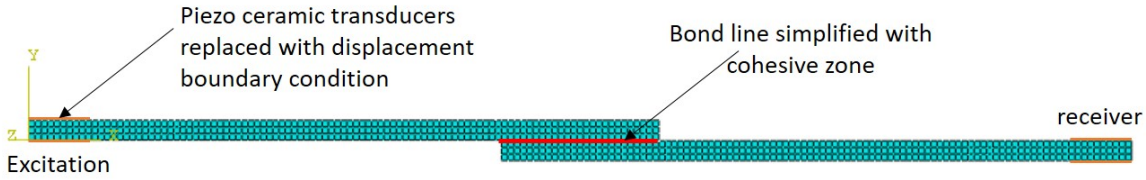

Figure 4.2: Simplified 2D lap-joint geometry in ABAQUS CAE.

ABAQUS CAE with Implicit Dynamic Analysis (IDA) was used to simulate guided wave propagation across the lap-joint. Input signal in the form of Morlet wavelet with varying central frequency and peak displacement of 10 μm is applied to the displacement boundary condition (B.C). The top and bottom B.C are applied in phase to excite symmetric mode $S0$ and out of phase to excite anti-symmetric mode $A0$. The implicit solver was configured to run simulations with fixed 0.1 μs time increments. The displacements at the receiver end were saved for every time increment in order to create snapshots of the ultrasonic wave field. With this model being created, the modal analysis was performed with the help of PYTHON by sweeping through selected parameters.

4.3.1.1 Results and Discussion

Displacements acquired on the receiver end on all 70 simulations are processed and features are extracted using MATLAB. The aim of this analysis is to identify which combination of mode and frequency are sensitive to crack initiation and propagation. Figure 4.3 shows the input and recorded received signal at 75 kHz under $S0$ mode on a pristine lap-joint. 70 such input and received signals are obtained form ABAQUS. To identify sensitivity features, Guided wave signals acquired at different combinations were processed to estimate their energy spectral density (ESD), E according to Equation 4.2.

$$E = \int_{f_1}^{f_2} |\hat{s}(f)|^2 df, \tag{4.2}$$

where $\hat{s}(f) = \int_{-\infty}^{\infty} e^{-i(2\pi f)t} s(t)dt$ is the Fourier transform of the acquired and cropped signal $s(t)$, and f_1 and f_2 are the lower and upper frequencies which are $+/-$ 15 kHz from the corresponding excitation central frequency.

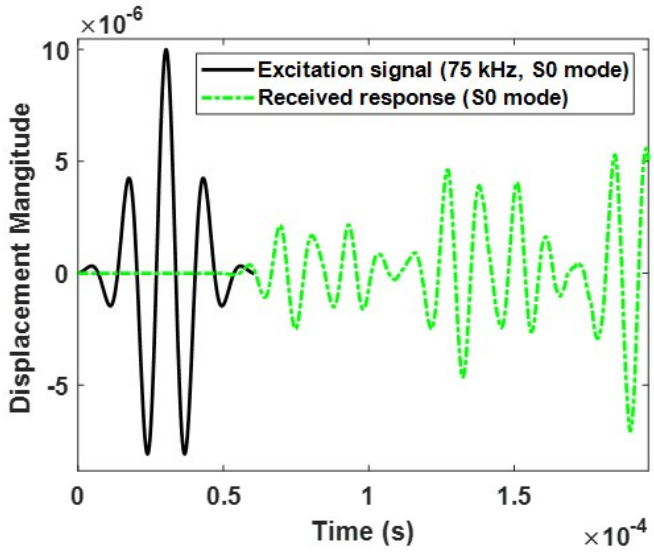

Figure 4.3: Excitation and received GW signal at 75 kHz, S0 mode configuration on a pristine lap-joint

Figure 4.4 and 4.5 shows the sensitivity of selected mode and frequency combination towards crack initiation and propagation respectively. Sensitivity towards crack initiation is obtained by taking the energy difference between pristine and initial cracked ESD. Similarly, sensitivity towards crack propagation is obtained by taking the energy difference between first and final cracked (8mm) ESD. Analyzing $A0$ from Figure 4.5 clearly indicates that it is less sensitive towards crack propagation compared to $S0$ mode under any frequency combination. However, from Figure 4.4 it can be seen that combination of $A0$ mode at 45 kHz is highly sensitive to crack initiation in comparison to symmetric mode. Thus tracking $A0$ and $S0$ mode at 45 kHz will help to identify the damage state transition.

Figure 4.6 shows the received symmetric $S0$ and anti-symmetric $A0$ signals at 45 kHz combination for pristine and 2 mm cracked joint. $A0$ mode signals shows drastic variation between cracked and pristine joint. This reconfirms the selected frequency-mode combination is sensitive towards crack initiation. Like-wise Figure 4.7 shows the received symmetric $S0$ and anti-symmetric $A0$

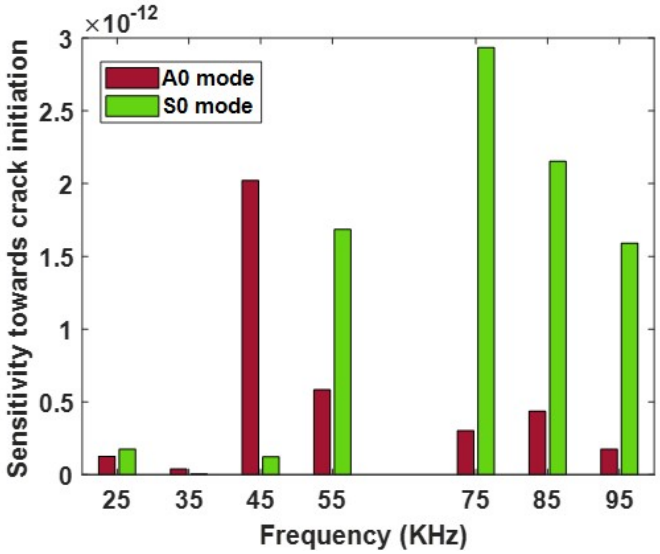

Figure 4.4: Sensitivity analysis towards crack initiation

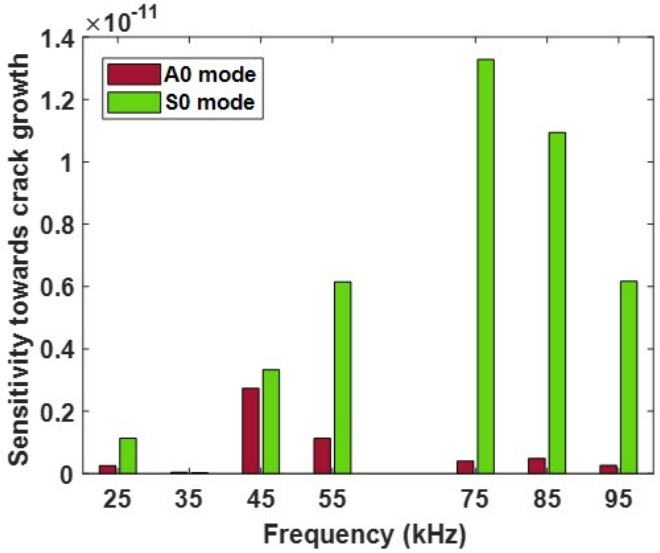

Figure 4.5: Sensitivity analysis towards crack propagation

signals at 75 kHz combination for 2 and 8 mm cracked joint. In this case $S0$ mode signals shows drastic variation during crack propagation. This confirms the selected $S0$, 75 kHz combination is sensitive towards crack propagation.

Simulation results are analyzed and anti-symmetric ($A0$) mode at 45 kHz is found to be the most sensitive mode-frequency combination to detect fatigue crack initiation. Further, symmetric $S0$ mode at 75 kHz is proved to be more sensitive towards crack propagation. Experimental validation

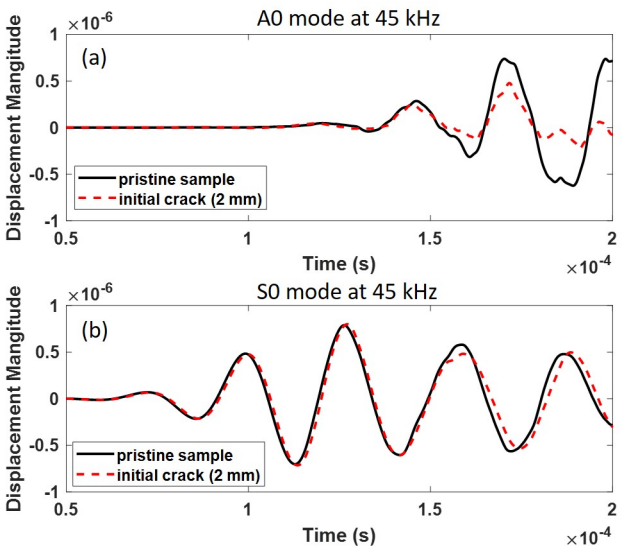

Figure 4.6: Received symmetric $S0$ and anti-symmetric $A0$ signals at 45 kHz combination for pristine and 2 mm cracked joint

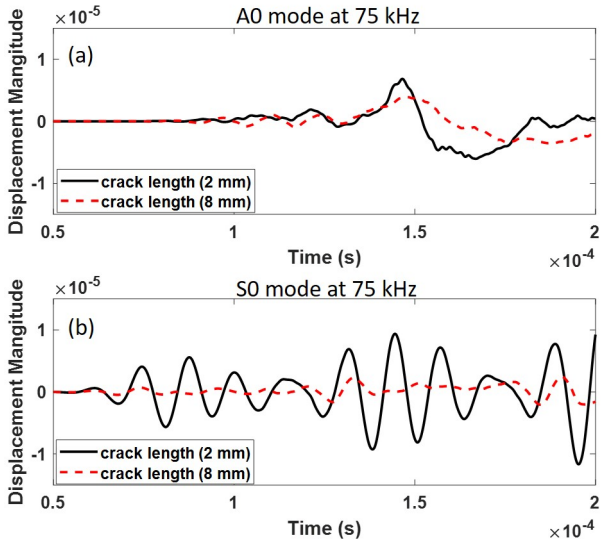

Figure 4.7: Received symmetric $S0$ and anti-symmetric $A0$ signals at 75 kHz combination for 2 and 8 mm cracked joint

are planned in the future, where selected frequency combination of both $A0$ and $S0$ modes are continuously tracked in real-time to identify damage state transition N^*. Further, identified N^* will be used in prognosis algorithm for accurate remaining useful life prediction.

4.3.2 Experimental modal analysis

In this section, experimental setup for both mechanical testing and guided wave system along with optical camera are shown. Both fatigue and monotonic loading of fabricated samples where conducted and their guided wave and mechanical test results are illustrated in detail.

4.3.2.1 Experimental setup

The experimental setup consist of two NDE technique for damage identification such as guided wave and optical camera. Damage identified form MTS data are accurate and so treated as reference damage index. Figure 4.8 shows the overall flow of control and components in the experimental setup. The control unit is in the center of the experimental setup where, it is connected to all the components of the setup and controlled using an MATLAB algorithm.

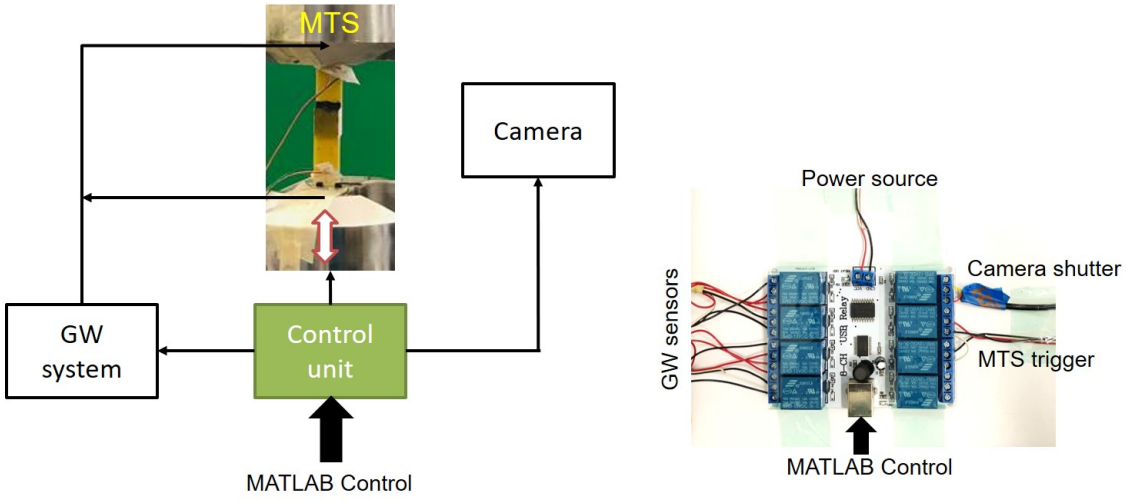

Figure 4.8: Experimental setup used for Fatigue monitoring along with control unit

Figure 4.8 shows the physical control unit which is a 8 channel relay system controlled with the help of MATLAB algorithm. Five relays are controlled to perform a fully automated model analysis. Four relays on the left are used to switch the polarity of each transducer pair to excite either symmetric *S* or anti-symmetric *A* mode. Two relays on the right is used to control the MTS system. One relay on the top right corner controls the camera shutter. During modal analysis, the control

unit automatically pauses fatigue loading at specified fatigue intervals and trigger GW system to obtain crack growth data for different frequency-mode combination. Once data acquisition is completed, the MTS is triggered to resumes fatigue cycle. This process repeats until the sample fails without any manual intervention.

4.3.2.2 Mechanical Testing

The setup used for fatigue testing and experimental data collection is shown in Figure 4.9. At first, similar lap-joints were subjected to monotonic displacement testing. These tests were conducted without sensors to determine the maximum tensile strength. Monotonic tests results conducted at a test rate of 2mm/min is shown in Figure 4.10. The fatigue testing was done with the surface bonded PZT sensors as described in chapter 3.

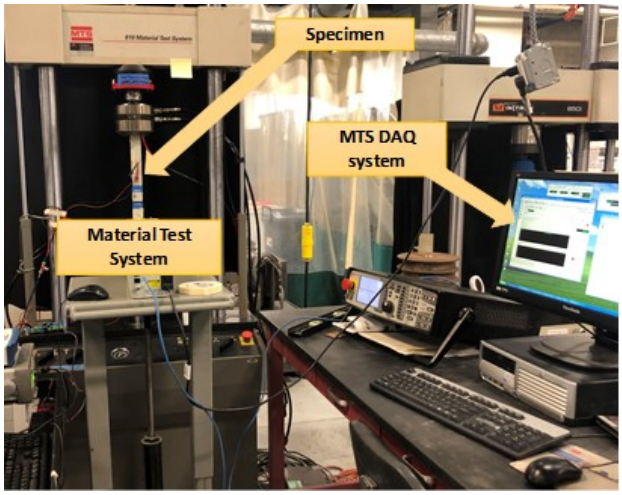

Figure 4.9: Mechanical testing system with Data collection

Under displacement testing the lap joints failed at approximately *1.72 kN* (refer figure 4.10) and hence the fatigue tests were conducted at 70% of the maximum load cycle with cyclic frequency of 4 Hz.

For fatigue testing the maximum load (P_{max}) was set to 70% of $1.72kN$ and which equals $1.2kN$. The load ratio P_{min}/P_{max} was considered as 0.1 [5] and thus P_{min} becomes $0.12kN$. Therefore in case of force controlled testing, applied force varied from P_{min} to P_{max} with initial target set point

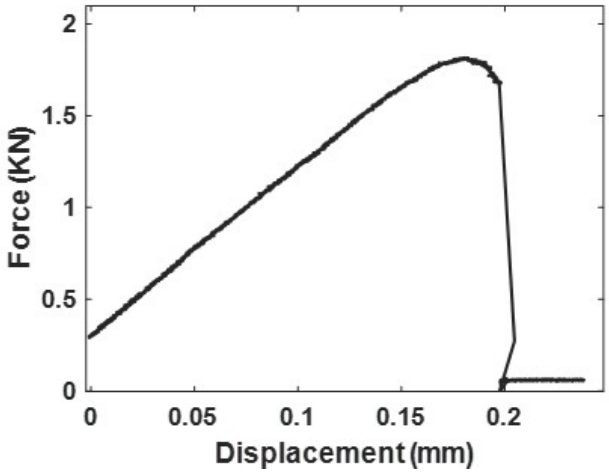

Figure 4.10: Force and displacement from monotonic testing

at 540N. Force, displacement and guided wave signals were collected at certain fatigue interval. True damage area A_{Damage} was then estimated using equation 4.1 with force and displacement information from MTS. Effective area is the undamaged area of adhesive available at any fatigue cycle for stress transfer and was calculated according to equation 4.3, $A_{pristine}$ being the area of pristine sample.

$$A_{eff} = A_{pristine} - A_{Damage} \tag{4.3}$$

Figure 4.11 shows the increase in damage area of adhesive with increasing load cycles. It can be inferred that the effective area reduces rapidly during the first 400 cycles. After that, the change in area is minimal until total failure after 3900 cycles where the lap-joint completely broke apart indicative of failure.

4.3.2.3 Optical and Guided Wave Technique

In this section two NDE technique used for fatigue damage estimation is analyzed. First, the optical camera is used to directly capture the crack formation and growth in the lapjoint during fatigue intervals. Figure 4.12 shows the camera setup to capture the lap-joint's side view. Some samples prepared using induction bonding technique will have excess adhesive outside the bond-line. Any

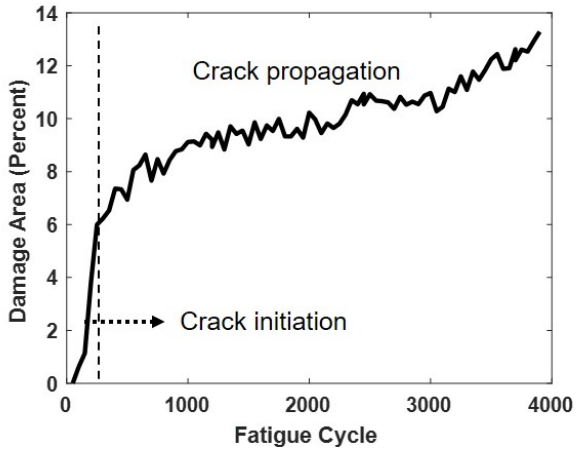

Figure 4.11: Bond line damage area vs fatigue cycle

excess adhesive are removed and the flat surface is coated with a thin uniform layer of water based white paint. During fatigue loading, the control unit stops the MTS loading at predefined fatigue intervals. Once the fatigue loading is stopped, the MTS system applies a constant mean load (540N). Then the control unit activate the camera shutter to obtain the crack images as shown in figure 4.12.

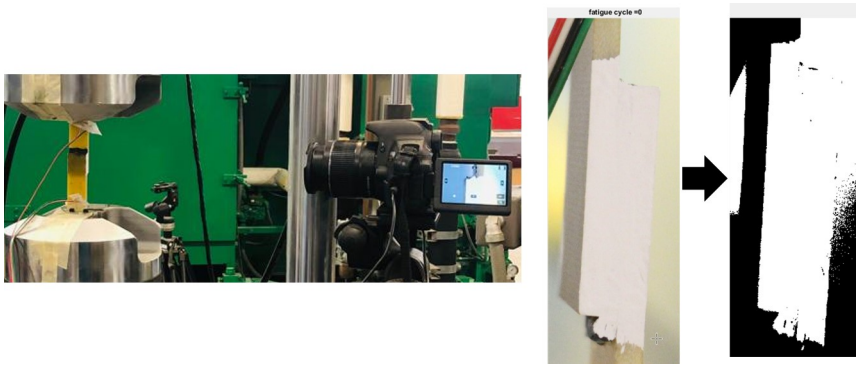

Figure 4.12: Guided wave setup for modal analysis during fatigue

Images taken at various fatigue intervals are processed in MATLAB to identify the crack clearly. Figure 4.13 shows the processed image of bond-line at crack initiation (400 cycle) and crack propagated until a complete failure (3900 cycle). The change in crack length can be clearly seen in the processed images. Figure 4.13 also shows the measured crack length at different fatigue

cycles. It can be seen that the initial crack formation is about 1.4mm and it has a faster phase of formation. After the crack initiation the propagation phase is much slower which is in accordance with the MTS and literature survey. During crack propagation, the crack lenght grew about 3.2mm and a complete failure occurred. It is important to note this behavior is strictly for the given loading condition and geometry of the lap-joint.

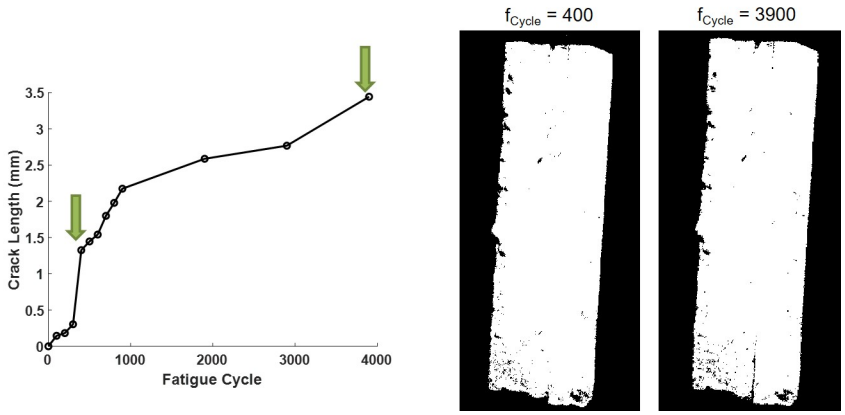

Figure 4.13: Guided wave setup for modal analysis during fatigue

The block diagram of the guided wave system is shown in figure 4.14. It consisted of 1) PZT wafers deployed on the lap-joint, 2) arbitrary waveform generator 33220A from Keysight Technologies, 3) control unit, and 4) data acquisition (DAQ) device USB-6255 from National Instruments. PZT wafers were bonded to the Garolite adherends using instant Loctite epoxy. PZT transmitters were electrically connected to the output of the waveform generator, via control unit where the excitation mode is controlled. Excitation was done using a Morlet wavelet function with adjustable center frequency, bandwidth and amplitude. Guided waves transmitted through the adhesive bond-line were sensed using PZT receivers, which were connected to the control unit for mode control. Signals from the control unit were acquired by the DAQ with a sample rate of 1.25 MS/s at 10 averaging. Data was then transferred to a PC with MatLab for real-time processing. Guided wave measurement system was only activated between the fatigue intervals to avoid interference of changing load during fatigue cycles.

To perform modal and frequency analysis, the MATLAB algorithm instructs the function

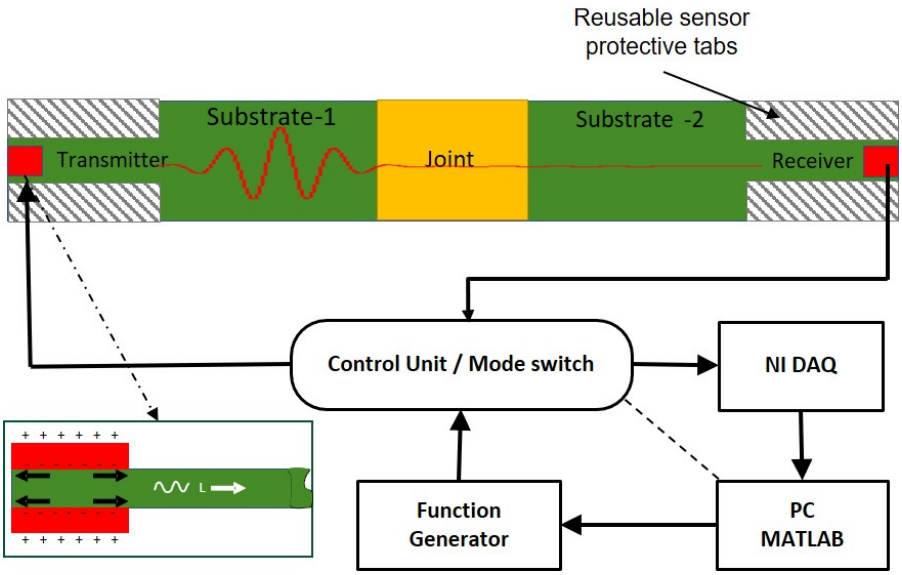

Figure 4.14: Guided wave setup for modal analysis during fatigue

generator to change frequencies between $35kHz$ to $85kHz$ with $10kHz$ stepping. Also symmetric and anti-symmetric modes are tested for all the above mentioned frequencies. Thus we have 12 guided wave waveform collected at a single fatigue interval. For a sample with about 4000 cycles, and 13 fatigue intervals consist of 156 waveform. Thus an effective processing technique is need to process such large volume of waveform. Guided wave signals acquired at different mode, frequency and fatigue cycle combinations were processed in MatLab in order to estimate their energy spectral density (ESD), E_S:

$$E_S = \int_{f_1}^{f_2} |\hat{s}(f)|^2 df, \tag{4.4}$$

where $\hat{s}(f) = \int_{-\infty}^{\infty} e^{-i(2\pi f)t} s(t) dt$ is the Fourier transform of the acquired and cropped signal $s(t)$, and f_1 and f_2 are the lower and upper frequencies selected for the analysis, respectively. Then the guided wave transmission coefficient α was evaluated for each signal as:

$$\alpha^{(n)} = \frac{E_S^{(n)}}{E_S^{(0)}}, \tag{4.5}$$

where $E_S^{(n)}$ is the ESD of the n-th guided wave signal acquired at n-th fatigue cycle, and $E_S^{(0)}$ is the ESD of the baseline signal acquired at zero fatigue cycle. Guided waves are launched for inspection

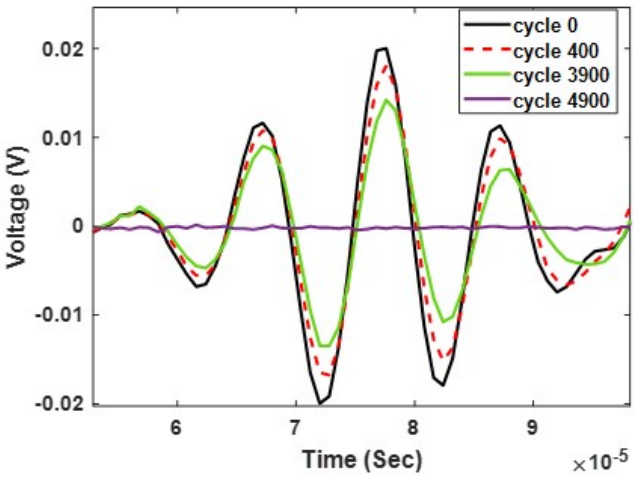

Figure 4.15: Guided wave signals for $85kHz$ and Symmetric mode combination at 0, 400, 3900 and 4900 fatigue cycle

only after the MTS system is paused. In the guided wave system, transmitter was excited with a Gaussian pulse signal of selected frequency at 0.5 bandwidth as discussed in chapter 3. The guided waves generated at first substrate, travels through the lap-joint and then to the second substrate. Receiving transducer bonded on the second substrate picks up the transmitted guided wave. Initially generated guided waves undergo double mode conversion at the grips, beginning and at the end of lap-joint. It would be complex to isolate modes at the receiver end. Thus only the energy transfer between the adherents is analyzed in this study. Figure 4.15 shows the received signal at $85kHz$ over different crack stages such as 1) $0cycle$ before the fatigue cycle starts 2) $400cycle$ right after crack initiation 3) $3900cycle$ before the sample completely fails 4) $4900cycles$ where the sample completely failed. Other studies show a similar trend of GW response [37].

Figure 4.16 and 4.17 shows the energy transferred at 6 different frequencies and 13 different fatigue interval for symmetric and anti-symmetric modes respectively. All the frequency for symmetric mode combination is sensitive towards fatigue damage, see figure 4.16 . However, comparing different combinations, Energy change of symmetric mode at $85kHz$ clearly is qualitatively similar to effective area change as shown in figure 4.11 and figure 4.13. Also, $65kHz$ combination is very sensitive towards stage transition. Other studies also show a similar trend of GW response

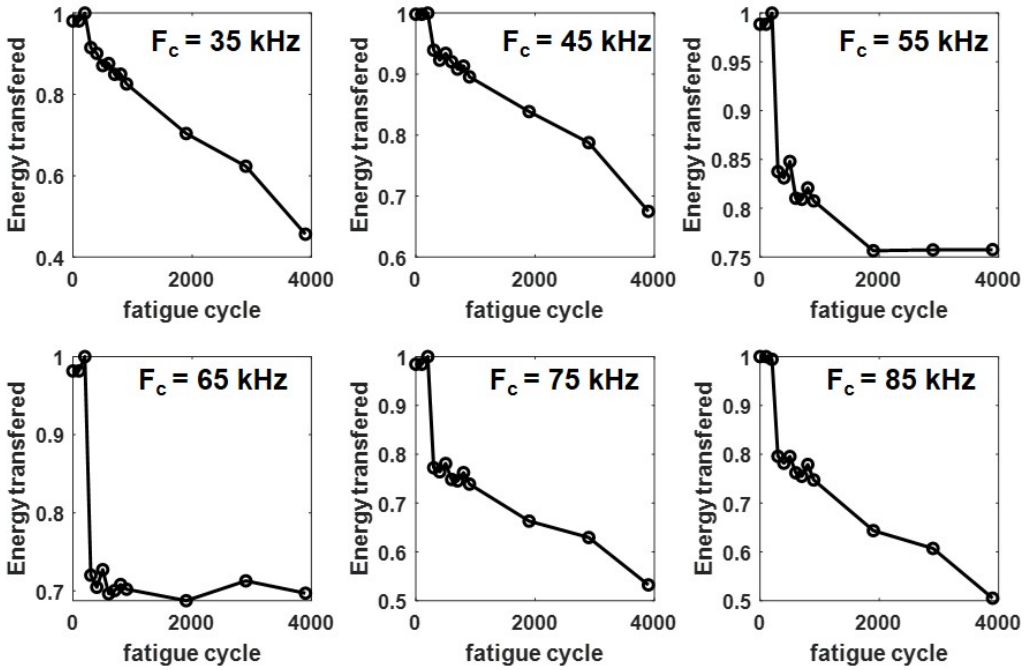

Figure 4.16: Guided wave energy received vs fatigue cycle for symmetric mode

towards fatigue damage [37]. Under anti-symmetric mode $A0$, $35-55kHz$ show similar trend as of symmetric mode. other frequency combinations are not consistent. Thus from the experimental modal analysis, symmetric mode at $85kHz$ is selected as the most sensitive combination for fatigue damage. It is important to note that the identified mode-frequency combination is geometry and load specific. Thus, a new modal analysis should be conducted for a sample with different geometry and loading condition.

4.4 Diagnosis of fatigue damage

From section4.3 symmetric mode, $85kHz$ is selected as the optimal mode-frequency combination for fatigue damage identification from experimental modal analysis. Experimental and numerical modal analysis do not share the same behavior owing to the simplification and assumptions considered in the numerical analysis. Thus, outcome of experimental analysis is used in diagnosis and prognosis of fatigue damage. In this section, only data collected at selected mode-frequency combination is processed to perform fatigue diagnosis.

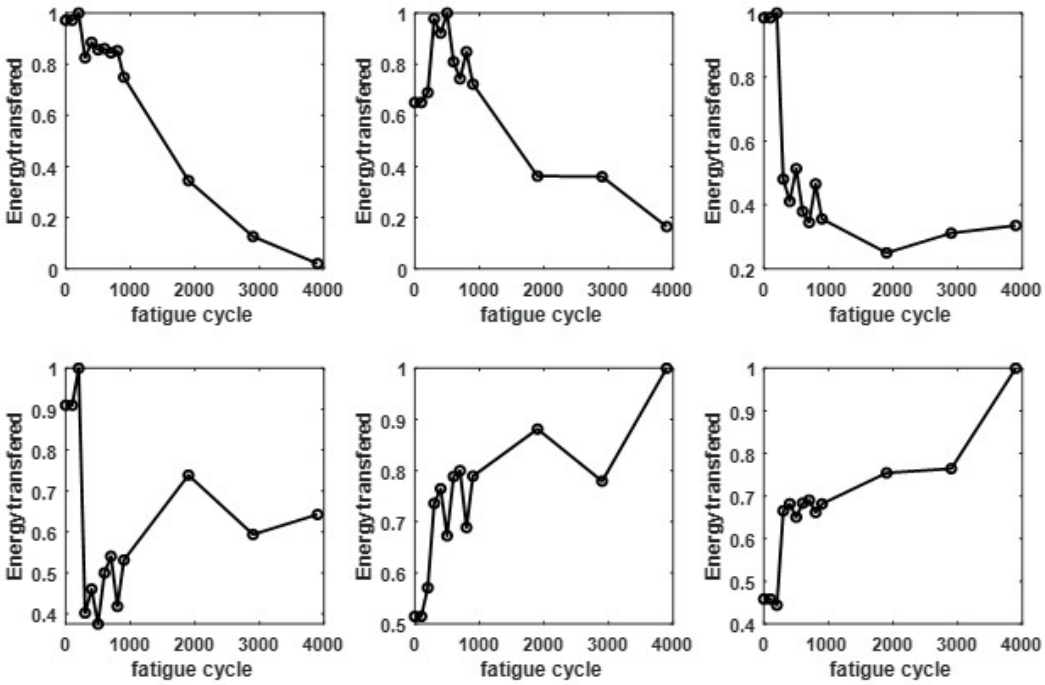

Figure 4.17: Guided wave energy received vs fatigue cycle for anti-symmetric mode

Figure 4.15 shows the time series data of received signal for symmetric mode at $85kHz$ over different crack stages such as 1) $0cycle$ before the fatigue cycle starts 2) $400cycle$ right after crack initiation 3) $3900cycle$ before the sample completely fails 4) $4900cycles$ where the sample completely failed. Clearly the amplitude of the signal shows a significant change as the damage area grow. However, there is no significant phase or frequency shift noticed.

Transmission coefficient E_s is calculated according to equation 4.5. For a final validation fatigue damage estimated using optical and MTS system are compared to the GW system. The normalized transmission coefficient E_s obtained from GW system is directly proportional to the effective area $A_(eff)$. Thus normalized damage index shall be easily obtained by $1 - E_s$ as shown in figure 4.18. The estimated fatigue damage form guided wave technique is highly correlated with MTS and Optical camera system. As discussed in section 4.2 crack formation and propagating is random among samples. Thus, one more sample is validated with MTS results only see figure 4.19. Considering figure 4.18 and 4.19 it can be clearly seen that the intensity and growth rate of crack is

different for different stages and samples. Overall, MTS and GW system have greater correlation, thus GW system have successfully tracked the fatigue damage In both the samples. This illustrate the potential of developed in-situ ultrasonic technique for real-time fatigue damage diagnosis.

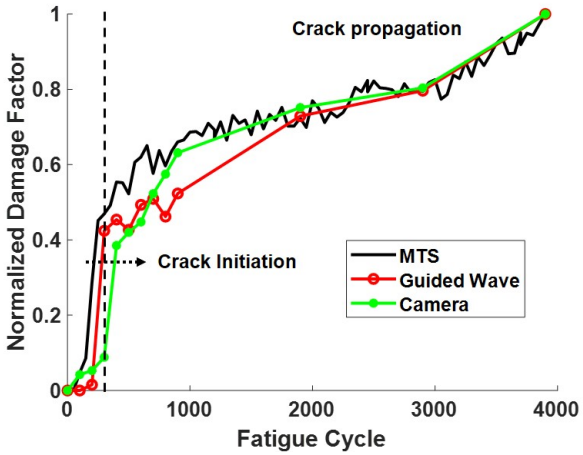

Figure 4.18: Comparison of fatigue damage estimated from MTS system, optical camera, and guided wave system.

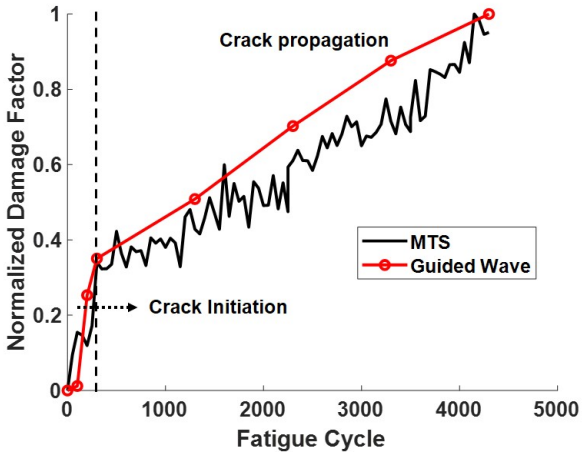

Figure 4.19: Comparison of fatigue damage estimated from MTS, and guided wave system.

4.5 Prognosis of Fatigue Damage

In this study, particle filtering framework was implemented to predict damage area in the lap-joint using guided wave measurements from first few load cycles. Particle filtering is a powerful prognostic tool since it combines benefits of both data-driven and model-based prediction approaches. To begin with, a modified damage growth model based on Paris law was defined to generate the degradation trend of fatigue-induced damage growth in the lap-joint specimens. Paris model was first studied for prediction of crack growth rate in a metal plate under Mode I loading condition relating rate of increase of crack length per cycle $\frac{da}{dN}$ and the range of the stress intensity factor ΔK , according to equation 4.6 [54] . Since then, Paris model has been widely implemented in several crack growth studies in metals [51, 13] as well as in composites [55, 20].

$$\frac{da}{dN} = C\,(\Delta K)^m \tag{4.6}$$

where a is the crack length, N is the total number of load cycles and m,C are the Paris law parameters. ΔK can be further interpreted as:

$$\Delta K = Y\sqrt{\pi a} \tag{4.7}$$

where, Y is a dimensionless constant depending on the crack shape and geometry of the specimen for a given stress range in the fatigue crack growth models.

As shown in Fig. 4.11, the damage area growth curve obtained from fatigue experiments in lap-joints can be observed to increase at different rates before and after the knee-point of 400 cycles (for this case study). Hence, a Paris-Paris model based on Piecewise-deterministic Markov processes (PDMPS) was used in this study where Paris law is described by two sets of parameters (m_1, C_1, m_2, C_2) before and after a transition time N^*, denoted by equation 4.8. This model have been adopted from previous damage growth studies in composite structures by Banerjee et al. [6, 7].

$$\frac{da}{dN} = \begin{cases} C_1\left(Y\sqrt{\pi s}\right)^{m_1}, & \text{if } N \leq N^* \\ C_2\left(Y\sqrt{\pi s}\right)^{m_2}, & \text{if } N \geq N^* \end{cases} \tag{4.8}$$

Next, T_c values from the periodic guided wave measurements on the lap-joints, denoted by z_k, were incorporated for updation of model parameters. z_k is assumed to linearly correlate with the true damage area a_k of the lap-joint at load cycle N_k along with additive noise ω_k.

$$z_k = H(a_k) + \omega_k \tag{4.9}$$

$$\omega_k \sim \mathcal{N}(0, \sigma^2) \tag{4.10}$$

4.5.1 Procedure

Details of the proposed algorithm for estimation of Paris-Paris model parameters are summarized in the following steps.

1. **Initialization**: At $k = 1$ step, the initial (prior) distribution of n samples of all parameters Θ_k is defined.

$$\begin{aligned} s_0 &\sim \mathcal{N}(0.01,\ (0.001)^2) \\ m_{10} \sim \mathcal{N}(0.8,\ (0.01)^{0.01}), &\log C_{10} \sim \mathcal{N}(-5,\ (0.01)^2) \\ m_{20} \sim \mathcal{N}(0.5,\ (0.01)^2), &\log C_{20} \sim \mathcal{N}(-10,\ (0.01)^2) \\ N*_0 &\sim \mathcal{N}(40,\ (5)^2) \\ \omega &\sim \mathcal{N}(0.05,\ (0.01)) \end{aligned} \tag{4.11}$$

2. **Prediction**: Posterior distributions of the model parameters evaluated at the previous $(k-1)^{th}$ step are used as prior distributions at the current step (k).

   Damage area at the current time step is then computed from the parameters estimated at the previous step by rewriting equation 4.8 in its state-transition form as:

$$a_k = \begin{cases} C_1^k \left(Y\sqrt{\pi a_{k-1}}\right)^{m_1^k} \Delta N + a_{k-1}, & \text{if } N_k \leq N^* \\ C_2^k \left(Y\sqrt{\pi a_{k-1}}\right)^{m_2^k} \Delta N + a_{k-1}, & \text{if } N_k \geq N^* \end{cases} \tag{4.12}$$

3. **Updating**: The distribution of i^{th} particle is updated based on its likelihood given the T_c measurement data (z_k), as denoted in equation 4.13. It is important to note that different Paris law parameters $\{m_1, C_1\}$ and $\{m_2, C_2\}$are selected before and after the loading cycle N_k crosses the 'jump' cycle N^*.

$$L(z_k|a_k^i) = \frac{1}{z_k\sqrt{2\pi}\sigma_k^i} exp\left[-\frac{1}{2}\left(\frac{z_k - a_k^i}{\sigma_k^i}\right)^2\right] \tag{4.13}$$

4. **Resampling**: Finally, resampling is achieved through inverse CDF method such that particles with higher likelihood of representing the true measurement data are duplicated while the others are discarded [80]. The process is repeated n times in order to obtain n resampled particles at the k^{th} iteration. The PDF constituted from these resampled particles thus forms the posterior distribution of the current iteration $p(\boldsymbol{\theta_k}|z_{1:k})$ and the prior distribution of the next iteration. Adding randomness to the resampling process avoids degeneracy of weights.

5. **Remaining-Useful-Life (RUL) computation**: In this study, it is assumed that the end-of-life (EOL) of the lap-joint occurs at $L_{EOL} = 3900$cycles when the joint is completely broken apart. Hence, the paris-paris model parameters $\boldsymbol{\theta_k}$ are updated upto $k = L$ iterations, where L is the total number of observed measurements. After L iterations, future damage area is predicted using equations 4.12. RUL after L iterations is hence computed as $RUL_L = (L_{EOL} - L)$ cycles. The RUL PDF is generated by computing the RUL of all the particles. The mean and median values are computed at each load cycle.

4.5.2 Results and Discussion

Guided wave data collected during experiments are used for prognosis using the procedure shown in section 4.5.1. Initial distribution of noise (eq. 4.12) was characterized based on experimental evidence of GW measurements on lap-joint specimens shown in figure 4.18. The other set of guided wave measurements are used in rest of the prognosis procedure. Prediction results with different number of measurements are presented in Fig.4.20. It should be noted that as number of

measurements increases, the predicted damage area converges to the true values calculated from MTS measurements according to equation 4.3. Further, the 95 percentile uncertainty bounds also decreases thereby increasing confidence associated with the prediction results.

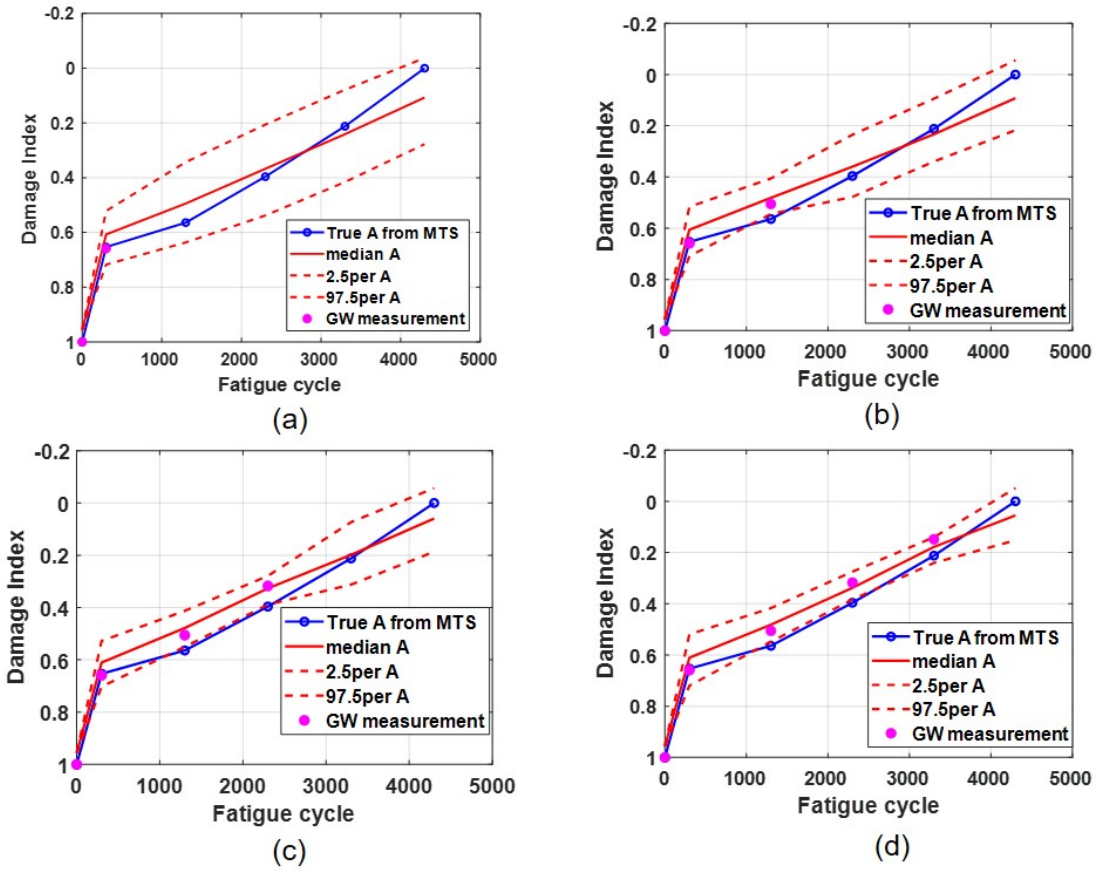

Figure 4.20: Prediction of damage growth curve based available guided wave measurement in Paris-Paris model until following fatigue cycle (a) Fc=400, (b) Fc=1300 (c) Fc=2300 (d) Fc=3300.

The estimated RUL values at all fatigue stages are illustrated in Fig. 4.21. For most cases with the given loading condition, samples fails around 5000 cycles. In the beginning the estimated RUL is lower then the actual value as initial assumption and random variable distribution is taken from a different sample. However, once the guided wave measurements started to flow into the prognosis algorithm the predictions become much accurate and the estimated RUL converged to the true values.

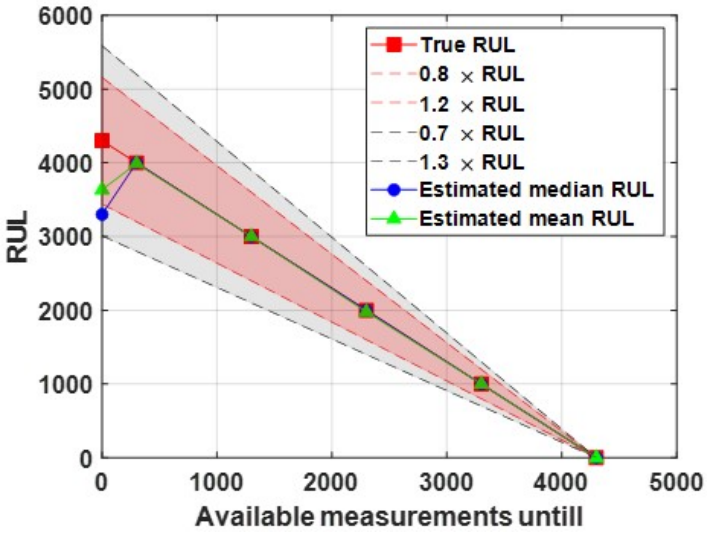

Figure 4.21: RUL prediction for varying number of available guided wave measurements.

4.6 Summary and Conclusion

This chapter presents a guided wave technique to monitor and predict damage area growth in adhesive bonded SLJ. Mechanical test results reveal that the damage area growth is rapid in the first 400 cycles followed by slow growth rate until complete failure. A similar trend was noticed in the transmission coefficients of the GW signals and optical images as the damage area grew in size, hence denoting the sensitivity of the NDE technique for damage diagnosis in composite SLJs. Two samples where successfully validated for diagnosis of fatigue damage with guided wave measurements only. Further, a data-driven prognosis technique is introduced and guided wave data are used for prediction of damage area in upcoming cycles and Remaining useful life. Final validation of prognosis results show a reliable prediction of damage area and RUL.

CHAPTER 5

GUIDED WAVE CONTROLLED HEALING OF DAMAGES IN BOND-LINE

5.1 Introduction

Repair or removal of damaged bond-line is expensive and it can even cause damage to adjoining structures. Using thermoplastic adhesive with dispersed ferrous nano-particles can enable localized healing and easy dismantling for re-usability of components. One of the commonly used bond-line healing technique is micro-encapsulation approach. Here the healing agent and catalyst are dispersed in epoxy matrix, Once a damage occurs the suspended capsules around the damage area release the healing agent which react with dispersed catalyst to polymerize and activate the healing process [79, 35]. Li et al [42], proposed a two step self-healing technique. In this method, first the initial cracks are closed using a steel frame and later placed in oven to introduce heat that activate healing of thermoplastic particles. Aubert et al [4], introduced cross-linked polymers that are capable of healing cracks by formation of thermal activated covalent bond. This reaction is also known as Diels-Adler reaction.

For bonding non-metallic substrates, Thermoplastics embedded with conductive nano-particles are great choice. Verna and ciardiello [74, 18], illustrated the assembling and dismantling of joints using Electro-Magnetic (EM) heating technique. EM offers various advantages over above mentioned healing techniques. EM healing allows targeted healing, reduced energy usage, rapid processing. Vattathurvalappil et al [72], demonstrated the ability of EM healing on impact damaged bondline. Alternate magnetic field applied to dispersed ferromagnetic nanoparticles (FMNP) introduces hysteresis losses in the FMNPs, which results in intensive heat dissipation and melting from within the adhesive. However, it is essential to accurately measure the temperature of the adhesive, since overheating may cause chemical degradation while repair. In this research work an ultrasonic guided wave technique for online monitoring of the adhesive state while repair and feedback control of the electromagnetic bonding process.

Guided wave monitoring technique described in chapter 3 is used here for controlled healing. Single lap-shear joints subjected to fatigue damage as described in chapter 4 are healed and mechanically tested to analyze restoration of the original bond strength. Further, this technique is also numerically investigated to heal a localized bond area in a long bond-line.

5.2 Controlled Induction Healing of Single Lap-joint

In this section, a new single lap-joint is processed using induction heating method and the processed bond is subjected to fatigue loads. Crack formation due to fatigue loads are healed using guided wave controlled induction heating. Figure 5.1 shows how a controlled new bondline is processed. It is important to note that while preparing a new bond line, initially there is no transfer of stress wave across the bond line as the adhesive is not melted yet and are not chemically bonded to the substrate. Thus, a small amount to uncontrolled intermittent heating is applied as shown in figure 5.1. It can be seen that there is a $20s$ of intermittent heating to achieve initial melting of adhesive strips. Initial heat does not create any adhesive degradation. The process monitoring system developed in section 3.2.2 is modified to wait for $100s$ and monitor the energy transmission coefficient T_c across the bond-line. If the T_c value did not reach 90% of reference T_c value, then the heating cycle is repeated. The reference T_c is measured using an oven bonded joint. Figure 3.8 shows the lap-joint took three heating cycles to achieve almost 100% of reference T_c value.

The newly processed single lap-joint is subjected to about 2000 fatigue cycles. An initial crack formation is observed and also the guided wave fatigue monitoring technique developed in chapter 4 shows a 15% loss in guided wave energy transfer. The tracked energy transfer during fatigue have a different boundary conditions and mode-frequency combination as that of process monitoring. During process and heal monitoring a symmetric mode at 35 kHz is used and during fatigue monitoring symmetric mode at 85 kHz is used. Energy transfer at symmetric 35 kHz shows a 20% loss as shown in figure 5.1. Now the lap-joint is heated using controlled induction system as developed in chapter 3. Once the adhesive is completely melted, the system detects the phase change and stop the induction system automatically. Figure 5.1 (b) shows the guided wave energy

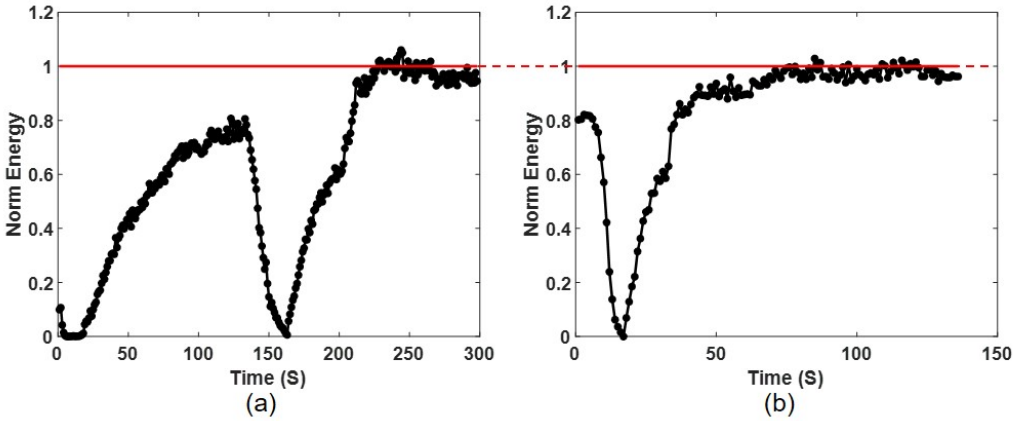

Figure 5.1: Controlled processing and healing of bondline: (a) processing a new bond; (b) controlled healing of fatigue damaged bond.

transfer is completely restored.

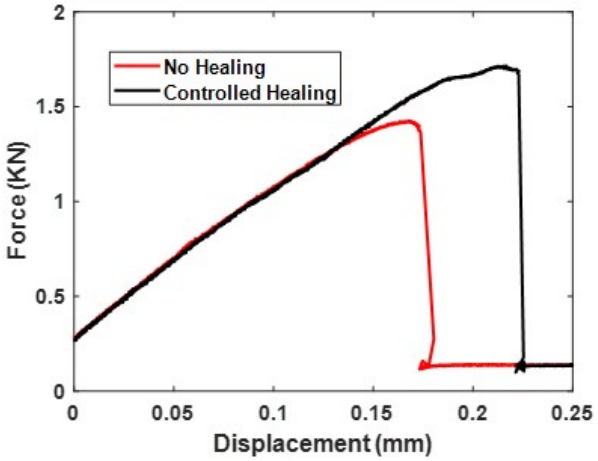

Figure 5.2: Representative load-displacement curve of lap-joint after fatigue damage and healing

Samples prepared after fatigue and healing are tested in Mechanical Testing System for ultimate shear strength. Monotonic lap-shear tests are conducted in the MTS machine at the rate of $0.1mm/min$ as shown in figure 5.2. It can seen that the lap-joint processed by GW control shows higher ultimate strength and also higher displacement to failure. This clearly indicate the effectiveness of controlled healing. Figure 5.3 shows Mean and variance of ultimate strength comparison between newly processed lap-joints and joints subjected to fatigue and healing. From

figure 5.3 it can be seen that after 2000 fatigue cycles the joint lost about 20% of load carrying capacity and once the joint is healed, it has recovered almost 98% of its original strength. Thus the developed controlled healing technique is very efficient in restoring the original bond strength.

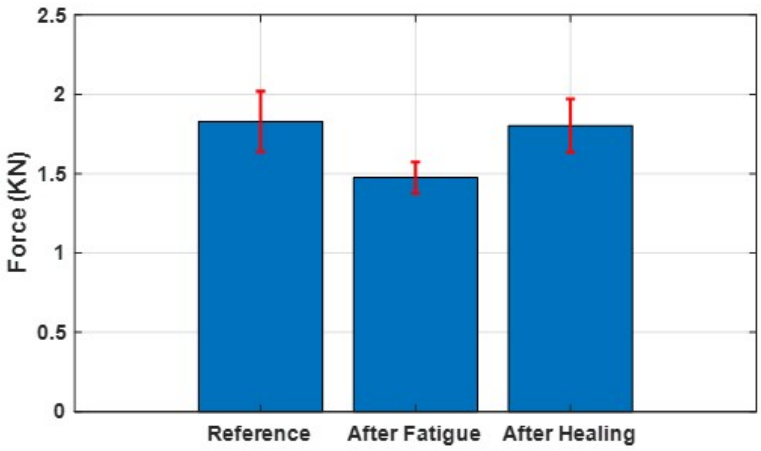

Figure 5.3: Peak load carrying capacity of lap-joint at different life stages

5.3 Healing Technique for Long Bondline

Generally, damage in long bondline are not throughout the bondline, thus it would be much easier to heal only the damage section. The only challenge in localized healing of a bondline compared to healing a single lap-joint is transfer of energy through non-melted adhesive zones. Thus this section will focus on numerically understanding the behavior of guided waves while healing a small section of a long bondline 5.4. Two finite element models developed to understand dispersion properties and propagation of ultrasonic guided waves in the adhesively bonded lap-joint. The first model was an eigenfrequency study that helped determine possible GW modes in the adherends and the bond-line region of the joint. Results of the study were used to identify an optimal excitation frequency and select the mode shape that would be most sensitive to changes in the modulus of adhesive. The second FE model was a time-dependent study of wave propagation from one adherend to another thorough the bond-line. Guided wave signals were simulated at different adhesive temperatures in order to link the features in the signals such as energy, peak amplitude or time-of-flight to adhesive

state. Temperature-dependent viscoelastic properties of the adhesive were taken from the DMA, and uniform temperature distribution in the adhesive was assumed for simplicity.

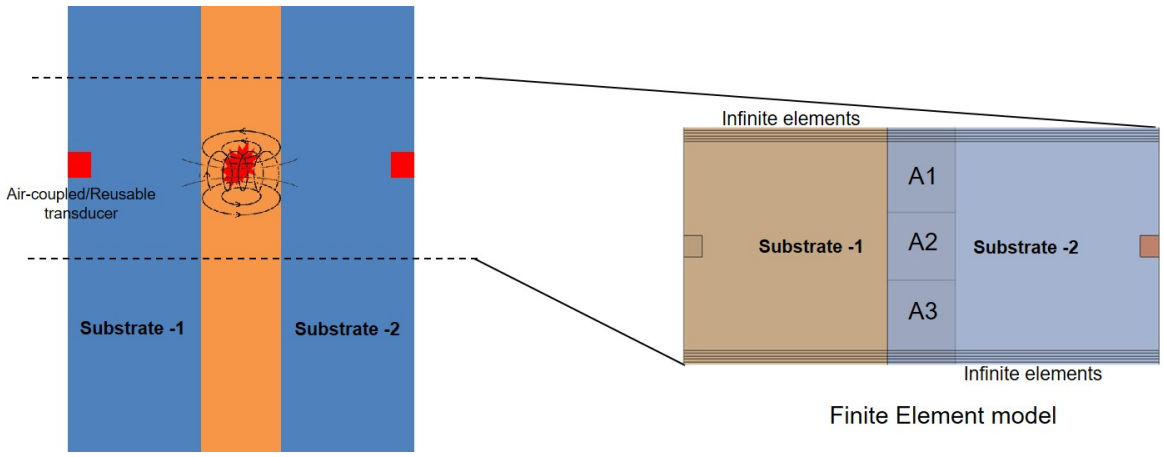

Figure 5.4: Selective heating of long bondline along with representative Finite Element Model.

5.3.1 Dispersion Analysis

Guided waves are elastic waves that can propagate in plate-like structures, bars, rods, pipes, rails and other waveguides of various cross-sections and periodicity. Compared to ultrasonic bulk waves, guided waves are characterized by complex displacement fields or modes. Only certain modes can be supported by the host structure, however there can be multiple at the same excitation frequency. Guided waves are also dispersive, meaning that the phase and group velocities of each mode are functions of excitation frequency. Hence, determining dispersion relations is key in current application, since the goal is to identify modes with large displacements in the adhesive bond-line of the lap-joint.

Dispersion relations for plates can be computed analytically (e.g. using Rayleigh-Lamb equation for isotropic plates [60, 49], Transfer Matrix method or Global Matrix method for classical laminates[53]) based on the assumption that plates have infinite length and width. More sophisticated techniques such as Semi-Analytical Finite Element (SAFE) method [60] were developed for computation of dispersion relations of waveguides with arbitrary cross-sections. In this work, we adopted Floquet-Bloch (F-B) technique ([28]) to identify dispersion curves of the adherends

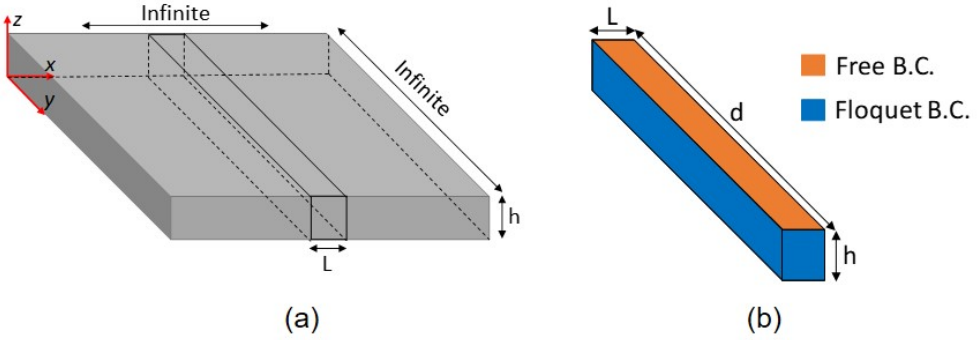

Figure 5.5: Floquet-Bloch theory for computation of dispersion relations of a plate-like waveguide: (a) unit cell; (b) boundary conditions.

and bond-line region of the lap-joint. The F-B technique doesn't require development of complex numerical scripts and can be easily implemented using commercial FEM software.

The concept of the F-B is to represent a continuous plate-like waveguide with a unit cell and apply periodic displacement boundary conditions on the faces perpendicular to the direction of wave propagation (see fig.5.5).

The F-B method for finding dispersion relations was implemented in Comsol Multiphysics 5.4. Structural mechanics module was used to conduct an eigenfrequency study. Material properties for FE simulation were the same as in chapter 2. The unit cells were meshed using tetrahedral elements, and periodic displacement boundary conditions were applied to highlighted faces as defined in COMSOL Multiphysics 5.4:

The Floquet wavenumber k_x^{FB} was parametrically swept while solving for angular frequency $\omega = 2\pi f$ and mode shapes. Corresponding results for the Garolite adherend are shown in figure5.6. Phase c_{ph} and group c_{gr} velocities were computed using the equations 5.1 and 5.2, respectively:

$$c_{ph} = \frac{\omega}{k_x}, \tag{5.1}$$

$$c_{gr} = \frac{{c_{ph}}^2}{c_{ph} - fa\frac{\partial c_{ph}}{\partial(fa)}}, \tag{5.2}$$

where $a = \frac{h}{2}$ is the half thickness of the unit cell. The results are demonstrated in figure 5.7.

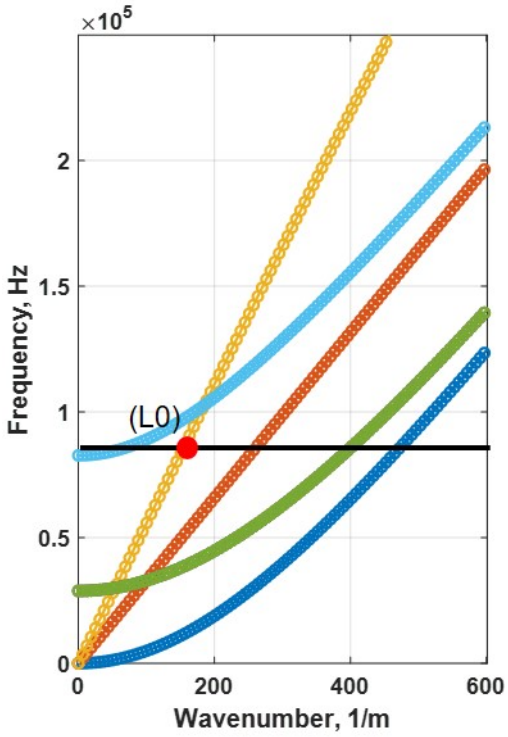

Figure 5.6: Eigenfrequency analysis of the Garolite adherend: wavenumber versus excitation frequency

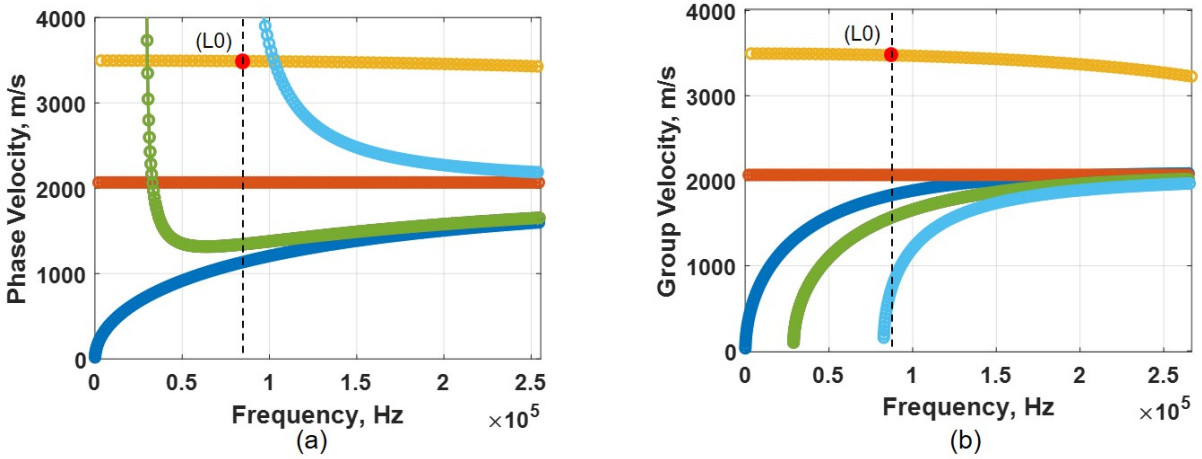

Figure 5.7: Dispersion curves of Garolite adherend: (a) phase velocity; (b) group velocity.

The fundamental longitudinal mode $L0$ was selected for excitation in the lap-joint. As shown in Figure 5.7, the $L0$ mode is largely non-dispersive under 250 kHz, which helps preserve the shape

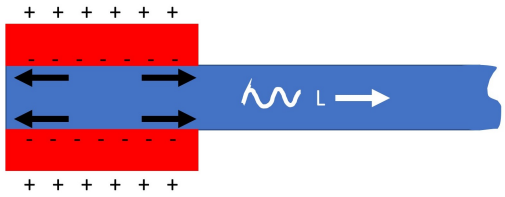

Figure 5.8: Collocated PZT wafer excitation for generation of the $L0$ mode.

of the excitation signal and simplify signal processing. In addition, the $L0$ mode is the easiest to identify among the other modes and reflections in the received signal as it has the highest group velocity. A sqaure surface-bonded PZT wafer introduced in chapter 3 is used here for simulation. Based on the group velocity plot (figure 5.2) longitudinal mode beyond 150 kHz is dispersive, thus 85 kHz is choose for excitation.

5.3.2 Time-depended model of guided wave propagation

ABAQUS CAE with Implicit Dynamic Analysis (IDA) was used to simulate the piezoelectric wafers and guided wave propagation across the lap-joint. The geometry of the lap-joint is presented in figure 5.4. Adhesive was modeled as a viscoelastic material as discussed in chapter 2 in order to account for the damping of ultrasonic waves. The voltage signal applied to actuating PZT wafers was the Morlet wavelet with the central frequency $f_0 = 85\ kHz$ and $V_{pp} = 10\ V$. Figure 5.8 illustrates how the top and bottom PZT wafers were driven in phase in order to generate purely $L0$ mode.

5.3.2.1 FE model configuration

Substrate, adhesive, and piezoelecric domain are all defined as part, meshed (Structured), and assembled to form a long bond line lap joint as shown in figure 5.4. The adherends were meshed using first order C3D8 (3D-brick) elements with maximal size of $1 \times 1 \times 0.78\ mm$, and the adhesive bond-line was meshed using C3D8R elements with maximal size of of $1 \times 1 \times 0.33\ mm$ so that the bond-line had at least 3 elements in the thickness direction. PZT wafers were assumed ideally bonded to the adherends, and were represented using C3D8E piezoelectric elements with maximal

size of $1 \times 1 \times 0.2\ mm$. For the excitation frequency of 85 kHz. Infinite Elements are used at the edges to avoid edge reflection in the simulation as shown in figure 5.4.

The implicit solver was configured to run simulations with fixed 0.1 μs time increments. The displacements were saved for every time increment in order to create snapshots of the ultrasonic wave field. The parametric study was performed by sweeping through material properties of the ABS thermoplastic adhesive obtained experimentally using the DMA. Material parameters adhesive zone A2 is only changed to simulate the localized heating of bondline.

5.3.2.2 Results and Discussion

The wave propagation in the lap-joint is simulated for the time period of 200 μs. Within this time span, the excited longitudinal mode $L0$ propagates from PZT transmitters across the adhesive bond-line and reaches the PZT receiver pair. Voltages generated by the PZT receivers are summed to reduce the effect of flexural modes on the resulting signal. Guided waves undergo mode conversions while entering and while leaving the adhesive bond-line region. This phenomenon combined with varying thicknesses and different dispersion relations in the substrates and the adhesive bond-line may render signal analysis complicated. Hence, in this study, the measured GW signal is cropped to include mostly the fastest $L0$ mode, then its energy is monitored in order to evaluate the bond condition [59].

Guided wave propagation corresponding to different adhesive states is simulated by changing the elastic modulus E of the adhesive and its dynamic viscosity ν as per experimental DMA results from Figure 1.3 and Figure 1.4. The ABS adhesive at 30 °C, 110 °C and 130 °C will be in a fully cured, partially melted and fully melted state, respectively. Thus, the simulation results at these three temperatures are discussed in detail for better understanding of guided wave transmission through the adhesive bond-line. Figure 5.9 shows snapshots of the corresponding displacement fields in the substrate-2 at 60 μs. The energy transfer of guided waves from the top Substrate 1 to the bottom Substrate 2 reduces slightly in the case of partially melted adhesive compared to the case of the fully cured adhesive. However, when the adhesive is fully melted, the energy transfer

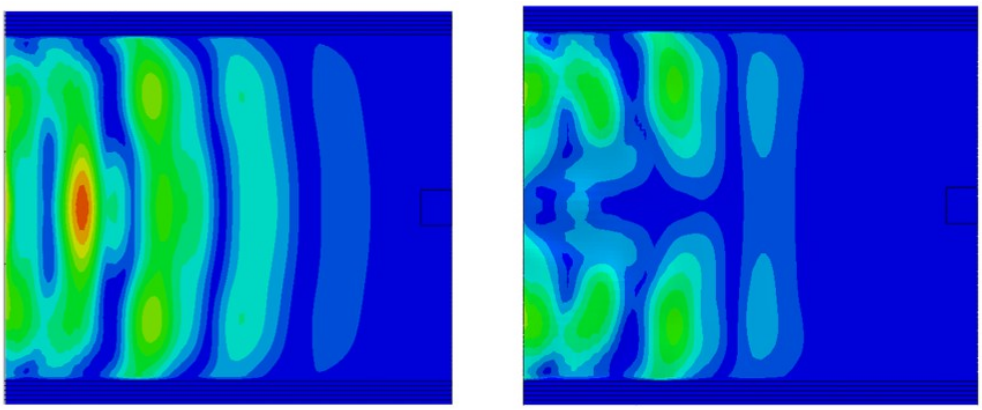

Figure 5.9: Displacement fields in the lap-joint at 60 μs corresponding to different adhesive states: (a) fully cured; and (b) fully melted.

is not zero due to transfer through non-melted regions (A1 and A3). In the process of transitioning from the fully cured to the fully melted state, the magnitude of displacements increases in the top Substrate 1. This indicates that guided waves are trapped in the Substrate 1. They reflect from the top edge in the bond-line region and propagate backwards to the transmitter PZT pair. Figure 5.10 shows the voltage received in the receiver transducer pair. Voltage for top and bottom transducer pair are summed up to maximize longitudinal mode reception. Received voltage signals indicate both amplitude and phase shift or Time of Flight (TOF) while the adhesive is being melted. Thus both energy transfer and TOF are clearly an indicative feature for heal and process monitoring.

Figure 5.11 presents the TOF and Energy transfer T_c of the received waveform at different healing stages. From figure 5.11(b) It can be seen that initially there is no induction heating applied until healing timeline 3, later the induction heating is applied from stages 3 to 6 where there is a steady increase in TOF. This indicates the adhesive A2 is melting and thus the guided waves take time to arrive at the received PZT pair from the adjacent adhesives (A1 and A3). Energy transfer T_c of the received waveform at different adhesive stages are calculated according to Equation 5.3.

$$T_c = \int_{f_1}^{f_2} |\hat{s}(f)|^2 df, \tag{5.3}$$

where $\hat{s}(f) = \int_{-\infty}^{\infty} e^{-i(2\pi f)t} s(t) dt$ is the Fourier transform of the acquired and cropped signal $s(t)$,

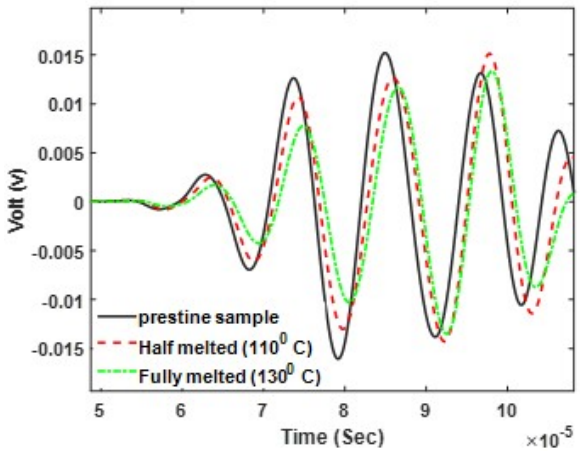

Figure 5.10: Voltage acquired by the receiver transducer pair

and f_1 and f_2 are the lower and upper frequencies which are $+/-$ 15 kHz from the corresponding excitation central frequency 85 kHz. Figure 5.11 (a) shows the energy transfer while a section of bond line is being heated. Initially there is no induction heating applied until healing timeline 3, where the energy transfer is constant. Later the adhesive properties are changed to simulate a heating condition from stages 3 to 6, where there is a 60% loss in energy transfer. This indicates the adhesive A2 is melting and thus the guided waves are not effectively transferred to the substrate-2. 40% of energy being transferred after heating timeline 6 are via adhesive sections A1 and A3. Based on the results, Both energy transfer and TOF shall be used as an indicative feature to control the healing process.

5.4 Summary and Conclusion

In this chapter, a single lap-joint is processed using guided wave controlled processing technique and subjected to fatigue loads. Lap-joint that had fatigue damage are healed using guided wave controlled induction healing technique. Overall the life cycle monitoring of the single lap-joint is demonstrated here. Further, joints prepared with, without and guided wave controlled healing are mechanically tested. Mechanical strength testing of healed samples show the controlled healing was able to restore 98% of original strength. In addition, healing of long bondline is also numerically investigated. Based on the numerical results, Both energy transfer and TOF are sensitive features

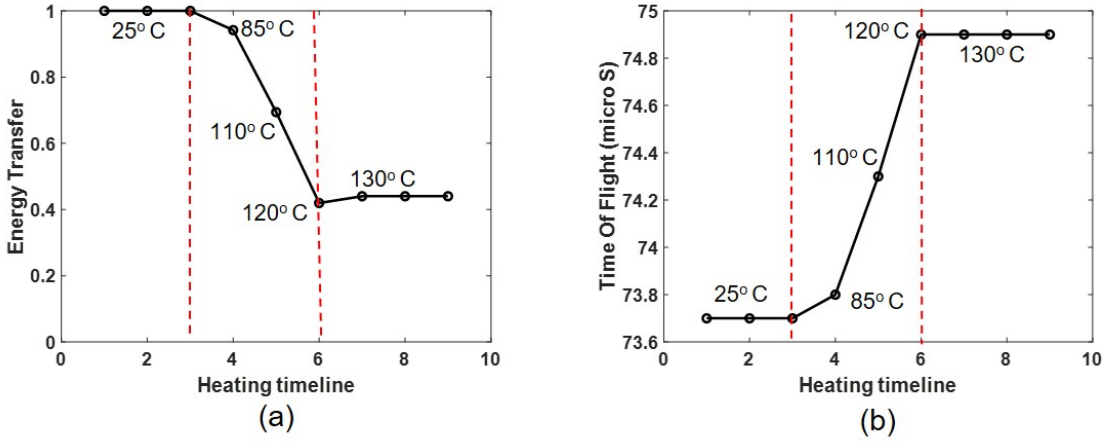

Figure 5.11: Energy transfer(a) and TOF(b) of received waveform with different heating stages while healing

towards bondline healing. Thus, the developed life-cycle monitoring technique shall be easily extended to longer bondlines.

CHAPTER 6

MATERIAL CHARACTERIZATION USING SMART SKIN

6.1 Introduction

Tailoring the structural properties through strategic lamina layup is one of the biggest advantages that fiber reinforced polymer (FRP) composites offer. These FRP composites are designed to handle complex mechanical, thermal and diffusion loading, and the damage is accumulated over time. While many non-destructive (NDE) techniques are available to determine the flaw(s) or defects, the gradual degradation in elastic properties cannot be detected until the flaw is formed. earlier work on 3 on determining the degradation of adhesive under cyclic loading has shown that the guided wave/lamb-wave technique is an excellent method to back-calculate the elastic properties (modulus) and its degradation over time. In this work, instead of one actuation-receiving sensor pair, an array of sensors were used to determine the elastic properties (Modulus) in multiple directions. Furthermore, since most automotive structural components are curved, hence this research aims at developing a conformable sensing skin that estimates the elastic moduli in multiple directions including curved surfaces. A Single-Transmitter-Multiple-Receiver (STMR) Piezo-ceramic based sensor array is embedded to a conformable skin, called as Smart skin. The developed Smart skin can be attached to any surface using pressure sensitive adhesive.

Application of GW in material characterization and damage detection has been successfully demonstrated in several studies [77, 30, 75, 38] Recent studies used GW to detect disbonds, cracks, perform quality control, and in-service fatigue monitoring [64, 16, 24, 25, 6, 7] A MTMR configuration is generally used for material characterization. In most of the above-mentioned studies, piezo-ceramic sensors are permanently bonded to the surface of the substrate during inspection. In this study we have developed a smart skin where the emended sensors can be reused. An inverse Rayleigh lamb wave technique is used to estimate the material properties in different direction. Schematic of inverse Rayleigh technique is shown in figure 6.1 This technique

is validated on a aluminum sample in identifying the material modulus in each direction. To enable rapid material classification, machine learning models are used to process the data collected form smart skin.

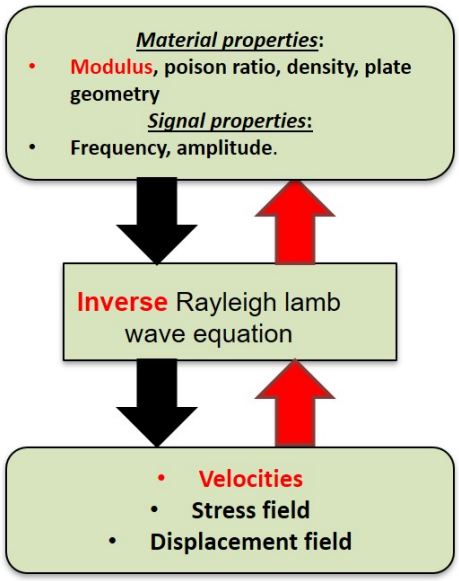

Figure 6.1: Schematic of inverse Rayleigh lamb wave technique for material characterization

To demonstrate the ability of material classification two grades of Aluminum having same thickness are chosen. Shallow machine learning models need efficient feature extraction for correct classification. Thus, the experimental signals are first pre-processed by clearing the offsets and by excluding the transmitted signal from the received ones. Then 21 features such as wavelet coefficients, zero crossing coefficients, mean, energy, standard deviation etc. are extracted. These obtained features are then feed into Support Vector Machine (SVM) classification algorithms [58] for material characterization. However, extracting meaningful features are time consuming and need opinion of experts [67]. Moreover, with massive amount of data these days there is possibility of erroneous classification and detection as the number of features become excessive which is called curse of dimensionality [73]. Feature extractions and dimension reductions by Principal Component Analysis (PCA) though has great interpretability, but can leave out features with small contributions which can entail important information about material characterization. Deep

learning involving Convoluted Neural Networks (CNN) show promising results as these networks reduce the manual design effort of feature extraction. Features are extracted directly from the raw data by these networks [39]. Here the experimental images are directly feed into the developed 2D CNN network for binary classification.

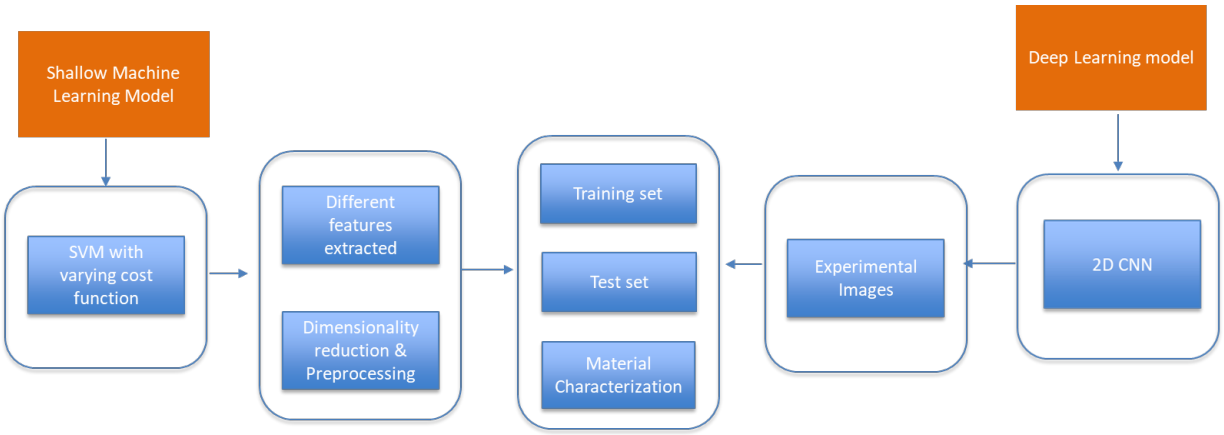

Figure 6.2: Schematic of the characterization methodology

Figure 6.2 shows the schematic of the working methodology in this research work. This chapter is organized as follows. Section 6.2 and 6.3 describes the fabrication of smart skin and its application in Guided wave transmission and acquisition on aluminum plate. Section 6.5 illustrate the features extracted from experimental data and how they are used in SVM. Section 6.6 shows the development of 2D CNN technique. Results of material classification using SVM and 2D CNN are discussed in section 6.6.1. Summary, conclusion, and future work are presented finally.

6.2 Development of Smart Skin

A Multiple-Transmitter-Multiple-Receiver (MTMR) Piezo-ceramic based sensor (PZT) array is embedded to a conformable skin. The bottom layer of the skin is coated with pressure-sensitive adhesive to be attached to most curved and non-curved structural surfaces (refer Figure 2). Each PZT sensor nodes are individually controlled by a MATLAB code that actuates and receive the GW waves signals. The skin could actuate and receive GW waves in each direction of the material. Further,

the reusable sensors can be deployed in an array configuration for multi-purpose NDE. Figure 3 shows the application of “SMART SKIN” on an Aluminum plate for material characterization.

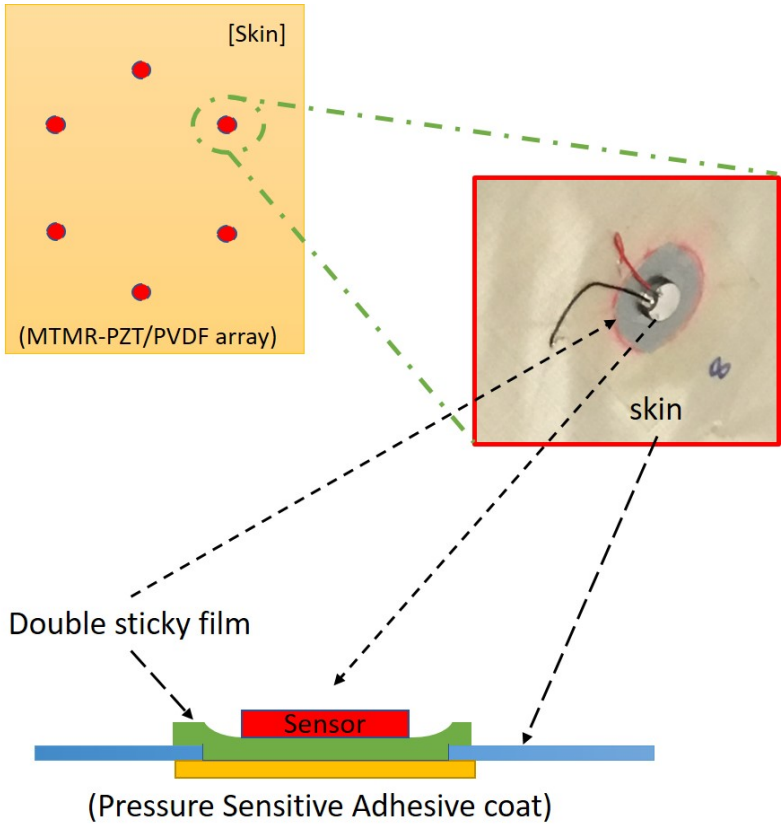

Figure 6.3: Schematic of smart skin

6.3 Experiments

Two different grade of aluminum plates with same thickness as shown in Table 1 are chosen for classification

The block diagram in Figure 6.4 Smart skin attached to aluminum sample with GW DAQ setupshows the GW experimental setup. It consisted of 1) Smart skin deployed on the aluminum sample, 2) arbitrary waveform generator 33220A from Keysight Technologies, 3) Oscilloscope DSO 1004A from Keysight Technologies. Piezoelectric transduces embedded on smart skin were electrically connected to the output of the waveform generator. Excitation was done using a

Sample (Name)	Thickness (mm)	Elastic Modulus, E (Gpa)
AL - 6061 (AL_1)	1.6	68.9
AL - 2024 (AL_2)	1.6	73.1

Table 6.1: Properties of selected Aluminum sample

Morlet wavelet function with center frequency of 150 kHz. Guided waves transmitted through the aluminum plate were sensed using piezoelectric receivers, which were connected to the oscilloscope. Data was then transferred to a PC with MATLAB.

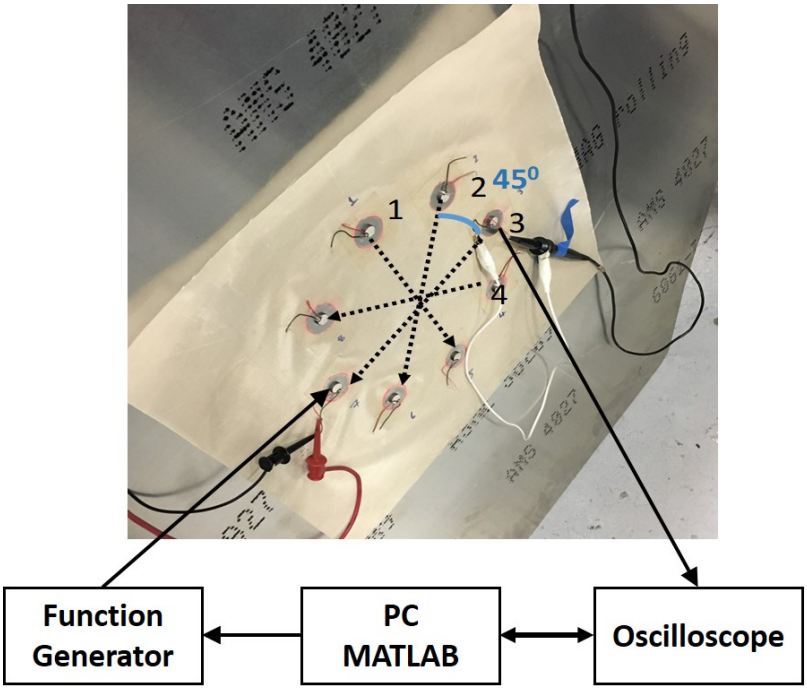

Figure 6.4: Smart skin attached to aluminum sample with GW DAQ setup

Based on the dispersion analysis for selected aluminum plates, excitation of 150 kHz would avoid any higher-modal excitation and lower dispersion of excited wave. Excited and received signal from one pair of transducers are shown in Figure 6.5.

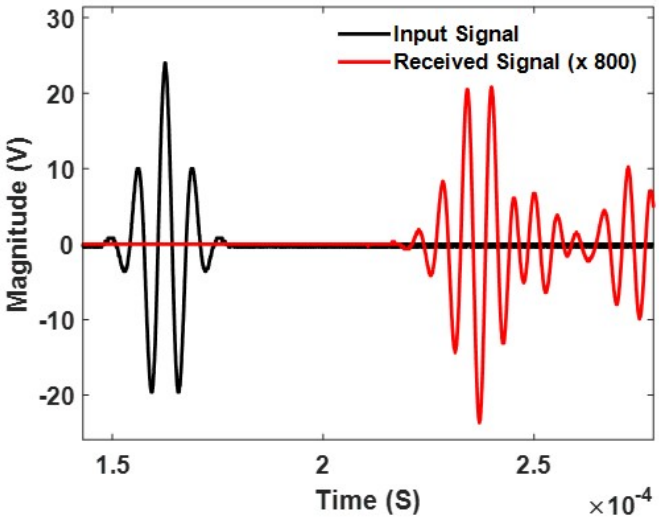

Figure 6.5: Excited and received guided wave signal form smart skin

6.4 Inverse Rayleigh Lamb Wave Technique

For an isotropic plate, Rayleigh-Lamb governing equation shall be used to estimate the multi-modal dispersion curves [50]. This equation requires wave-guided parameters such as thickness, elastic modulus, poisons ratio and density of the material. Using the dispersion curves, we shall further estimate velocity, stress and displacement filed of the propagating wave as shown in figure 6.1. The inverse optimization is also possible where the experimentally measured guided wave parameters such as velocity of selected mode-frequency combination shall be used to estimate the intrinsic material properties of the wave guide.

In this research work, velocities measured on AL 6061 using smart skin as shown in section 6.3 is used in inverse Rayleigh-Lamb wave optimization technique to estimate the modulus of wave-guide. Estimated elastic modulus of Aluminum sample is shown in figure 6.6. The results clearly indicates the algorithm is effective in estimating the elastic modulus at 4 different directions. Estimation error is highly dependent of time of flight (TOF) calculation.

This technique requires accurate calculation of TOF between actuated and received waveform. Some mode-frequency combinations are dispersive and mixed with other modes, thus accurate

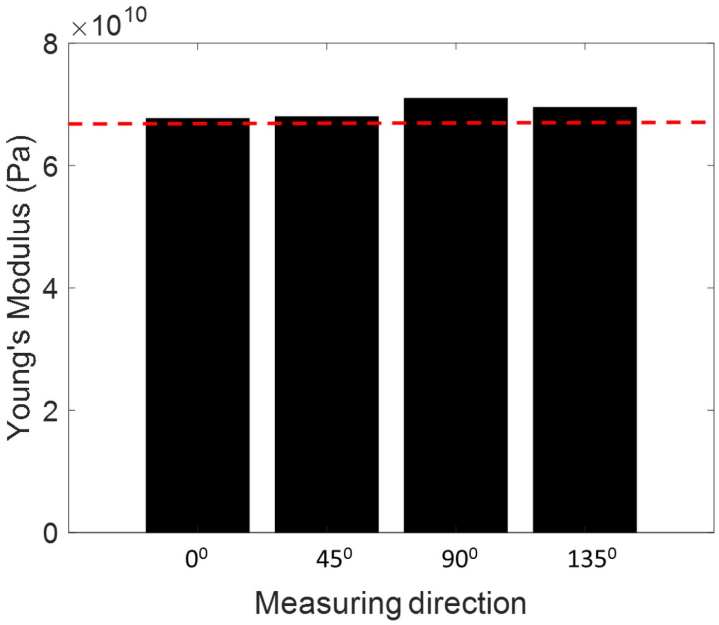

Figure 6.6: Estimated Elastic modulus of Al-6061 in 0^0, 45^0, 90^0 and 135^0

TOF estimation requires high skills. Due to this limitation, functional data analysis techniques are explored in the following sections.

6.5 Numerical Methods

Material classification of two grades of Aluminum is a binary classification problem. For each specimen type 40 signals are acquired. Thus, the entire data consists of 80 patterns where from each pattern 21 features are extracted. The data set is divided into 50 training data, 10 data for validation set and remaining 20 for test set. The extracted features are feed into shallow machine learning network (SVM) and the direct experimental images to deep learning network, 2D CNN.

6.5.1 Feature Extraction

Signals have been normalized by considering the absolute of the maximum of the signals. Then from those normalized values different features like mean, variance, energy, zero crossing coefficients and discrete wavelet transform (DWT) are obtained. Wavelet transform constitutes an important feature as the guided wave based ultrasonic signals contain various stationary and non-stationary

characteristics. Thus, signal analysis by wavelet decompositions provides an efficient method in NDE and SHM community compared to that with Fourier transforms [14, 48] From the experimental signals the offsets and transmitted signal is being eliminated. Now on this transformed signal, Debauchies wavelet of level 4 based on Mallat's pyramidal algorithm [45] has been used as an extracted feature. Zero crossing is the place where the sign of a mathematical function changes, thus providing another important feature [29]. At zero crossing, the time points where the amplitude of the experimental signal crosses zero has been considered. The insignificant segments at the beginning are ruled out by setting a minimum pass filter on standard deviation and maximum amplitude metrics at 10%. Different significant features as obtained from an experimental signal are shown in Figure 6.7.

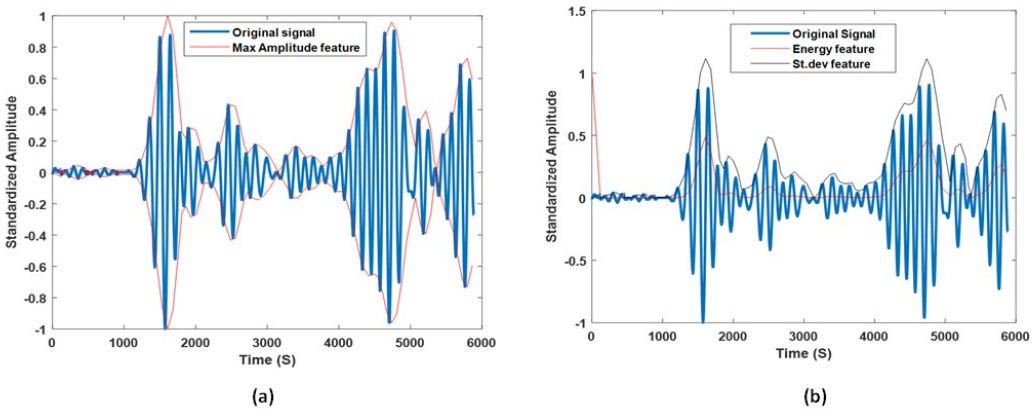

Figure 6.7: (a) maximum signal envelope of the signal, (b) standard deviation and energy feature of the signal

6.5.2 Description of the Dataset

The bar plot below shows the distribution of the features across the two classes. Color red (label 1) represents the class of AL1 sample whereas light green (label2) represents the AL2 sample. As different features have different ranges, hence the features are normalized to the same scale in bar plot.

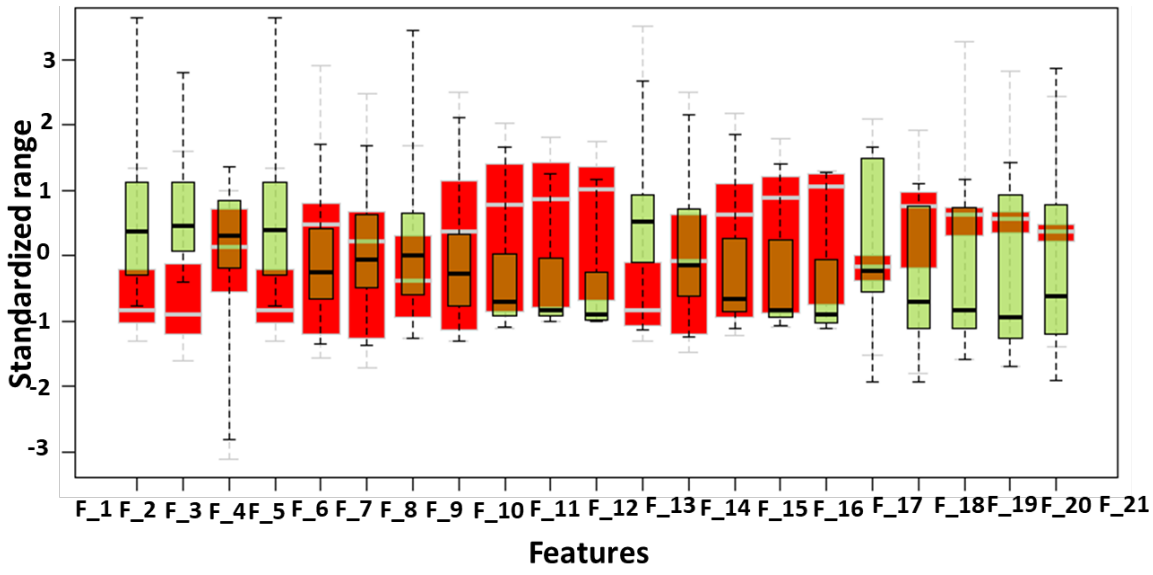

Figure 6.8: Feature distributions in bar plots representing A1 in red and A2 in light green. F1 stands for Feature1

Variability Coverage by the Principal components				
1 PC	**2 PCs**	**3 PCs**	**4 PCs**	**5 PCs**
47.13%	68.26%	79.84%	84.96%	89.57%
6 PCs	**7 PCs**	**8 PCs**	**9 PCs**	**10 PCs**
93.73%	95.41%	96.59%	97.65%	98.52%
11 PCs	**12 PCs**	**13 PCs**	**14 PCs**	**15 PCs**
99.19%	99.47%	99.65%	99.78%	99.90%
16 PCs	**17 PCs**	**18 PCs**	**19 PCs**	**20 PCs**
99.96%	99.99%	99.99%	100%	100%

Table 6.2: Variability coverage based on Principal components (PC)

6.5.3 Data Analysis

Dimension reduction is done by Principal Component Analysis (PCA) where 5 PC and 10 PC directions are used as extracted features forming two different datasets and the results are compared with that on original dataset. Table 2: Variability coverage based on Principal components (PC)shows the cumulative variability coverage by the PCA components. The table shows that the three few PCA components do not cover the entire variability of the data.

Figure 6.9 shows the variability in dataset based on first two principal components. From the

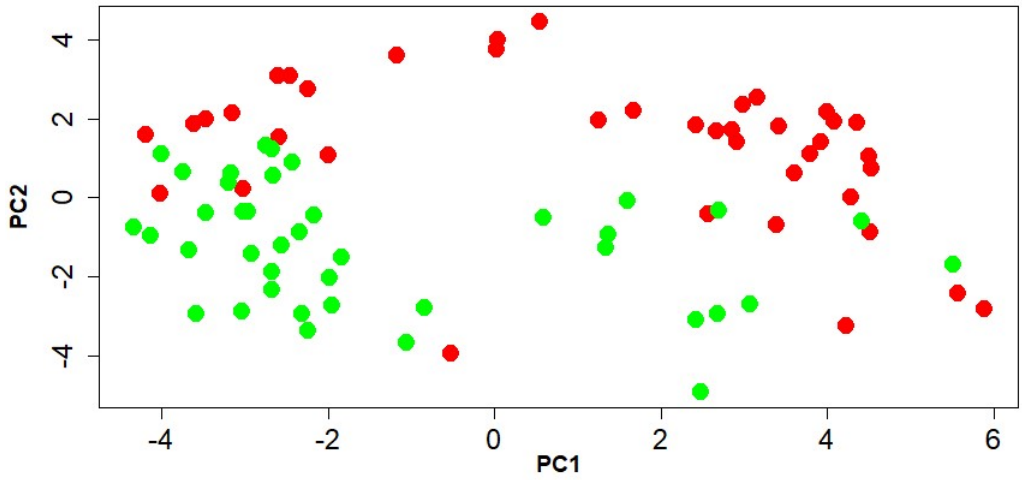

Figure 6.9: Data representation based on first two principal components

below picture it is clear that it is hard to distinguish the two classes based on two PCs as there is overlap between the 2 classes

The AL1 class is shown in red whereas AL2 class is shown in dark green. Hence it is better to perform the classification analysis by taking into consideration more than 4 principal components or without dimension reduction. Support Vector Machine (SVM) is applied where the cost parameter is varied from 1 to 10 on both the training and test sets. It is seen that cost parameter 8 produces the optimal result on the test set. Figure 8 shows the train and test errors when SVM is applied. Choosing the cost parameter as 8 gives the lowest misclassification rate on the test set.

6.6 2D Convolution Neural Network

Recently in the field of Nondestructive evaluation (NDE), studies involving defect classifications and material characterization using deep learning is gaining prominence [43, 33, 47]. Here we have developed a 2D CNN network to perform the material characterization between two grades of Aluminum. The experimental data here are stored in the form of images of dimension 300X30. The deep learning models are developed in using keras and TensorFlow in Google Colab platform.

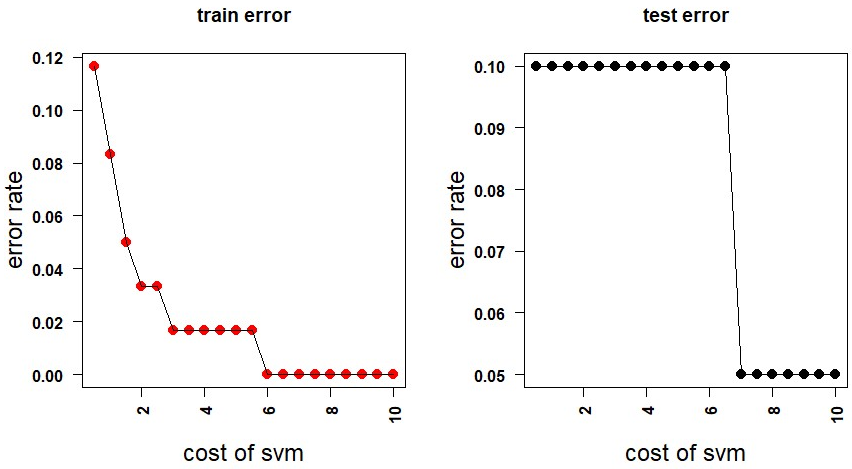

Figure 6.10: Error rate for different values of cost function

A 2D CNN network uses convolution operation and deals with data in grid formats where it learns features in a hierarchical fashion by constructing deep neural architecture [23]. The network comprised of 5 convolutional layers and 3 fully connected dense layers. Maximum pooling layers and dropout layers are also present on order to remove dimension and to introduce regularization respectively. The first convolutional layer contains 32 kernales each of size 3X3 and stride as 1. After second convolution the output dimension reduces to 296X296X32. Then maximum pooling of window size 2x2 is applied which reduces the output dimension to 148X148X32. Next dropout is introduced to reduce regularization. Then another layer of convolution, maxpooling and dropout layer is applied which further reduces the dimension to 73X73X32. The fourth convolutional layer contains 64 kernels modifying the output dimension to 71X71X64. as the non-linear activation function in the convolutional and dense layers. The optimizer used in the model is ADAM. Figure 6.11 shows the schematic of the described architecture of the 2D CNN.

6.6.1 Results and Discussions

In this section the performance of the shallow machine learning algorithms SVM on the extracted features and deep learning algorithm 2D CNN on the experimentally gathered data are compared.

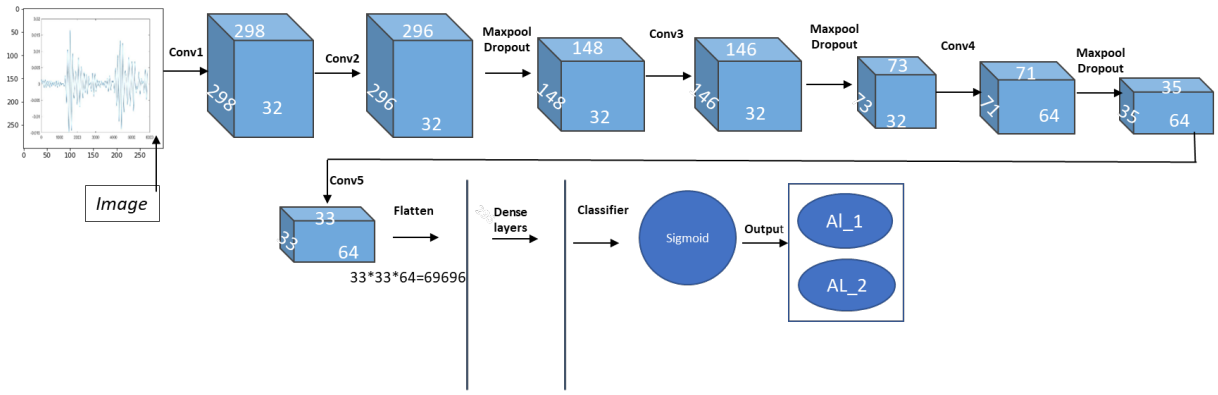

Figure 6.11: Schematic of the developed 2D CNN model

Out of total 80 data, 50 are used for training, 10 for validation and rest 20 are used for testing. Figure 6.12 shows the train and validation accuracies and losses as obtained from the 2D CNN. The accuracy obtained using 2D CNN on test dataset is 100%. Deep learning model is successful in material characterization.

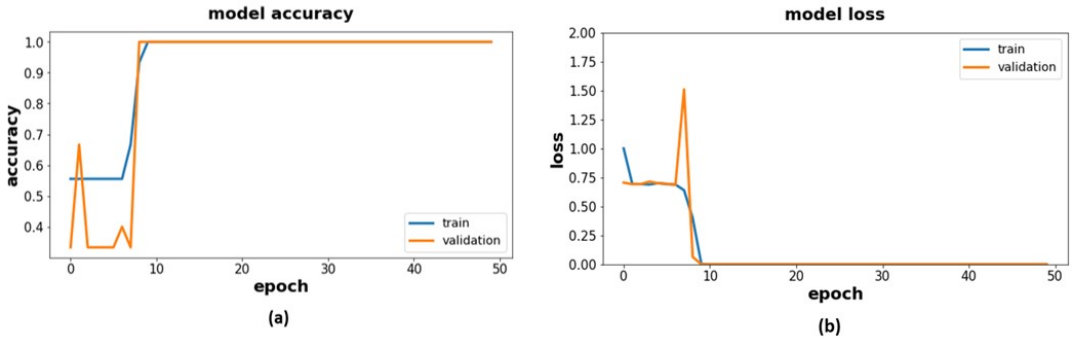

Figure 6.12: Illustrating the 2D CNN accuracy(a) and loss(b) on the original dataset

The shallow machine learning models also produce accurate classification results as the dataset is small. we receive the accurate classification choosing cost parameter as 8 in SVM gives the accuracy of 95%. Thus, due to a smaller number of data almost all the classifiers give 100% accuracy. Figure 6.13 shows the confusion matrix for SVM and 2D CNN.

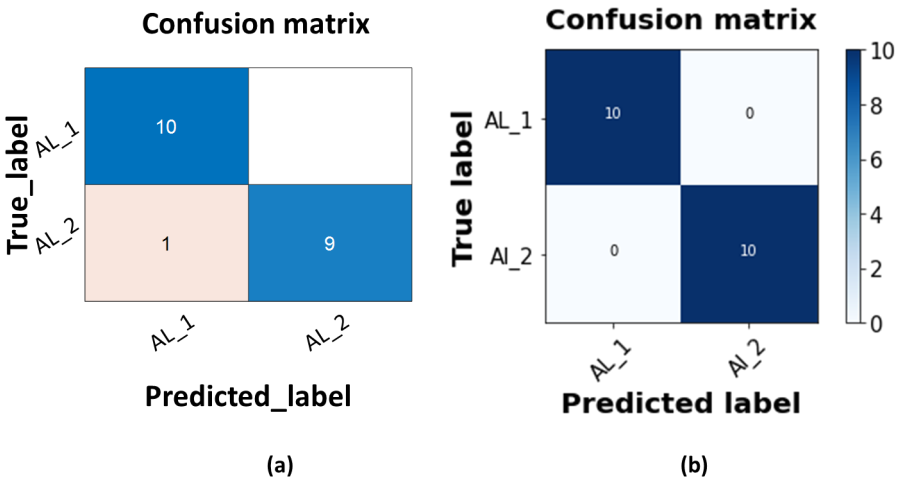

Figure 6.13: Confusion matrix of (a) SVM, (b) 2D CNN

6.7 Summary and Conclusion

This chapter presents the development of smart skin for reusable and rapid NDE. Inverse Rayleigh-Lamb wave technique was successfully used to identify material modulus in aluminum sample. Rapid Material classification is one of the applications of smart skin. This application is achieved with machine learning algorithms. SVM and 2D CNN is used successfully to classify two different grades of aluminum plate. Classification results are promising and clearly indicates the ability to use smart skin for rapid material classification and identification.

CHAPTER 7

SUMMARY AND CONCLUSIONS

In this chapter, a summary of all the work done in Life cycle monitoring of reversible adhesive bonded joints are revisited and conclusions of all the research findings are presented.

Ultrasonic guided wave sensing and optical frequency domain reflectometry techniques were successfully implemented for real-time monitoring of melting and curing processes in a Garolite lap-shear joint with nano-Fe_3O_4 reinforced ABS adhesive. The thermoplastic adhesive was remotely heated at 200 kHz with the help of a 6.6 kW commercial induction heater and a water-cooled solenoid. The embedded FMNPs interacted with the applied electromagnetic field by generating heat due to hysteresis losses and eddy currents between locally agglomerated nano-particles. The electromagnetic system was controlled using pulse-width modulation and was programmed to terminate the heating process based on guide wave measurements so that the adhesive wouldn't suffer thermal degradation.

Guided waves were excited and sensed using surface-bonded PZT wafers bonded on to both adherends. Dispersion relations corresponding to the adherends and the bond-line region were obtained in Comsol Multiphysics 5.4 based on the Floquet-Bloch theory. The state of adhesive was actively monitored by passing the fundamental $L0$ mode at 35 kHz across the bond-line from one adherend to another. The $L0$ mode was selected due to its high sensitivity to material properties of the adhesive and its high group velocity that helped simplify signal processing. Ultrasonic wave propagation was simulated in Abaqus CAE 6.14 in order to map the transmission coefficient of the $L0$ mode to the Young's modulus of the adhesive. In FE modeling, the nano-Fe_3O_4 reinforced ABS plastic was simulated as a viscoelastic material, and it's properties were obtained experimentally using the dynamic mechanical analysis. A non-linear relationship between the Young's modulus of the adhesive and the FE transmission coefficient of the $L0$ mode was later applied to experimental guided wave signals.

In addition to guided wave measurements, distributed measurements of temperature within

the adhesive bond-line were successfully acquired using the strategically embedded optical fiber. A Rayleigh back-scattering OFDR system ODiSI-B from Luna Innovations provided temperature profiles of the adhesive at a rate of 10 Hz and with a spatial resolution of 1.5 mm. Measured temperature distributions were averaged along the length of the embedded section of the optical fiber. Then, similarly to the guided wave technique, temperature averages were converted to the Young's modulus of the adhesive based on the DMA data.

The advantages of EM bonding with guided wave and fiber-optic feedback were successfully demonstrated in the experiments with a manufactured lap-joint specimen. Implementing guided wave and fiber-optic sensing provided real-time monitoring of the adhesive state by displaying the effective Young's modulus of the adhesive. Both techniques accurately captured a transition from a solid to a viscoelastic state at which the modulus dropped down to nearly zero values. At that stage, the EM heating was automatically disabled at a prescribed temperature of 130°C to avoid thermal damage. In addition, guided wave and fiber-optic systems correctly sensed the curing of the adhesive after the EM field was removed. As the lap-joint was let cool down to the room temperature and eventually turned solid, measured Young's modulus of the adhesive went up to its original value observed before EM heating. Obtained experimental results demonstrated the stability of the proposed EM bonding process.

During in-service life-stage of lap joint, GW technique is used for prognosis and diagnosis of fatigue damage. Mechanical test results reveal that the damage area growth is rapid in the first 400 cycles followed by slow growth rate until complete failure. A similar trend was noticed in the transmission coefficients of the GW signals and optical images as the damage area grew in size, hence denoting the sensitivity of the NDE technique for damage diagnosis in composite SLJs. Two samples where successfully validated for diagnosis of fatigue damage with guided wave measurements only. Further, a data-driven prognosis technique is introduced and guided wave data are used for prediction of damage area in upcoming cycles and Remaining useful life. Final validation of prognosis results show a reliable prediction of damage area and RUL. For the healing stage in life cycle monitoring, a single lap-joint is processed using guided wave controlled

processing technique and subjected to fatigue loads. Lap-joint that had fatigue damage are healed using guided wave controlled induction healing technique. Overall the life cycle monitoring of the single lap-joint is demonstrated here. Further, mechanical strength testing validates the reliability of developed life cycle monitoring technique. In addition, healing of long bondline is also numerically investigated. Based on the numerical results, The developed monitoring technique shall be easily extended to longer bondlines.

Finally a smart skin was developed for reusable and rapid NDE application. Inverse Rayleigh-Lamb wave technique was successfully used to identify material properties of aluminum sample. Rapid Material classification is one of the applications of smart skin. This application is achieved with machine learning algorithms. SVM and 2D CNN is used successfully to classify two different grades of aluminum sheet. Classification results are promising and clearly indicates the ability to use smart skin for rapid material classification. Overall, the proposed GW based life-cycle monitoring technique is successfully validated in reversible single lap joint. This technique shall be extended to air-coupled robotic setup where life cycle monitoring of complex automotive joints are possible.

BIBLIOGRAPHY

BIBLIOGRAPHY

[1] MM Abdel Wahab. Fatigue in adhesively bonded joints: a review. *ISRN Materials Science*, 2012, 2012.

[2] MM Abdel Wahab, I Hilmy, IA Ashcroft, and AD Crocombe. Evaluation of fatigue damage in adhesive bonding: part 2: single lap joint. *Journal of Adhesion Science and Technology*, 24(2):325–345, 2010.

[3] Dawn An, Joo-Ho Choi, and Nam H Kim. Identification of correlated damage parameters under noise and bias using bayesian inference. *Structural Health Monitoring*, page 1475921711424520, 2011.

[4] James H Aubert. Note: Thermally removable epoxy adhesives incorporating thermally reversible diels-alder adducts. *The journal of adhesion*, 79(6):609–616, 2003.

[5] MR Ayatollahi, M Samari, SMJ Razavi, and LFM da Silva. Fatigue performance of adhesively bonded single lap joints with non-flat sinusoid interfaces. *Fatigue & Fracture of Engineering Materials & Structures*, 40(9):1355–1363, 2017.

[6] Portia Banerjee, Oleksii Karpenko, Lalita Udpa, Mahmood Haq, and Yiming Deng. Prediction of impact-damage growth in gfrp plates using particle filtering algorithm. *Composite Structures*, 194:527–536, 2018.

[7] Portia Banerjee, Rajendra Prasath Palanisamy, Mahmood Haq, Lalita Udpa, and Yiming Deng. Data-driven prognosis of fatigue-induced delamination in composites using optical and acoustic nde methods. In *2019 IEEE International Conference on Prognostics and Health Management (ICPHM)*, pages 1–10. IEEE, 2019.

[8] Portia Banerjee, Rajendra Prasath Palanisamy, Lalita Udpa, Mahmood Haq, and Yiming Deng. Prognosis of fatigue induced stiffness degradation in gfrps using multi-modal nde data. *Composite Structures*, 229:111424, 2019.

[9] T Bayerl and P Mitschang. Heating of polymer-polymer composites by inductive means. In *18th International Conference on Composite Materials Proceedings*, 2009.

[10] Thomas Bayerl. Application of particulate susceptors for the inductive heating of temperature sensitive polymer-polymer composites. 2012.

[11] Thomas Bayerl, Miro Duhovic, Peter Mitschang, and Debes Bhattacharyya. The heating of polymer composites by electromagnetic induction–a review. *Composites Part A: Applied Science and Manufacturing*, 57:27–40, 2014.

[12] Thomas Bayerl, Ralf Schledjewski, and Peter Mitschang. Induction heating of thermoplastic materials by particulate heating promoters. *Polymers and Polymer Composites*, 20(4):333–342, 2012.

[13] Anis Ben Abdessalem, Romain Azaïs, Marie Touzet-Cortina, Anne Gégout-Petit, and Monique Puiggali. Stochastic modelling and prediction of fatigue crack propagation using piecewise-deterministic markov processes. *Proceedings of the Institution of Mechanical Engineers, Part O: Journal of Risk and Reliability*, 230(4):405–416, 2016.

[14] Fairouz Bettayeb, Tarek Rachedi, and Hamid Benbartaoui. An improved automated ultrasonic nde system by wavelet and neuron networks. *Ultrasonics*, 42(1-9):853–858, 2004.

[15] A Bund, H Chmiel, and G Schwitzgebel. Determination of the complex shear modulus of polymer solutions with piezoelectric resonators. *Physical Chemistry Chemical Physics*, 1(17):3933–3938, 1999.

[16] Michel Castaings. Sh ultrasonic guided waves for the evaluation of interfacial adhesion. *Ultrasonics*, 54(7):1760–1775, 2014.

[17] Yuanguo Chen. *Viscoelastic modeling of flexible pavement*. PhD thesis, University of Akron, 2009.

[18] R Ciardiello, G Belingardi, F Litterio, and V Brunella. Thermomechanical characterization of reinforced and dismountable thermoplastic adhesive joints activated by microwave and induction processes. *Composite Structures*, page 112314, 2020.

[19] R Ciardiello, G Belingardi, B Martorana, and V Brunella. Physical and mechanical properties of a reversible adhesive for automotive applications. *International Journal of Adhesion and Adhesives*, 89:117–128, 2019.

[20] M Corbetta, C Sbarufatti, A Saxena, M Giglio, and K Goebel. Model-based fatigue prognosis of fiber-reinforced laminates exhibiting concurrent damage mechanisms. 2016.

[21] ASTM D 5868. Astm international. d5868-01(2014) standard test method for lap shear adhesion for fiber reinforced plastic (frp) bonding. Technical report, West Conshohocken, PA; ASTM International, 2014.

[22] Lucas FM Da Silva, Andreas Öchsner, and Robert D Adams. *Handbook of adhesion technology*. Springer Science & Business Media, 2011.

[23] George E Dahl, Tara N Sainath, and Geoffrey E Hinton. Improving deep neural networks for lvcsr using rectified linear units and dropout. In *2013 IEEE international conference on acoustics, speech and signal processing*, pages 8609–8613. IEEE, 2013.

[24] RP Dalton, P Cawley, and MJS Lowe. The potential of guided waves for monitoring large areas

of metallic aircraft fuselage structure. *Journal of Nondestructive Evaluation*, 20(1):29–46, 2001.

[25] Bruce W Drinkwater, Michel Castaings, and Bernard Hosten. The measurement of a 0 and s 0 lamb wave attenuation to determine the normal and shear stiffnesses of a compressively loaded interface. *The Journal of the Acoustical Society of America*, 113(6):3161–3170, 2003.

[26] Nagi Gebraeel, Mark Lawley, Richard Liu, and Vijay Parmeshwaran. Residual life predictions from vibration-based degradation signals: a neural network approach. *IEEE Transactions on industrial electronics*, 51(3):694–700, 2004.

[27] Victor Giurgiutiu. Tuned lamb wave excitation and detection with piezoelectric wafer active sensors for structural health monitoring. *Journal of intelligent material systems and structures*, 16(4):291–305, 2005.

[28] Pablo Gómez García and José-Paulino Fernández-Álvarez. Floquet-bloch theory and its application to the dispersion curves of nonperiodic layered systems. *Mathematical Problems in Engineering*, 2015, 2015.

[29] Robert C Higgins. The utilization of zero-crossing statistics for signal detection. *The Journal of the Acoustical Society of America*, 67(5):1818–1820, 1980.

[30] Bernard Hosten, Michel Castaings, Hervé Tretout, and Hubert Voillaume. Identification of composite materials elastic moduli from lamb wave velocities measured with single sided, contactless ultrasonic method. In *AIP Conference Proceedings*, volume 557, pages 1023–1030. American Institute of Physics, 2001.

[31] Chao Hu, Byeng D Youn, Pingfeng Wang, and Joung Taek Yoon. Ensemble of data-driven prognostic algorithms for robust prediction of remaining useful life. *Reliability Engineering & System Safety*, 103:120–135, 2012.

[32] Tyler B Hudson and Fuh-Gwo Yuan. Automated in-process cure monitoring of composite laminates using a guided wave-based system with high-temperature piezoelectric transducers. *Journal of Nondestructive Evaluation, Diagnostics and Prognostics of Engineering Systems*, 1(2), 2018.

[33] Shivprakash Iyer and Sunil K Sinha. A robust approach for automatic detection and segmentation of cracks in underground pipeline images. *Image and Vision Computing*, 23(10):921–933, 2005.

[34] Audrius Jankauskas and Liudas Mazeika. Ultrasonic guided wave propagation through welded lap joints. *Metals*, 6(12):315, 2016.

[35] Henghua Jin, Gina M Miller, Nancy R Sottos, and Scott R White. Fracture and fatigue response of a self-healing epoxy adhesive. *Polymer*, 52(7):1628–1634, 2011.

[36] GJ Kacprzynski, A Sarlashkar, MJ Roemer, A Hess, and B Hardman. Predicting remaining life by fusing the physics of failure modeling with diagnostics. *JOM Journal of the Minerals, Metals and Materials Society*, 56(3):29–35, 2004.

[37] Oleksii Karpenko, Ermias Koricho, Anton Khomenko, Gerges Dib, Mahmoodul Haq, and Lalita Udpa. Multitechnique monitoring of fatigue damage in adhesively bonded composite lap-joints. In *AIP Conference Proceedings*, volume 1650, pages 1102–1111. American Institute of Physics, 2015.

[38] Casey J Keulen, M Yildiz, and Afzal Suleman. Damage detection of composite plates by lamb wave ultrasonic tomography with a sparse hexagonal network using damage progression trends. *Shock and Vibration*, 2014, 2014.

[39] Donghwoon Kwon, Hyunjoo Kim, Jinoh Kim, Sang C Suh, Ikkyun Kim, and Kuinam J Kim. A survey of deep learning-based network anomaly detection. *Cluster Computing*, 22(1):949–961, 2019.

[40] Francesco Lanza di Scalea, Piervincenzo Rizzo, and Alessandro Marzani. Propagation of ultrasonic guided waves in lap-shear adhesive joints: case of incident a 0 lamb wave. *The Journal of the Acoustical Society of America*, 115(1):146–156, 2004.

[41] C James Li and Hyungdae Lee. Gear fatigue crack prognosis using embedded model, gear dynamic model and fracture mechanics. *Mechanical systems and signal processing*, 19(4):836–846, 2005.

[42] Guoqiang Li, Gefu Ji, and Ouyang Zhenyu. Adhesively bonded healable composite joint. *International journal of adhesion and adhesives*, 35:59–67, 2012.

[43] Tianyuan Liu, Jinsong Bao, Junliang Wang, and Yiming Zhang. A hybrid cnn–lstm algorithm for online defect recognition of co2 welding. *Sensors*, 18(12):4369, 2018.

[44] Yuchen Lu, James Broughton, and Pat Winfield. A review of innovations in disbonding techniques for repair and recycling of automotive vehicles. *International Journal of Adhesion and Adhesives*, 50:119–127, 2014.

[45] Stéphane Mallat. *A wavelet tour of signal processing*. Elsevier, 1999.

[46] Shu Minakuchi, Nobuo Takeda, Shin-ichi Takeda, Yosuke Nagao, Alessandro Franceschetti, and Xiaolin Liu. Life cycle monitoring of large-scale cfrp vartm structure by fiber-optic-based distributed sensing. *Composites Part A: Applied Science and Manufacturing*, 42(6):669–676, 2011.

[47] Subrata Mukherjee, Xuhui Huang, Vivek T Rathod, Lalita Udpa, and Yiming Deng. Defects tracking via nde based transfer learning. In *2020 IEEE International Conference on Prognostics and Health Management (ICPHM)*, pages 1–8. IEEE, 2020.

[48] Subrata Mukherjee, Xuhui Huang, Lalita Udpa, and Yiming Deng. Nde based cost-effective detection of obtrusive and coincident defects in pipelines under uncertainties. In *2019 Prognostics and System Health Management Conference (PHM-Paris)*, pages 297–302. IEEE, 2019.

[49] Adnan H Nayfeh. *Wave propagation in layered anisotropic media: With application to composites*. Elsevier, 1995.

[50] Zinoviy Nazarchuk, Valentyn Skalskyi, and Oleh Serhiyenko. Propagation of elastic waves in solids. In *Acoustic Emission*, pages 29–73. Springer, 2017.

[51] Marcos E Orchard and George J Vachtsevanos. A particle-filtering approach for on-line fault diagnosis and failure prognosis. *Transactions of the Institute of Measurement and Control*, 31(3-4):221–246, 2009.

[52] SK Panigrahi and B Pradhan. Three dimensional failure analysis and damage propagation behavior of adhesively bonded single lap joints in laminated frp composites. *Journal of Reinforced plastics and Composites*, 26(2):183–201, 2007.

[53] S Pant, Jeremy Laliberte, Marcias Martinez, and B Rocha. Derivation and experimental validation of lamb wave equations for an n-layered anisotropic composite laminate. *Composite Structures*, 111:566–579, 2014.

[54] Paul Croce Paris and Fazil Erdogan. A critical analysis of crack propagation laws. ASME, 1963.

[55] Tishun Peng, Yongming Liu, Abhinav Saxena, and Kai Goebel. In-situ fatigue life prognosis for composite laminates based on stiffness degradation. *Composite Structures*, 132:155–165, 2015.

[56] H Polli, L Pontes, A Araujo, Joana Barros, and V Fernandes. Degradation behavior and kinetic study of abs polymer. *Journal of thermal analysis and calorimetry*, 95(1):131–134, 2009.

[57] Nicolas Quaegebeur, Philippe Micheau, Patrice Masson, and Hugo Belanger. Structural health monitoring of bonded composite joints using piezoceramics. *Smart Materials, Structures & NDT in Aerospace, number November*, 10, 2011.

[58] Vivek T Rathod, Subrata Mukherjee, and Yiming Deng. Machine learning enabled damage classification in composite laminated beams using mode conversion quantification. In *Nondestructive Characterization and Monitoring of Advanced Materials, Aerospace, Civil Infrastructure, and Transportation XIV*, volume 11380, page 113800B. International Society for Optics and Photonics, 2020.

[59] SI Rokhlin. Lamb wave interaction with lap-shear adhesive joints: Theory and experiment.

The Journal of the Acoustical society of America, 89(6):2758–2765, 1991.

[60] Joseph L Rose. *Ultrasonic guided waves in solid media*. Cambridge university press, 2014.

[61] Joseph Lawrence Rose, KM Rajana, and MKT Hansch. Ultrasonic guided waves for nde of adhesively bonded structures. *The Journal of adhesion*, 50(1):71–82, 1995.

[62] M Sander and HA Richard. Lifetime predictions for real loading situations—concepts and experimental results of fatigue crack growth. *International journal of fatigue*, 25(9):999–1005, 2003.

[63] MJ Santos and P Faia. Propagation of ultrasonic lamb waves in aluminium adhesively bonded lap joints and in single plates. *Research in Nondestructive Evaluation*, 20(3):178–191, 2009.

[64] Emmanuel Siryabe, Mathieu Renier, Anissa Meziane, and Michel Castaings. The transmission of lamb waves across adhesively bonded lap joints to evaluate interfacial adhesive properties. *Physics procedia*, 70:541–544, 2015.

[65] Michael Smith. *ABAQUS/Standard User's Manual, Version 6.9*. Dassault Systems Simulia Corp, United States, 2009.

[66] Stemnic.

[67] Nasrin Sultana, Naveen Chilamkurti, Wei Peng, and Rabei Alhadad. Survey on sdn based network intrusion detection system using machine learning approaches. *Peer-to-Peer Networking and Applications*, 12(2):493–501, 2019.

[68] Suhail Hyder Vattathurvalappil. *Experimental and Numerical Characterization of Bonded Joints Using Reversible Adhesives*. PhD thesis, Michigan State University, 2020.

[69] Suhail Hyder Vattathurvalappil and Mahmoodul Haq. Thermomechanical characterization of nano-fe3o4 reinforced thermoplastic adhesives and single lap-joints. *Composites Part B: Engineering*, 175:107162, 2019.

[70] SUHAIL HYDER VATTATHURVALAPPIL, SYED FAHAD HASSAN, and MAHMOODUL HAQ. Monitoring residual strains in oven-and induction-bonded joints. In *Proceedings of the American Society for Composites—Thirty-fourth Technical Conference*, 2019.

[71] Suhail Hyder Vattathurvalappil, Syed Fahad Hassan, and Mahmoodul Haq. Healing potential of reversible adhesives in bonded joints. *Composites Part B: Engineering*, page 108360, 2020.

[72] Suhail Hyder Vattathurvalappil, Syed Fahad Hassan, and Mahmoodul Haq. Healing potential of reversible adhesives in bonded joints. *Composites Part B: Engineering*, 200:108360, 2020.

[73] Michel Verleysen and Damien François. The curse of dimensionality in data mining and

time series prediction. In *International work-conference on artificial neural networks*, pages 758–770. Springer, 2005.

[74] Elena Verna, Irene Cannavaro, Valentina Brunella, Ermias Gebrekidan Koricho, Giovanni Belingardi, Davide Roncato, Brunetto Martorana, Vito Lambertini, Vasilica Alina Neamtu, and Romeo Ciobanu. Adhesive joining technologies activated by electro-magnetic external trims. *International Journal of Adhesion and Adhesives*, 46:21–25, 2013.

[75] J Vishnuvardhan, CV Krishnamurthy, and Krishnan Balasubramaniam. Genetic algorithm based reconstruction of the elastic moduli of orthotropic plates using an ultrasonic guided wave single-transmitter-multiple-receiver shm array. *Smart materials and structures*, 16(5):1639, 2007.

[76] Thomas Vogt, Michael Lowe, and Peter Cawley. Cure monitoring using ultrasonic guided waves in wires. *The Journal of the Acoustical Society of America*, 114(3):1303–1313, 2003.

[77] Thomas K Vogt, JS Lowe, and Peter Cawley. Measurement of the material properties of viscous liquids using ultrasonic guided waves. *IEEE transactions on ultrasonics, ferroelectrics, and frequency control*, 51(6):737–747, 2004.

[78] Dong Wang, Lin Ye, Youhong Tang, and Ye Lu. Monitoring of delamination onset and growth during mode i and mode ii interlaminar fracture tests using guided waves. *Composites science and technology*, 72(2):145–151, 2012.

[79] Scott R White, Nancy R Sottos, Philippe H Geubelle, Jeffrey S Moore, Michael R Kessler, SR Sriram, Eric N Brown, and S Viswanathan. Autonomic healing of polymer composites. *Nature*, 409(6822):794–797, 2001.

[80] Enrico Zio and Giovanni Peloni. Particle filtering prognostic estimation of the remaining useful life of nonlinear components. *Reliability Engineering & System Safety*, 96(3):403–409, 2011.